

BOSTON UNIVERSITY

GRADUATE SCHOOL OF ARTS AND SCIENCES

Dissertation

UNDERSTANDING THE BRAIN THROUGH ITS SPATIAL STRUCTURE

by

WILL ZACHARY MORRISON

B.S., University of New Hampshire, 2007

M.A, Boston University, 2013

Submitted in partial fulfillment of the
requirements for the degree of
Doctor of Philosophy

2015

© Copyright by

WILL MORRISON

2015

Approved by

First Reader _____

H. Eugene Stanley, Ph.D.

Professor of Physics

Second Reader _____

Rama Bansil, Ph.D.

Professor of Physics

UNDERSTANDING THE BRAIN THROUGH ITS SPATIAL STRUCTURE

(Order No.)

WILL ZACHARY MORRISON

Boston University Graduate School of Arts and Sciences, 2015

Major Professor: Gene Stanley, Professor of Physics

ABSTRACT

The spatial location of cells in neural tissue can be easily extracted from many imaging modalities, but the information contained in spatial relationships between cells is seldom utilized. This is because of a lack of recognition of the importance of spatial relationships to some aspects of brain function, and the reflection in spatial statistics of other types of information. The mathematical tools necessary to describe spatial relationships are also unknown to many neuroscientists, and biologists in general.

We analyze two cases, and show that spatial relationships can be used to understand the role of a particular type of cell, the astrocyte, in Alzheimer's disease, and that the

geometry of axons in the brain's white matter sheds light on the process of establishing connectivity between areas of the brain.

Astrocytes provide nutrients for neuronal metabolism, and regulate the chemical environment of the brain, activities that require manipulation of spatial distributions (of neurotransmitters, for example). We first show, through the use of a correlation function, that inter-astrocyte forces determine the size of independent regulatory domains in the cortex. By examining the spatial distribution of astrocytes in a mouse model of Alzheimer's Disease, we determine that astrocytes are not actively transported to fight the disease, as was previously thought.

The paths axons take through the white matter determine which parts of the brain are connected, and how quickly signals are transmitted. The rules that determine these paths (i.e. shortest distance) are currently unknown. By measurement of axon orientation distributions using three-point correlation functions and the statistics of axon turning and branching, we reveal that axons are restricted to growth in three directions, like a taxicab traversing city blocks, albeit in three-dimensions. We show how geometric restrictions at the small scale are related to large-scale trajectories. Finally we discuss the implications of this finding for experimental and theoretical connectomics.

Table of Contents

1. INTRODUCTION	1
2. REVIEW OF ANATOMICAL AND FUNCTIONAL NEUROSCIENCE	7
2.1 A HISTORICAL INTRODUCTION TO NEUROSCIENCE.....	7
2.2 BASIC ANATOMY OF THE BRAIN.....	10
<i>Cell Types: Form and Function.....</i>	<i>10</i>
<i>Neuronal components.....</i>	<i>11</i>
<i>The Soma.....</i>	<i>13</i>
<i>Processes – The Axon.....</i>	<i>14</i>
<i>Processes – Dendrites.....</i>	<i>17</i>
<i>Glial Cells – Astrocytes.....</i>	<i>18</i>
<i>Glia – Oligodendrocytes.....</i>	<i>19</i>
<i>Glia – Microglia.....</i>	<i>21</i>
<i>Organization of the Brain.....</i>	<i>21</i>
<i>Coordinate Systems.....</i>	<i>21</i>
<i>Divisions of the Central Nervous System – Fore, Mid and Hindbrain.....</i>	<i>23</i>
<i>Structure of the Cerebrum.....</i>	<i>24</i>
3. OVERVIEW OF QUANTITATIVE TOOLS.....	29
3.1 QUANTIFICATION OF COLLECTIONS POINTS	29
3.2 REPRESENTATION OF CELLS AS POINT-LIKE OBJECTS.....	30
3.2 STOCHASTIC PROCESSES AND SETS OF POINTS	31
<i>The Poisson Point Process.....</i>	<i>31</i>

<i>Non-uniform Point Processes</i>	32
3.3 DESCRIPTIONS OF POINT PROCESSES.....	34
<i>N-Point Correlation Functions</i>	34
<i>Tessellation Based Descriptions</i>	37
3.4 COMPUTATION OF DESCRIPTORS	39
<i>Two-Point Correlation Function: Radial and Vector Pair Correlation, and Estimators</i>	39
<i>Two-Point Correlation Function: Computation with Pair Counting Method</i>	44
<i>Three-Point Correlation Function: Extended Objects and Subsets</i>	50
<i>The Three-Point Function and Path Probability</i>	54
<i>Voronoi Diagrams</i>	61
4. THE STRUCTURAL RESPONSE OF ASTROCYTES IN ALZHEIMER'S DISEASE.....	64
4.1 SUMMARY OF FINDINGS AND IMPACT	66
4.2 EXPERIMENTAL DESIGN.....	67
<i>Three-Dimensional Location Acquisition</i>	67
<i>In-Vivo Imaging</i>	68
<i>Pan-Astrocytic Labeling</i>	69
<i>Overview of Experimental System</i>	69
4.3 EXPERIMENTAL METHODS	70
<i>Animals and Surgery</i>	71
<i>Labeling Procedures</i>	72
<i>In-vivo Imaging</i>	72
<i>Image Processing: Advantages and Challenges of Data Extraction from Fluorescence</i>	
<i>Microscopy</i>	73

<i>Image Processing: Plaque Extraction</i>	76
<i>Image Processing: Blood Vessel Extraction</i>	79
<i>Image Processing: Astrocyte Extraction</i>	81
<i>Data Summary</i>	84
4.4 ASTROCYTE PAIR CORRELATION ANALYSIS.....	85
4.5 ASTROCYTE VORONOI TESSELLATION ANALYSIS.....	96
4.6 SIMULATION OF ASTROCYTE-PLAQUE INTERACTIONS	104
4.7 BIOLOGICAL INTERPRETATION OF ALZHEIMER’S ASSOCIATED MODIFICATIONS IN ASTROCYTE STRUCTURE AND DISCUSSION	110
5 STRUCTURAL MOTIFS OF LONG-RANGE AXONS.....	116
5.1 EXPERIMENTAL DESIGN.....	119
5.2 EXPERIMENTAL METHODS – TNIMALS, TISSUE PREPARATION AND IMAGING.....	121
<i>Subjects:</i>	121
<i>Surgical Procedure and Tracer Injections</i>	122
<i>Perfusion Procedure and Tissue Harvest</i>	122
<i>Tissue Processing Procedures</i>	122
<i>Visualization of Tract Tracers</i>	122
<i>Immunohistochemistry for SMI-312 and SMI-32</i>	123
<i>Microscopy</i>	123
<i>dMRI Imaging</i>	123
5.3 EXPERIMENTAL METHODS – TMAGE ANALYSIS.....	124
<i>Correlative Orientation Analysis</i>	124
<i>Turn and Branch Identification and Measurement</i>	129

5.4 RESULTS OF IMAGE ANALYSIS	132
<i>Patterns of Axon Orientation</i>	132
<i>Branching and Turning Rates, Anisotropy, and Alignment with Grid</i>	146
5.7 IMPLICATIONS FOR GRID STRUCTURE AND LONG-RANGE TRAJECTORIES.....	155
<i>Mathematical Modeling of Connectivity</i>	155
<i>Biological Implications</i>	159
6. DISCUSSION AND FUTURE PROSPECTS	161
BIBLIOGRAPHY	166
CURRICULUM VITAE	171

1. Introduction

The obvious question to ask in response to the title of this dissertation is why we bother measuring spatial relationships between cells in the brain? After all, anyone with a basic knowledge of neuroscience knows that neurons communicate with each other through long, thin axons and dendrites – the cellular equivalent of wires. These cellular wires evolved to enable a pair of neurons to communicate regardless of the distance between them, unshackling cellular signaling from the spatially dependent chains of diffusion. Should we not then focus on the connectivity and diversity of components in the brain, which surely are the features that define its functions and dysfunctions?

It is probably true that, ideally, the function of the brain would be independent of how its components are embedded in space. However, the brain *is* embedded in space, and ignoring the spatial relationships between its components risks overlooking a source of important information. There is an old trope that you can learn a lot about a person if you understand the challenges they have overcome. By examining the brain's attempts to free itself from structural constraints, we can learn about the processes that are important to brain function.

Two examples of this type of analysis are performed here. The first analysis concerns a set of cells known as astrocytes. These cells are caretakers of the neurons, overseeing needs such as the provision of nutrients, the regulation of chemical signals, and the maintenance and construction of synapses. These tasks all involve the manipulation of the spatial distribution of some necessary ingredient for neural function, so it is expected that the spatial distribution of astrocytes is important. The distribution of astrocytes may be regulated, for example, to prevent density fluctuations

of too high a magnitude. Low densities of astrocytes may be overwhelmed by their regulatory responsibilities. High densities, conversely, would represent a misallocation of resources such as cortical space and energy, and might lead to astrocytes interfering with one another.

The spatial distribution of astrocytes is hypothesized to be altered by injury to the brain. Astrocytes and some other cells are thought to migrate to the site of injury, such as that caused by a stroke or puncture wound, both for the purpose of repair, and also to seal off the injured part of the brain, preventing the spread of toxic materials. We will examine here a particular case: the response of astrocytes to Alzheimer's disease. One harmful agent in Alzheimer's is a toxic protein known as amyloid-beta, which forms locally toxic deposits known as plaques. It has been previously recognized that "activated" astrocytes are found around the plaque. These differ from normal astrocytes through modifications to the proteins that make up their cytoskeleton. This led to the idea that astrocytes respond to plaques the same way they do to gross injury, by migrating to plaques. It is also hypothesized that astrocytes fight Alzheimer's by absorbing amyloid-beta, reducing plaque size, and sealing off plaques to prevent injury to surrounding neurons.

Disease can be studied in a controlled manner through the use of animal models. We study the effect of amyloid-beta plaques on the distribution of astrocytes through the use of a transgenic mouse, whose genome has been modified to produce amyloid-beta plaques. Astrocytes, amyloid-beta plaques and other cortical residents can be imaged in these mice while they are still living by installing transparent windows in their skulls, and using three-dimensional two-photon fluorescence microscopy to peer down below the surface of the brain.

Tracking the locations of individual cells as amyloid-beta builds up in the brain is possible, but very difficult experimentally. Imaging must be done regularly enough that cells change position by small amounts, so that they are not confused with one another. Every imaging experiment requires anesthetizing the animal, which carries significant risks. Losing a mouse in this manner is costly in terms of both time and money, and may even risk biasing the experiment if mortality is related to the course of pathology. Mice can re-grow material under a cranial window, which requires surgery to correct. This surgery is risky, and causes inflammation, so cells cannot be tracked from before surgery. Other experimental difficulties can arise from equipment malfunction; if a microscope goes down for a significant amount of time, the experiment must be ended.

By inferring the possible migratory action of astrocytes from their spatial distribution, we avoid these experimental difficulties. This requires only a single imaging session from each mouse. We compare the spatial distribution of astrocytes in transgenic mice to healthy wild-type mice, and attribute differences to the action of amyloid-beta plaques. We show that contrary to popular belief, astrocytes do not migrate to plaques. Instead, we detect a small distance dependent shift *away* from plaques. The closest astrocytes move by a few microns, about the diameter of the cell body. During the course of the study, we also detect evidence of a heretofore unrecognized interaction between astrocytes.

The second study concerns axons, the cellular wires linking neurons together. As we have noted, an axonal link allows one neuron to communicate with another, rapidly, with good fidelity and without disturbing their neighbors, regardless of their spatial location. However, to establish this link, an axon must first navigate the space between

neurons. Understanding the principles of this navigation will ultimately provide insight into the signals and rules used for navigation, how it is determined who will connect with whom, and how disorders resulting from aberrant connectivity arise from the construction of axonal pathways.

The trajectories of axons in primates have been studied with two experimental techniques, molecular tracers, and degeneration studies. Degeneration studies are the older of the two. The first step is to remove a small chunk of the cortex. The axons of these cells will soon degrade, and which makes them visible in the dissected brain. Newer experiments use molecular tracers, a dye which is transported along an axon, which can again be identified in dissections.

Experimentalists interested in the connections made by neurons in an area would use either degeneration or tracer dyes to mark the axons of a small group of neurons. They would then take several thin slices of brain, separated by some distance, and identify the locations of the marked axons in these slices. Typically, they would see groups of axons in each two-dimensional slice. The three-dimensional trajectories were estimated by essentially connecting the dots, filling in the distance between the slices.

When connecting the dots, researchers made some reasonable seeming assumptions, namely of smooth axon trajectories, minimizing bending. Mathematically, an interpolation minimizing bending is equivalent to cubic spline interpolation. Cubic splines are exact for an elastic rod forced to intersect a set of points, a natural interpolation from human experience.

Results from imaging of the diffusion propagator using MRI have recently cast doubt on the validity of the smoothness assumption. These results show that the

diffusion propagator of water, which is restricted to the insides of axons in white matter, has between one and three approximately orthogonal peaks in any small volume of the brain. The peaks of adjacent voxels line up, forming sheets of parallel tubes. These sheets are also spatially ordered: though they are warped, they never intersect one another. This interesting structure was dubbed the “grid” by its discoverer, Van Wedeen. The grid is incongruent with the traditional notion of smooth paths between points – how can axons form smooth paths, when they are constrained to choosing from such a restricted set of orientations?

The smallest voxels used in dMRI are about $(0.5\text{mm})^3$, and average over several thousand axons. Perhaps the smoothness assumption is not so inaccurate if this is only a collective behavior, and large deviations from the average in opposite directions cancel one another out.

We carried out experiments to quantify the geometric properties of axons in large images of axons taken with high-resolution microscopy. Although we are restricted to two dimensions, which, if the observations using MRI hold, will limit us to observation of two peaks in the orientation of axons, we are able to unambiguously resolve single axonal fibers. This enables us to determine the scale of this regulation of axon orientation. We discover that the majority of axons are restricted to a narrow range of orientations around two peaks. Furthermore, we find that axons conform to the grid at lengths scales of tens of microns. We find evidence that instead of smoothly curved trajectories, axons branch, or make sharp turns between allowed orientations.

This has implications for the organizational principles of the brain’s white matter, the mechanisms axons use to navigate, and the technologies used to measure connectivity. The statistics of turns and branches must produce the bundles of axons

observed in older studies. This collective behavior is very different from the smooth paths imagined in the past. Although diffusion MRI produced the initial observations that led to this discovery, these crucial turns and branches are below its resolution. This should inspire researchers to develop techniques to estimate the interaction between orientations in a given voxel.

Before engaging in these analyses, we will first give a brief overview of the field of neuroscience, focusing in particular on the biology of systems involved in our analyses. We will then discuss methods for describing the spatial distribution of points, including both the general theory behind point processes and the mechanics of calculating various descriptors. We will then proceed to analysis, filling in specific experimental methodological details when necessary. We will conclude with an overview of the impact of this work on the understanding of the brain and what can be learned from point processes, and future directions this work may take.

2. Review of Anatomical and Functional Neuroscience

This section contains a historical overview of neuroscience from prehistory to its modern underpinnings. A review of the anatomical description of the brain is then given, with special focus given to topics important to the investigations in this thesis. Techniques of experimental neuroscience important to anatomical observation are reviewed.

2.1 A Historical Introduction to Neuroscience

Humans have probably been aware of the brain's importance for mental function since the dawn of prehistory – one only has to experience the headache and mental effects of a bump in the head to realize that the skull's contents are critical for thinking. Evidence for this exists in the archeological record in the form of fatally damaged skulls dating back millions of years to our early hominid ancestors, with the damage presumably caused by other ill-intentioned hominids.

In the classical era, many Greek scholars understood that the brain was involved in mental function. Hippocrates, the father of modern medicine, was a chief proponent of this view, stating that the brain was “the primary seat of sense and of the spirits,” and responsible for understanding reality [Hippocrates]. This view was not universally accepted (Aristotle was a notable detractor), but became the mainstream view of physicians during the Roman Empire. The Roman physician Galen was one of the first to subdivide the brain into distinct areas. He noticed structural differences between parts of the brain now known as the *cerebrum* and the *cerebellum*, and made the impressively accurate suggestion that sensation were perceived and memories stored in the cerebrum, while the cerebellum would be responsible for motor control. Galen was

also the instigator of a theory of brain function that persisted until the eighteenth century. This was that the brain essentially functioned hydraulically, by pumping fluids known as the “humors” from the brain through the nerves, which were thought to be pipes similar to the blood vessels. The ventricles are a system of large cavities in the brain that contain cerebrospinal fluid, and due to this hydraulic view, were thought to be the key component of the brain.

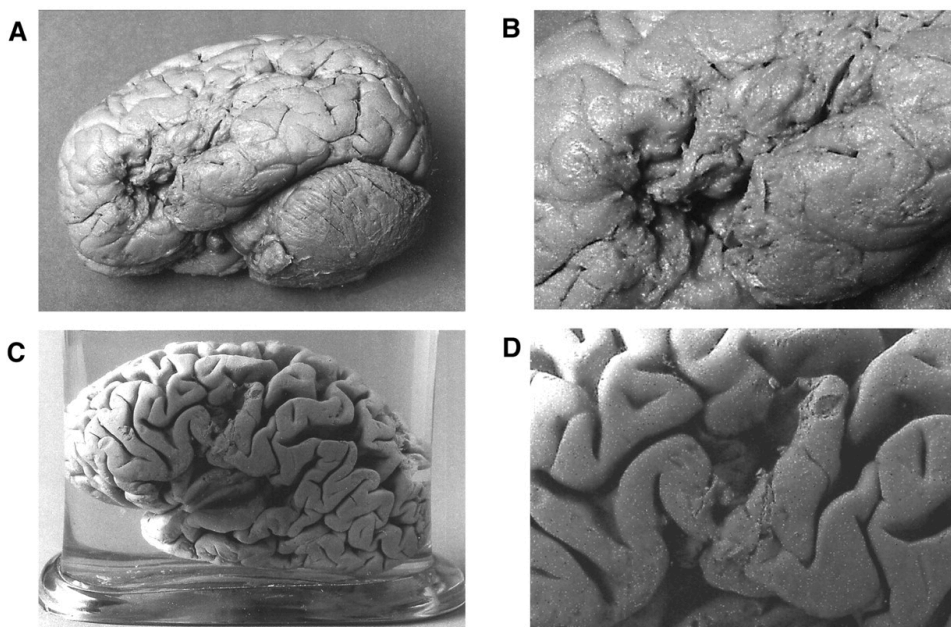


Figure 2.1. Photographs of the preserved brains of Broca’s aphasic patient. Panels A and C show the damage in the context of the entire brain, while B and D are close up demonstrating the extent of the damage. Taken from Dronkers, et al 2007.

Neuroscience rushed into its modern era in the late eighteenth and nineteenth centuries. Luigi Galvani’s famous experiments demonstrating movement in the leg of a frog showing that electricity, not fluid humors, was being conducted in nerves. Concurrently, a new experimental technique was elevating the importance of the solid

matter of the brain in mental function, at the expense of the ventricles. This was the observation of behavioral change, or motor and sensory deficits after the destruction of a small chunk of neural tissue, either through surgical ablation or through natural causes. The most famous of these experiments was the physician Paul Broca's observations of two patients suffering from expressive aphasia, a disorder in which one can understand the speech of others, but has great difficulty in speaking themselves (one of Broca's patients could only utter a single syllable, "tan," for example). Broca observed damage to a small part of the left frontal lobe in both patients, and correctly deduced that this region was responsible for the generation of speech. This solidified the notion of functional localization, in which, at a given time, each chunk of neural tissue has a defined processing task.

The last vital step that took neuroscience into its modern era was the introduction of microscopy capable of resolving cells at the modern level. Two giants of modern neuroscience, Camillo Golgi and Santiago Ramon y Cajal, pioneered the combination of high resolution microscopy with chemical contrast agents (see Figure 2.1) that targeted specific cells and subcellular components, creating the field of neurohistology and discovering that the brain was composed of neurons and other discrete cells.

Neuroscience today continues along the same basic lines of research: investigating the patterns of neuronal excitation through their electrical activity (and other, newer techniques), observing neural form and structural arrangement, and mapping the functional layout of the brain. The ever-expanding body of experimental knowledge has given neuroscience a window into the basic workings of the brain: how it develops, processes information, and what can go wrong.

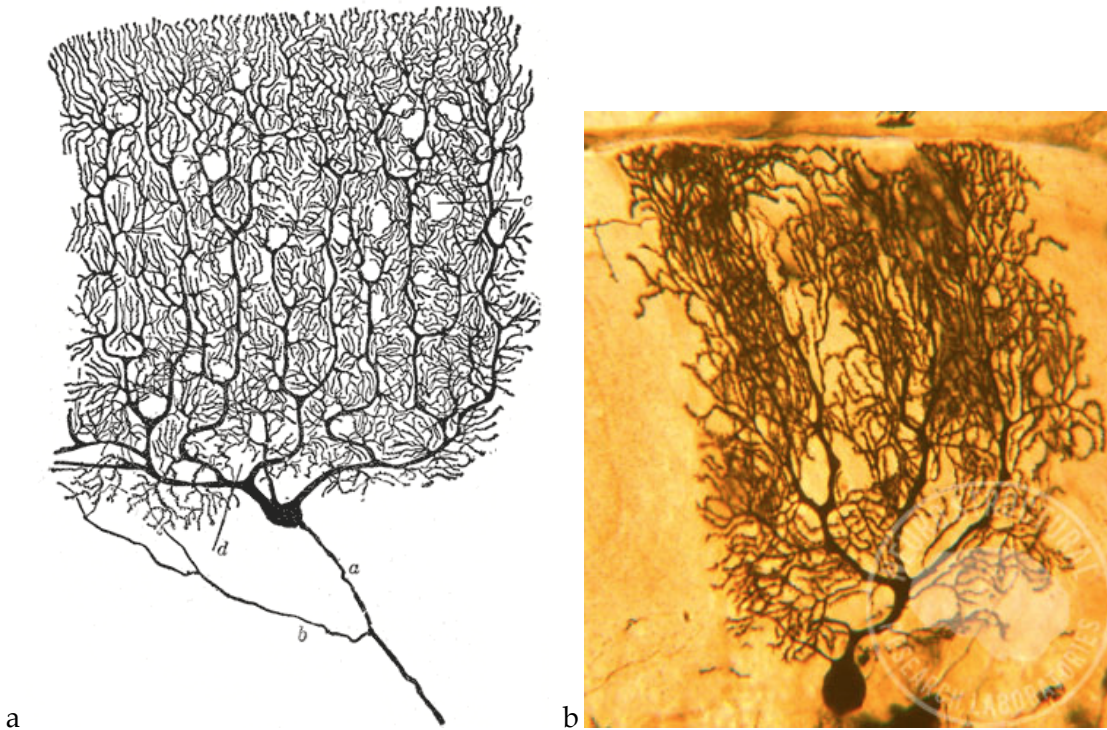


Figure 2.2. Dendritic Arbors. A) A drawing of a Golgi stained cerebellar Purkinje cell by Ramon y Cajal. From Gray's Anatomy. B) A photomicrograph of a cerebellar Purkinje cell, stained by the Golgi method. From the Neuron Gallery Collection [Mervis].

2. 2 Basic Anatomy of the Brain

Cell Types: Form and Function

The two primary classes of cells in the brain are neurons and glia. Neurons are a set of excitable cells, whose connections form the electrochemical network that processes

information in the brain. Glia, which means “glue” in Latin, encompass a variety of cell types which perform support functions for the neurons, although some studies suggest that a subset of glial cells can participate in signaling and electrically excite neurons [e.g. Nedergaard].

Neuronal components

Neurons are an impressive cell based on the complexity of their external form alone. Thin tendrils called processes extend from a compact body known as the soma. These processes, on the order of a micron in diameter, can form dense arbors a few millimeters in width. Single processes can extend extreme distances. The longest neuronal processes in the human CNS are several centimeters long, making neurons the largest cells in the body (peripheral nervous system neurons can have processes over a meter long). Processes are subdivided into two classes: dendrites, which receive signals and transport them to the soma where they are integrated, and axons, which transmit signals from the soma to other neurons. Axons transmit signals to dendrites at synapses, close contacts with a gap, or synaptic cleft, across which small neurotransmitter molecules are released from the axon and activate receptors in the dendrite.

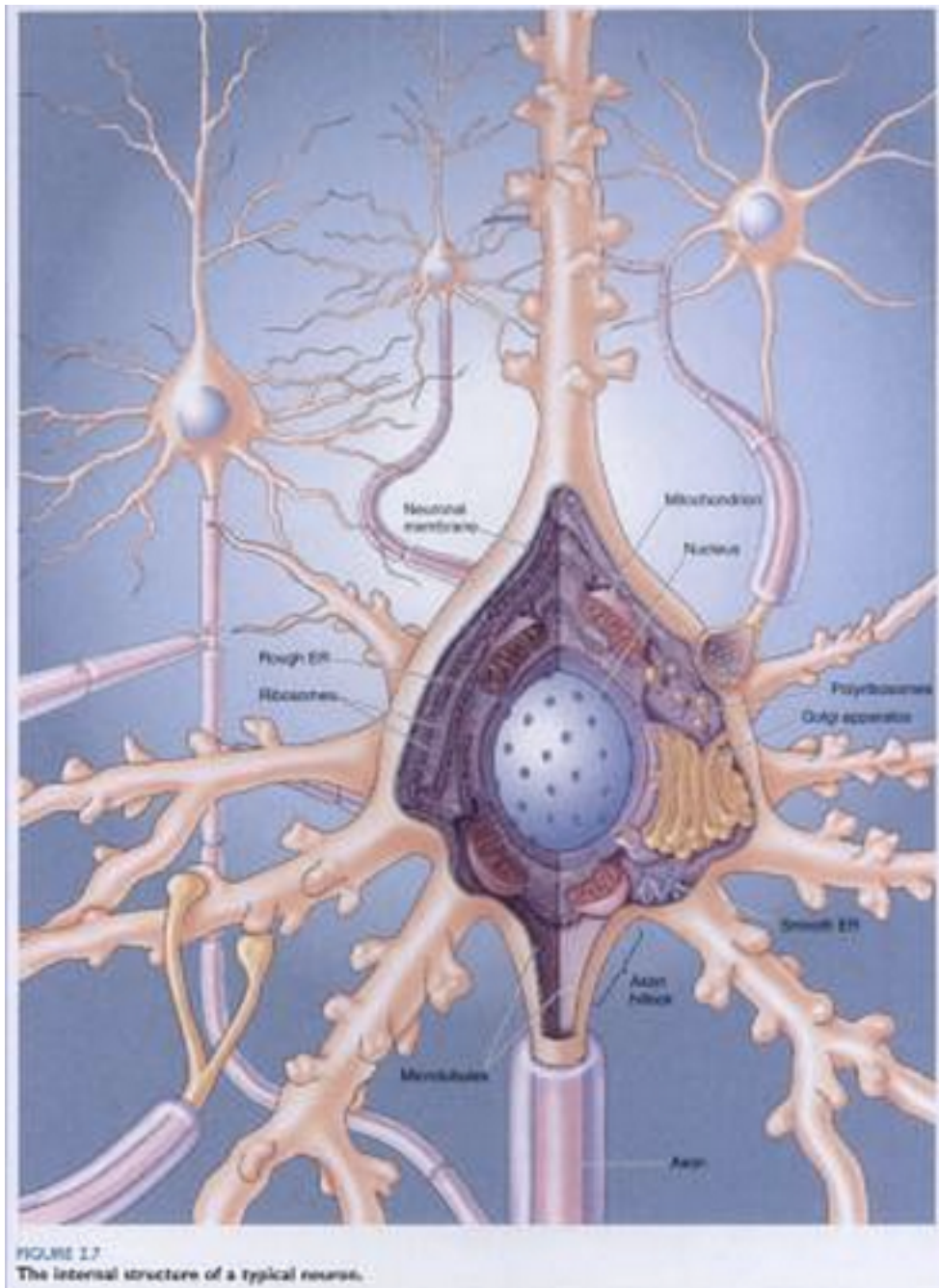


Figure 2.3: The internal structure of a typical neuron, illustrating the internal structure of the soma and dendritic and axonal processes extending to contact other neurons.

Reproduced from [Bear, et. al., Figure 2.7]

The Soma

The soma contains the cell nucleus, and other cellular machinery typical to maintaining a cell. The distinguishing feature of a neuron, of course, is its ability to receive and transmit electrochemical excitations. The neuron achieves this by maintaining a potential difference of -65 mV with respect to the extracellular medium. Voltage sensitive ion pumps and channels in the membrane of the soma maintain this voltage difference. The intra- and extra-cellular fluids in the brain contain both negatively and positively charged ions, primarily potassium, sodium and calcium. In a neurons resting state, it achieves this -65 mV polarization by employing potassium-selective channels. Osmotic forces drive potassium from the intra-cellular fluid, with a high potassium salt concentration, leaving their anions behind, until the osmotic and electrical forces are in equilibrium. However, the soma membrane also contains sodium-selective channels.

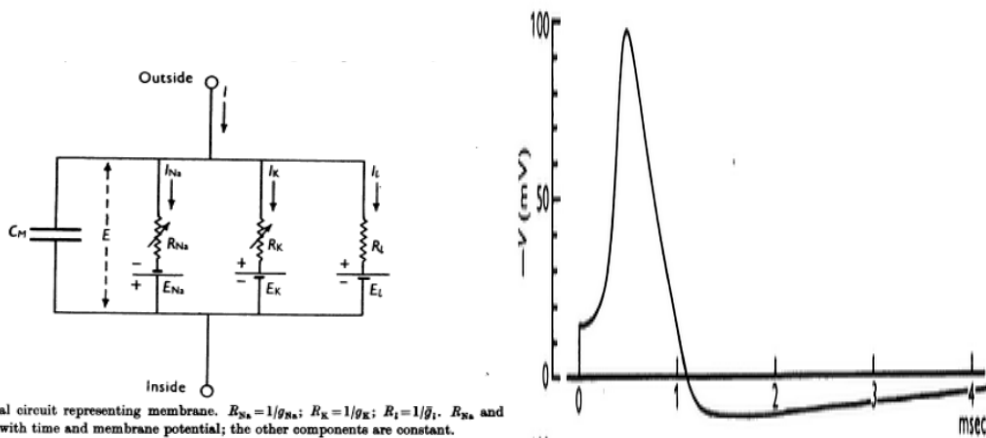


Figure 2.4. Action Potentials. A) The simplified membrane circuit proposed by the Hodgkin-Huxley model, which incorporated the effects of sodium (Na^+) and potassium (K^+) channels, leakage current (L) and membrane capacitance (C_M) in the generation of

membrane potential V_m . B) Membrane voltage as a function of time after the initiation of the action-potential-generating process, with labeled epochs. An initial depolarization spike is followed by a hyperpolarized refractory period, during which the neuron cannot fire. Note that the y-axis voltages refer to experiments on the giant squid axon, which Hodgkin and Huxley used because its large size facilitated experimental measurements, while the text refers to typical CNS neurons. Figures reproduced from [Hodgkin and Huxley].

The interior of the neuron contains a low concentration of sodium compared to the extra cellular fluid. Under normal polarized conditions, these sodium channels are impermeable. However, electrical input from other neurons can depolarize the soma. When these inputs depolarize the membrane potential to approximately -40mV , the sodium channels become conductive, and the electrochemical gradient rapidly drives in Na^+ , depolarizing the cell. This process actually overshoots electrical neutrality and produces a positive polarization of $+40\text{mV}$. The depolarization propagates down a special neuronal process called the axon, and is known as an “action potential” for its effect on downstream neurons. Sodium channels close after approximately 1 millisecond, initiating the re-polarization process. [Hodgkin and Huxley]

Processes – The Axon

Axons conduct the electrical action potential away from the soma. Axons differ in their myelination state, diameter, length, and degree of arborization. Myelin is a fatty membrane produced by a glial cell, the oligodendrocyte, that serves to insulate the axon from the ionic extracellular fluid. Conduction in an unmyelinated axon proceeds as a depolarization wave through the same voltage gated ion channel mechanism that generates the action potential in the soma: the leading edge of the depolarization wave

triggers an influx of sodium through voltage gated Na^+ channels, which close after a millisecond, allowing a K^+ efflux to repolarize the axon at the trailing edge of the wave.

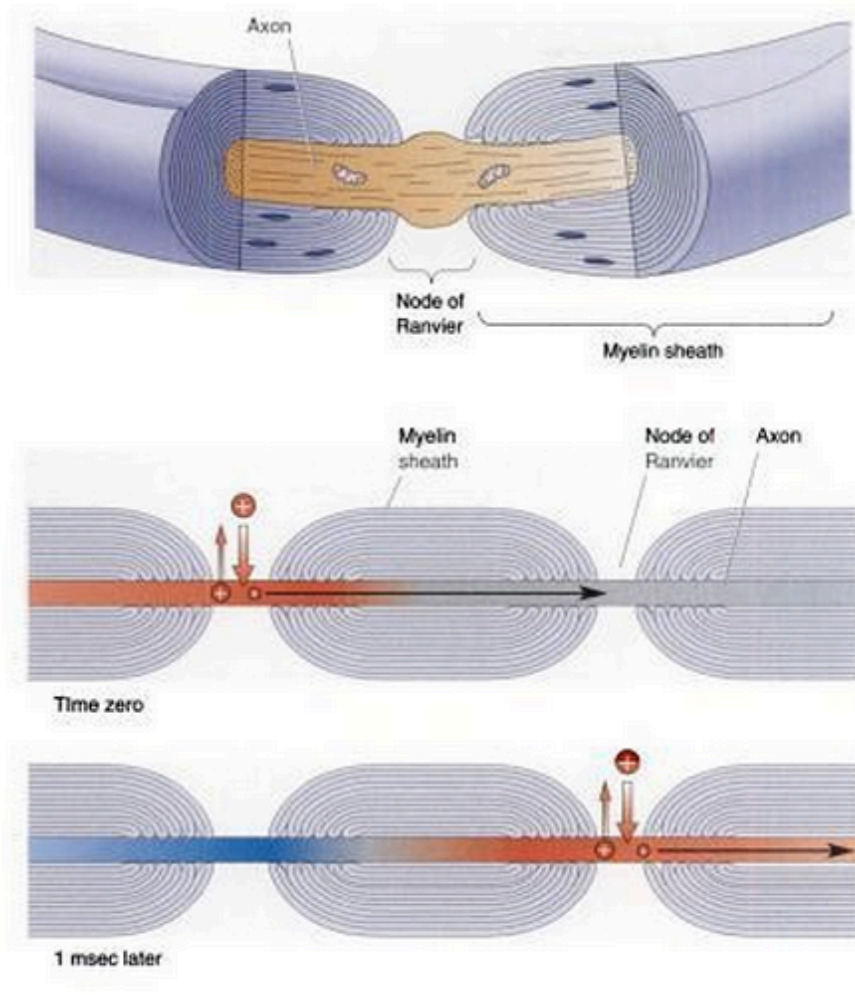


Figure 2.5. Action Potential Conduction. Saltatory action potentials jump from Node of Ranvier to Node of Ranvier. The myelin sheath produced by the oligodendrocyte prevents the electrical potential from leaking from the axon to the extracellular fluid.

Myelin allows a different type of action potential transmission, known as saltatory conduction. These axons have long sections of myelin, which increases resistance and decreases capacitance, interspersed with unmyelinated sections known as the Nodes of Ranvier. Depolarization jumps along the axon from node to node, greatly increasing speed and decreasing energy consumption.

Axon diameter is the other factor besides myelination that determines conduction velocity. A wide range of diameters and conduction velocities can be found in the CNS. In monkeys, axons range from small, unmyelinated axons approximately 0.1 microns in diameter, that conduct signals at about 0.3 m/s, to myelinated axons 20 microns in diameter that conduct at 120 m/s. Axons thus vary by up to a factor of 40,000 in volume and 400 in velocity [Swadlow and Waxman].

Axonal length and arborization are of great interest to this dissertation. Variations in these parameters control how signals are distributed between regions of the brain. Axonal length depends on the type of circuitry a neuron belongs to. Short axons are found in neurons that participate in local information processing, for example the circuits in the visual cortex that transform the representation of visual information from a spatial basis to a frequency (or more precisely, Gabor wavelet) basis. [Lee] These neurons may have excitatory or inhibitory effects on the neurons they synapse with. Longer axons transmit the results from this local processing through the white matter, which in humans occupies about forty percent of the volume of the cortex [Zhang and Sejnowski], and gets its name from the opaque fatty myelin sheaths.

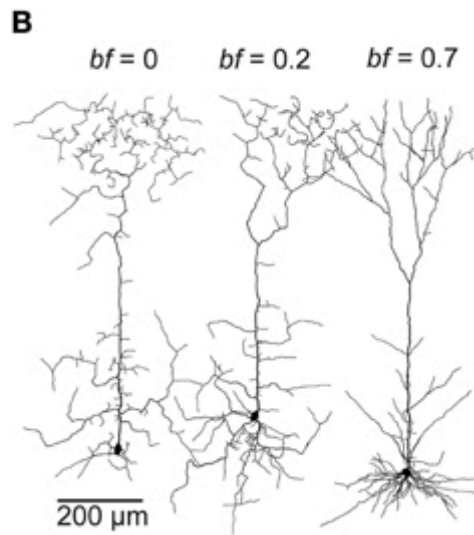


Figure 2.6 Axonal Arbors Axonal arbors (branched structure above soma) of spiny cells (left) and basket cells (right) show differing degrees of branching (measured by depth of bifurcations for example) and directional anisotropy. Adapted from Budd and Kisvarday.

Arborization refers to the tree like branching of the axon. The arborization patterns of short-range axons are well understood. They can range from simple, compact arbors with only a few branches near their terminus, or complex, bushy arbors with several levels of branching. Due to the difficulty of following long-range axons over several centimeters through the brain, their branching structure is much less understood. Prevailing opinion is that branches in the white matter are extremely rare, however our research indicates that they are much more common than previously thought, and may form the basis of inter-area connectivity.

Processes – Dendrites

As opposed to axons, which transmit the action potential, dendrites receive input from other neurons. Action potentials are not received directly, though electrical coupling

between neurons has been observed [e.g. Gibson et. Al.], it is relatively rare in comparison to chemical synapses. The average dendritic arbor in the human brain makes about 7,000 synapses [Pakkenberg].

The Greek root of “dendrite” is “dendro,” meaning tree, and it is so named for its branched spatial structure. Dendritic structure varies between different classes of neurons, but in general they are more densely branched than axons. The arbor of a common neocortical neurons, the pyramidal cell, has a diameter on the order of a few hundred microns in the plane normal to the direction of the axon. Complicated branching patterns are demonstrated in Figures 2.2, in a Purkinje cell, and in spiny and basket cells in Figure 2.6, where they can be compared to the more diffuse axonal arbors.

Glial Cells – Astrocytes

Glia were originally thought to serve simply as structural support for the neurons (their name is literally Latin for “glue”), and the neuroscience community has only recently come to appreciate their importance in brain function. Astrocytes in particular have a variety of important roles in the normal functioning of the brain. Their name is derived from the star-like shape of their cytoskeleton. They are slightly smaller than the typical neuron in the cortex, about five microns in diameter.

Astrocytes regulate the chemical environment of the brain, by uptaking or releasing extracellular neurotransmitters and molecules like potassium, which affects the production of action potentials. They also participate directly in synaptic communication, forming “tripartite” synapses with neurons, removing neurotransmitters from the synaptic cleft and preventing their release into extra-synaptic space (an action analogous to the activity of “reuptake inhibitor” class antidepressant drugs) [Perea et al.]. Astrocytes are also involved in the formation of new

synapses [Allen and Barres]. The formation and regulation of synapses gives the brain the ability to learn.

Astrocytes participate in the synaptic interface between neurons; they also form part of the interface between neurons and the vascular system that supplies the brain with nutrients. Similarly to neurons, astrocytes have long processes extending from their cell bodies. Many of these contact synapses as discussed above, but others contact the epithelial cells that wrap around blood vessels, forming the blood brain barrier. Astrocytes control the vascular response to neuronal activity, up-regulating it when they sense increased metabolism [Takano, et. al.].

Astrocytes also play a role in injury response in the brain, forming a glial scar through a process known as astrogliosis, although the benefits of astrogliosis have been questioned [Fawcett and Asher]. This response is well known in cases of gross injury, such as that caused by stroke or puncture wounds. Astrocytes are also thought to be involved to acute localized injuries, such as the toxic zone around the amyloid-beta plaques of Alzheimer's Disease. Elucidation of the nature of their response to amyloid-beta plaques through observation of their spatial structure will be discussed at length in this thesis.

Glia – Oligodendrocytes

Unlike the multi-functional astrocytes, the oligodendrocytes are specialists. They create the fatty myelin sheath that wraps many axons in the CNS, insulating them from the extracellular environment. The cell body of the oligodendrocyte is small, about two to four microns in diameter. A single oligodendrocyte may provide sections of myelin for several axons, but most axons require many sections of myelin over their length. The

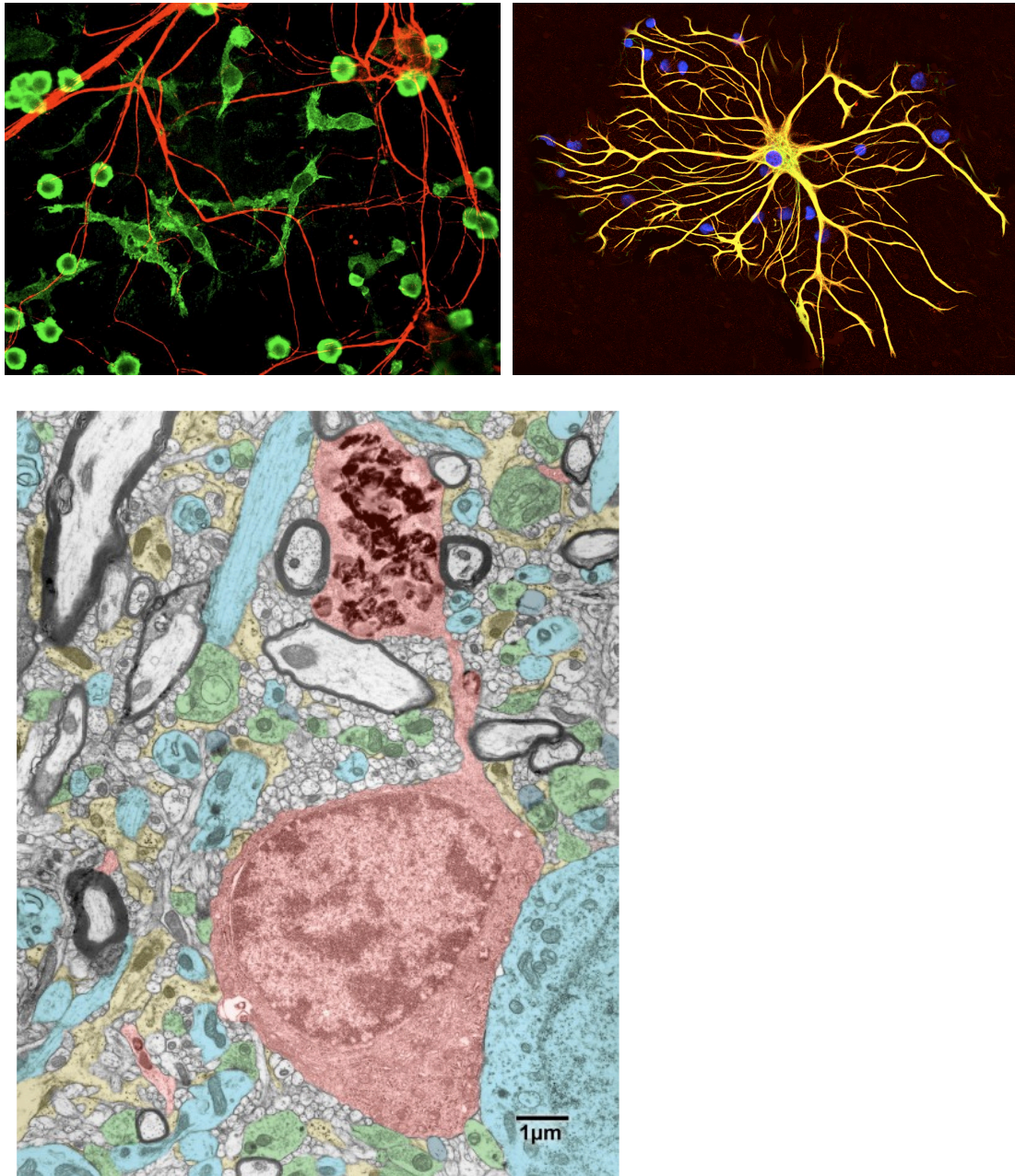


Figure 2.7. Types of glial cells. (a) Microglia stained for coronin 1a (green), among neuronal processes stained for alpha-internexin (red). Small round microglia are inactive, large amoebic microglia are “activated,” in their phage state [Shaw a]. (b) A cultured astrocyte stained with GFAP (yellow), with blue staining the nuclei of the

astrocyte and surrounding cells [Shaw b]. (c) False colored electron micrograph of an oligodendrocyte in layer 4 of the cortex. Oligodendrocytes- red; neuronal cell bodies and dendrites- blue; dendritic spines- grey; axon terminals- green; astrocytes- yellow.

[Reproduced from Peters]

Glia – Microglia

The final common type of glial cell in the CNS is the macrophage microglia. These are small cells with bodies about two to four microns in diameter. They extend thin processes through the cortex to detect potentially harmful elements, such as dead or dying neurons and glia, cellular waste or infectious agents. They remove these through the process of phagocytosis, in which the microglia envelops these elements and degrades them.

Organization of the Brain

We organize the brain through hierarchical subdivisions; similarly to how a person can be a member of a family, town, county, state, country, and continent, a neuron may be a member of a minicolumn, layer, area, hemisphere, and structure or system. Such designations may reflect structural differences between regions of the brain, or functionally defined regions.

Coordinate Systems

In order to discuss how two parts of the brain are related to one another spatially, it is important to define a reference coordinate system. The most commonly used system is that used for the rest of the body, the rostral-caudal, dorsal-ventral, medial-lateral set of axes. This can cause some confusion in bipedal primates, since the brain is tilted from its normal orientation (a person on hands and knees with their neck in a neutral position

will be looking at the ground, this is because their brain is rotated forward 90° compared to that of, say, a mouse). We will use the mouse as the typical quadruped, and the human as a typical biped, to describe these axes.

The rostral-caudal axis is directed from the nose to the tail of the rat. In a human this axis is curved from the nose to the base of the neck. The dorsal-ventral axis translates to English as the back-to-belly axis. In the human brain this axis remains perpendicular to the rostral-caudal axis, starting pointing from the top of the head to the chin in the foremost portion of the brain, and ending pointing from the back to the chest at the base of the neck. Lastly we have the medial-lateral axis, starting at the midline of the body and extending out to the extremities. This has some advantages over a simple left-right axis in its reflection of the bilateral symmetry of the body, for example the elbow is always medial to the hand, regardless of which side of the body you are on. The same relationship between brain structures is observed.

Lastly, the planes of the brain have also been named. This is convenient for neuroanatomy, which until very recently was limited to looking at thin two-dimensional slices of tissue or surfaces. Since sections are not curved, the names of the planes cannot be described in terms of the axes. The planes are instead are oriented with respect to the brains normal position in the animal's body. The sagittal plane is parallel to the midline, the horizontal plane is parallel to the ground, and the coronal plane is perpendicular to both of these.

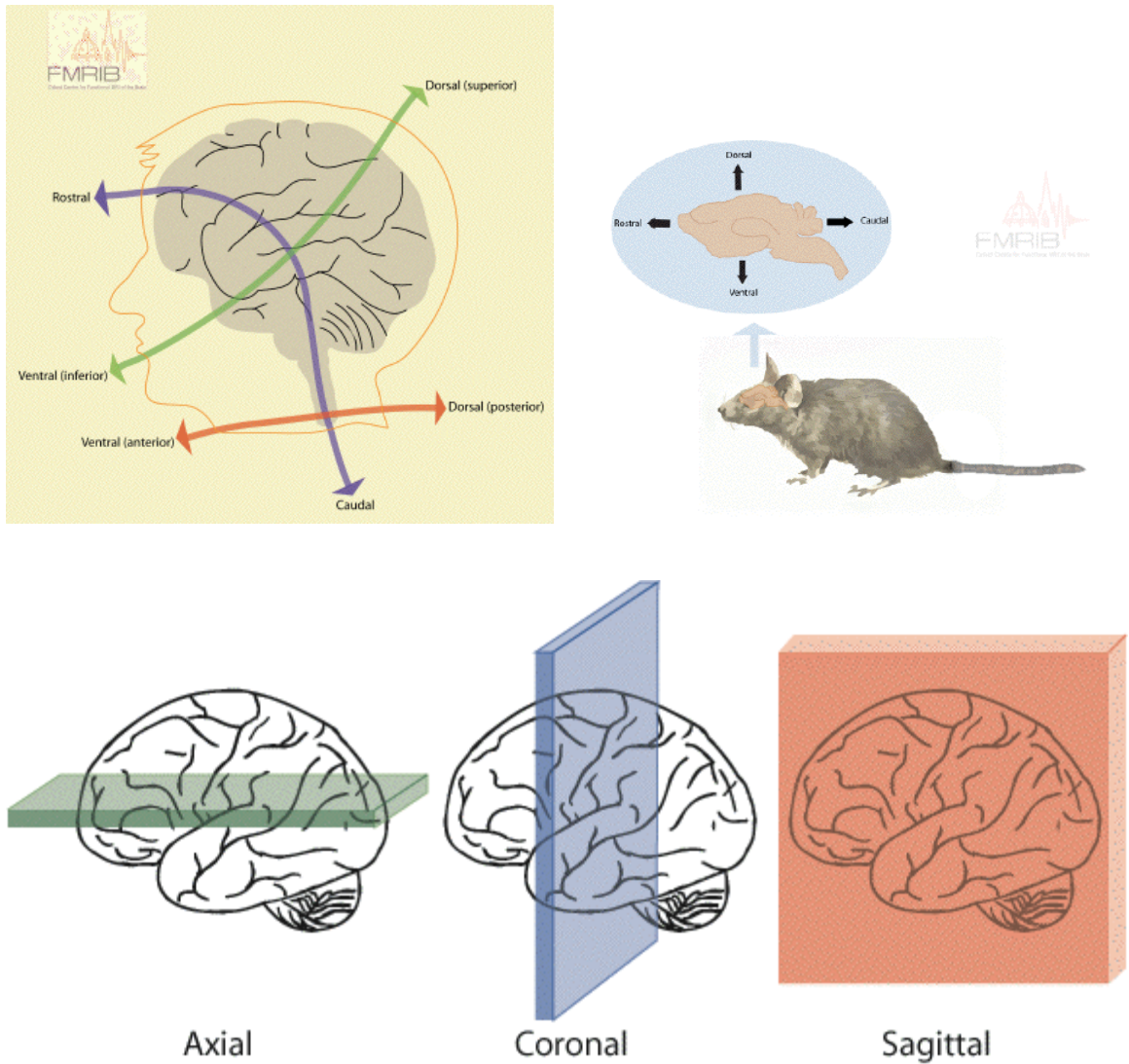


Figure 2.8 Coordinate systems in the brain.

Divisions of the Central Nervous System – Fore, Mid and Hindbrain

The central nervous system can be divided into three structures, which develop from three separate vesicles in the neural tube. These three structures are known as the forebrain, midbrain, and hindbrain, which roughly describe both their relative positions, and the level of the processing tasks they are responsible for.

The forebrain contains the structures responsible for perception, awareness, cognition and voluntary action. It is the largest structure in the mammalian brain, and contains the cerebrum, hypothalamus, thalamus, olfactory bulb, and optic stalks.

The midbrain is a smaller, less structurally differentiated structure. The midbrain contains the superior and inferior colliculus, which receive sensory information from the eyes and ears, as well as axons from the forebrain. It serves as a conduit for information between the forebrain and the rest of the body. The midbrain projects axons to widespread areas of the CNS, and is involved in basic elements of cognition such as mood, pleasure and pain.

Like the midbrain, the hindbrain also serves as a conduit, but also contains distinct important processing regions: the cerebellum, the pons, and the medulla oblongata. The pons and cerebellum are very important for motor control, while the medulla relays auditory, touch, and taste sensory information. Damage to any part of the hindbrain can be crippling.

Structure of the Cerebrum

The structures mentioned in the previous section are all critical to function. A small amount of damage to an area such as the pons can lead to a greater degree of disability than similar damage in many areas of the cerebrum. However, the cerebrum is the home of the most complex neural tissue, and many of the cognitive capabilities that we think of when we think of our own “selves.” Besides this aesthetic appeal, many brain dysfunctions important to humans, such as age-related cognitive decline, Alzheimer’s Disease, Parkinson’s, and many others, are diseases of the cerebrum. Study of the cerebrum can help understanding these diseases in their proper context, and how the workings of the incredibly complex cerebrum make it susceptible to insult.

The cerebrum can be separated into two sections – the gray matter cortex, containing neurons, and white matter, which contains long-range axonal pathways. The cortex can be divided broadly into lobes – the Frontal, Parietal, Temporal, and Occipital lobes, or more finely into the structurally defined Brodmann areas [See Figure 2.9]. Lobes contain areas that generally perform the same class of tasks; the frontal lobe, for example, is responsible for planning, anticipation, and executive decision-making. Though structurally defined, Brodmann areas are fairly close to functional areas identified by EEG and fMRI experiments that measure neuron excitation.

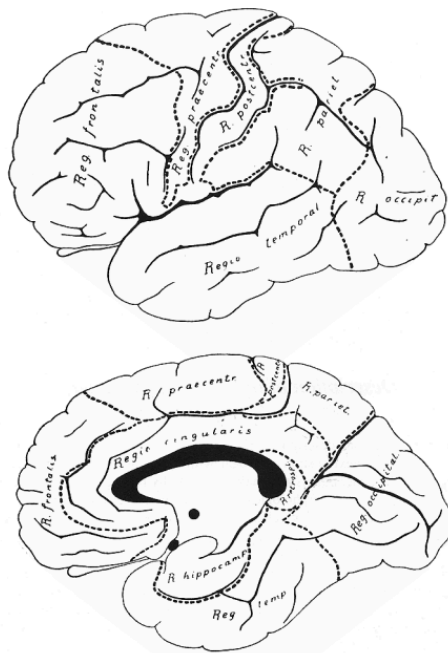


Fig. 83 and 84. The cytoarchitectonic regions of man. The olfactory region is not indicated.



Fig. 85 and 86. The cortical areas of the lateral and medial surfaces of the human cerebral hemispheres. (Sixth communication, 1907.)

Figure 2.9 Subdivisions of the cortex. Left: The cortex divided into lobes. Adapted from [Brodmann, Figure 83-84]. Right: Cytoarchitectonically distinct areas defined by Brodmann. Adapted from [Brodmann, Fig 85 and 86].

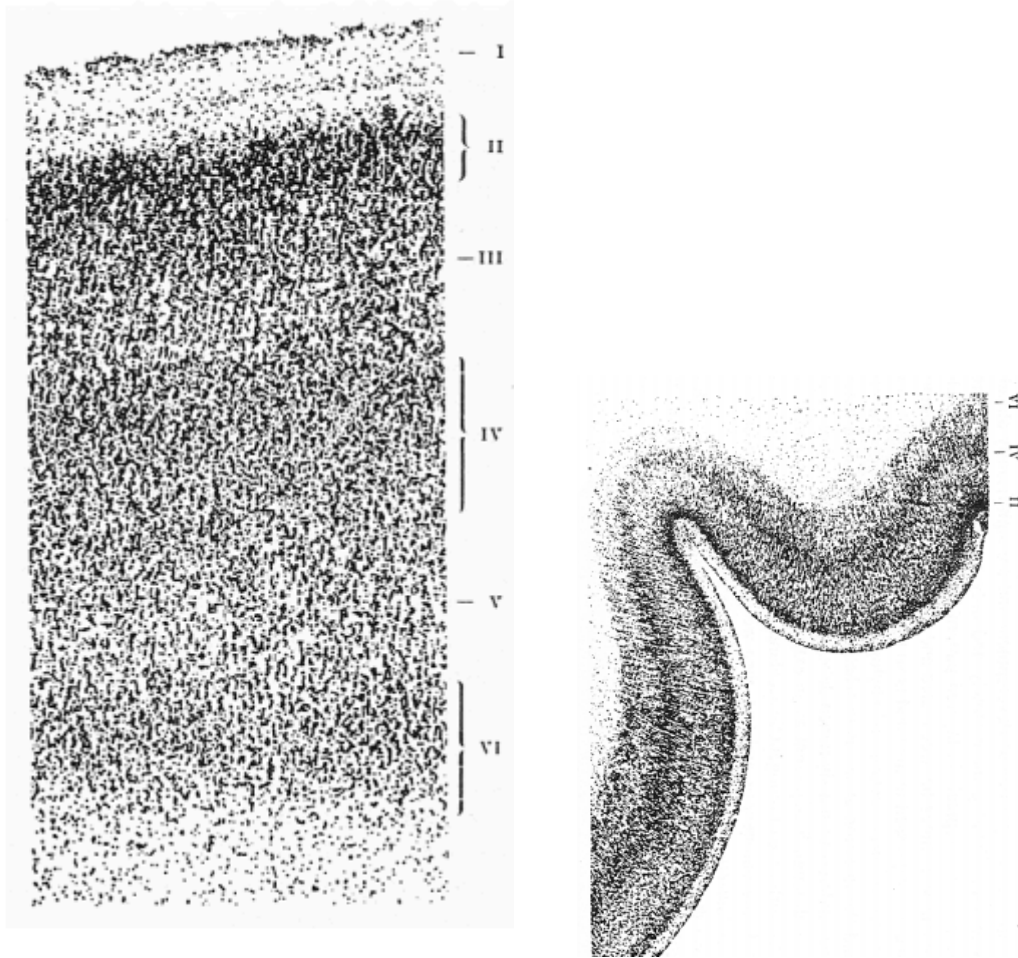


Figure 2.10 Cortical Layers. Left: Layers I-IV in early human development, adapted from Brodmann Fig 1. Right: Layers near a sulcus, adapted from Brodmann Fig 2.

Brodmann defined distinct areas of the cortex based on differences in cytoarchitecture. Primarily, these differences were in the thickness and number of layers of neurons of different types and densities. This layering reflects the different circuitry required by different processing tasks. The cortex has from two to six layers, although in some regions these layers may be subdivided. Layers are functionally specialized, for example sending information to a downstream area, or receiving feedback input [Rockland et al.]. Besides this laminar arrangement, neurons are observed to line up into

columns [Buldyrev et al.]. Neurons in these anatomical columns have a high degree of interconnectivity [Mountcastle], and may form a basic processing unit. Buldyrev showed that a decrease in the structural prominence of columns was correlated with mental dysfunction [Buldyrev, et al.], using methods from statistical physics.

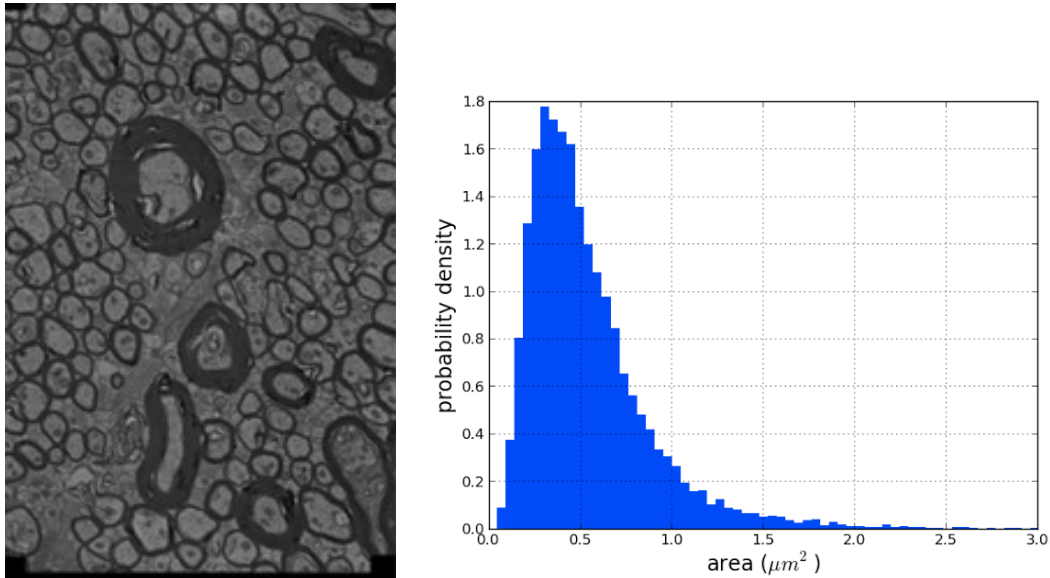


Figure 2.11 Axonal Fibers. Left: Example of axonal fibers from the fornix bundle, showing considerable variation in size [from Comin, et al.]. Right: Distribution of axon areas (not including myelin sheath) in fornix. [J. Santos, private communication]

In contrast to neuroscience's successful parcelization and organization of gray matter, the white matter remains largely mysterious. White matter occupies about forty percent of the human brain, and is composed of axons, both myelinated and unmyelinated, and oligodendrocytes. Axons vary in size and myelination, but do not display the variety of morphologies that distinguish cell bodies in the cortex. Furthermore, all sizes and myelination states appear to be mixed together [e.g. Comin et al.]. Because of this, white matter looks largely homogenous. Progress has been made

recently in identifying different fiber populations based on the proteins they express, or the proteins expressed in their insulating myelin sheathes [e.g. Campbell and Morrison], but this still has not led to recognition of any features that would allow an anatomical organization similar to that of the cortex.

Fibers are instead labeled by the regions of the cortex they connect, i.e. a fiber connecting the visual areas to the motor areas is said to be part of the visuo-motor pathway. A volume of the white matter can then be labeled by the array of fibers it contains. The organization of fiber pathways will be discussed in conjunction with our study on fiber orientation in the white matter.

3. Overview of Quantitative Tools

The description of spatial structure requires two ingredients: objects to analyze, and a mathematical framework to analyze them with. The concept of the object includes both a physical entity, composed of atoms, and its mathematical representation. For example, we may wish to analyze a set of cells. These cells *exist* in between two glass slides, in a drawer in the laboratory of our collaborators. In our analysis, they will be *represented* by a set of points.

A set of points is a very powerful representation, and it comes with a mathematical framework that has been developed by centuries worth of physicists. A point can represent an individual object, such as a neuronal cell body. A set of points can represent the result of a sampling process, such as the pixels of an image, which sample a signal such as the light from a fluorescently labeled axon.

The following section will focus on the representation of objects through sets of points, and the mathematical tools we use to quantify them. There will be other more specialized mathematical tools used in individual analyses; these will be explained in context.

3.1 Quantification of Collections Points

A point-like object is one whose only spatial property is location: it lacks any finite spatial extent. Though cells in the brain are obviously finite size, this description is often useful when defining the properties of, and comparing differences in cytoarchitecture. The effects of finite cell bodies, such as steric interference, can be observed and naturally added by considering interactions between the point-like approximations. The following

sections will discuss representation of cells as points, overview the analysis of the spatial structures of ensembles of points, and then discuss particular applications to the analysis of neural tissue.

3.2 Representation of Cells as Point-like Objects

At this point, the question becomes how to define the location of the point approximating the cell. The entire body of a neuron includes a dendritic arbor that extends over a few millimeters, and possibly an axon extending up to several centimeters. Even ignoring the difficulty in properly reconstructing entire neuronal bodies under most experimental conditions, the physical interpretation of this location is not readily apparent. A more useful choice of location is the center of mass of the soma, or neuronal cell body.

The soma can be thought of as a “home base” or “center of operations” for the neuron, both in a developmental and functional sense. During development, a compact neuron without large dendritic and axonal processes is generated from a precursor cell [Rakic], and migrates into its position in the cortical sheet, after which the soma normally maintains its position [Tyler and Haydar]. Thus somal position reflects the initial developmental “program.” Furthermore, dendritic and axonal processes are not constant over the life of the neuron, and may be lost or gained in response to the environment. Functionally, signals from the dendrites are integrated at the soma, and action potentials are generated before being transmitted down the axon. The soma also contains all of the necessary organelles necessary for maintaining the neuron [Bear et al.].

Sets of points can also be used as a representation of an extended object, for example, a set of points on an object's boundary. The object can be reconstructed by making some assumptions and interpolating between the points. A circle, for instance, can be reconstructed from any three points on its edge. We take the approach of describing the statistics of the samples as we would any other set of points, although as we will see, knowledge of the underlying objects can lead to some interesting statistical tools. This approach is generally more robust in the complex, heterogeneous environment of the brain.

3.2 Stochastic Processes and Sets of Points

If a process is stochastic, then the current state of the system defines *probabilities* for the state of the system at future time. This contrasts with a system that evolves deterministically. In general, a stochastic process can be thought of as an indexed set of random variables X_i , with each random variable part of the state of the system at a particular time indexed by i . A special case of this is the point process, which can be thought of as a binary random value indicating whether or not an event occurred. If the indexing space is multi-dimensional, this is typically referred to as a spatial point process, one-dimensional point processes usually consider evolution of a system through time. Stochastic processes can be described through the rules that govern the relationships between the X_i .

The Poisson Point Process

The simplest point process is the Poisson process, in which there is equal probability of a point being located in every small volume. This generates what is typically called a “spatially random” set of points. In this case the underlying process generating the

points can be described by a single parameter, ρ . This parameter defines the expected number of points and variance of that number in a volume V , $\langle N \rangle = \sigma^2 = \rho V$. Any deviation from this, for example increased variance, or a spatially dependent estimate of ρ , is an indication of a more complex stochastic process.

Non-uniform Point Processes

A point process can in general be spatially dependent – i.e. the probability of observing an event is not the same at every point. In a point process describing a stochastic physical system, this is a way of understanding and measuring interactions in the system. A simple modification to the one-dimensional discrete Poisson process introduces a correlation based on the last event. Say instead of every site containing a point with probability ρ , if site X_i contains an event, then site X_{i+1} contains a point with probability $\rho/2$. This in turn increases the probability that site X_{i+2} contains a point, since X_{i+1} is more likely to be empty. This is a simple model for particles with short-range repulsive potentials. The oscillating density is characteristic of liquids.

Spatially dependent processes can be split broadly into two classes: stationary processes, which are translationally invariant, and those that are not. Non-stationary processes indicate an outside influence creating a preferred coordinate system. An example might be the distribution of people over the earth. Humans are not dispersed evenly, but this is not only due to inter-human forces of attraction and repulsion. Some of the observed high and low densities are due to variations in climate and resources not determined by humans. An example in the brain would be the differential density of the cortical lamina, or a localized reduction in cell density due to injury. These outside

influences must be compensated for when estimating the relationship between points in a system.

Stationarity in reality is always an approximation, for the simple reason that our brain, and any region within it, is of finite size. However, the nontrivial properties of a stationary point process encompass some very interesting behaviors. Because variations in the probability of finding a cell in the vicinity of a point cannot be dependent on its absolute location, they must instead depend on the location of the rest of the points in the system,

$$(3.2.1) \quad P(\mathbf{x}) = P(\mathbf{x}; \mathbf{x}_1, \mathbf{x}_2, \dots, \mathbf{x}_N)$$

where \mathbf{x}_i is the location of the i th cell. This forms the basis of measuring interaction through the spatial structure of a system of particles (or cells in our case). Consider the special case of a particle added to a system of particles held fixed in a volume.

Boltzmann showed that the probability of finding a system in a given state is a function of the energy of that state, so

$$(3.2.2) \quad (\mathbf{a}) \quad P(x) = \frac{1}{Z} \exp[-E / kT] = \frac{1}{Z} \exp[-U(\mathbf{x}; \mathbf{x}_1, \mathbf{x}_2, \dots, \mathbf{x}_N) / kT]$$

$$(\mathbf{b}) \quad P(x) = \frac{1}{Z} \exp[-\sum_{i=1}^N U(\mathbf{x}; \mathbf{x}_i) / kT]$$

where $U(\mathbf{x}; \mathbf{x}_1, \mathbf{x}_2, \dots, \mathbf{x}_N)$ gives the potential energy at \mathbf{x} given a distribution of particles 1 through N , $U(\mathbf{x}; \mathbf{x}_i)$ is the energy due to particle i , and Z is the partition function.

Expression **(b)** applies to super-imposable potentials. This expression leads to the pair-correlation function, which will be discussed in detail in the following section, along

with “higher-order” correlation functions, which can describe a variety of interacting, multi-particle systems.

3.3 Descriptions of Point Processes

A description of a point process using the location of every point, as in Equation (3.2.1) would be very difficult to estimate, and very cumbersome for actual use. Fortunately, this is not necessary for physical systems with finite-range interactions. In this case Equation (3.2.1) serves as a basis for a series of enlightening approximations known as correlation functions.

N-Point Correlation Functions

Correlation functions are a statement of the joint probability. Formally, we will consider a random variable X representing the probability of observing a point in a small volume around a randomly chosen location x , and a random variable Y representing the probability of observing a point in a volume around $x+x_i$. The joint probability is thus parameterized by the vectors x and x_i .

$$P(X,Y) = P(\mathbf{x},\mathbf{x}_i)$$

(3.3.1) $P(X,Y) = P(X)P(Y | X) = const * P(\mathbf{x}_i)$

Stationarity, discussed above, plays a key part in the relationship between the distributions. This often leads to the simplification on the second line in Eq, 3.3.1. Given a stationary process, the probability of observing a point cannot be dependent on the global coordinates, so the conditional probability cannot depend on x . This leads to the definition of a correlation function:

$$(3.3.2) c_N(\mathbf{x}_0, \mathbf{x}_1, \dots, \mathbf{x}_N) = E[P(\mathbf{x}, \mathbf{x}_1)P(\mathbf{x}, \mathbf{x}_2) \dots P(\mathbf{x}, \mathbf{x}_N)]$$

where $E[\dots]$ is the expectation value. This is the full correlation function, as in [Szalay] Equation 11 (p. 166). The full N -point correlation function can be expressed in terms of simpler irreducible correlation functions, which, as we will see, can have intuitive physical meanings.

The expression for the full correlation function in Equation (3.3.1) expressed in terms of expectation values can be related to the joint cumulants of the $P(x, x_i)$. Cumulants are a way of describing a probability that are related to the more familiar moments. The cumulants of a distribution, $c_{i'}$, are defined as the coefficients of the power series of the cumulant generating function, which is the logarithm of the moment generating function. In this context the joint cumulant of the $P(x, x_i)$ can also be referred to as an Ursell function or connected correlation function. The joint cumulant is defined by the generating function [Schlosman]:

(3.3.3)

$$(a) \quad c_N(\mathbf{x}_1, \mathbf{x}_2, \dots, \mathbf{x}_N) = \left. \frac{\partial}{\partial z_1} \frac{\partial}{\partial z_2} \dots \frac{\partial}{\partial z_N} \log E \left[\exp \sum_{i=0}^N z_i P(\mathbf{x}; \mathbf{x}_i) \right] \right|_{z_i=0}$$

$$(b) \quad c_1 = E[P_1]$$

$$(c) \quad c_2(\mathbf{x}_2) = E[P_1 P_2] - E[P_1] E[P_2]$$

$$(d) \quad c_3(\mathbf{x}_2, \mathbf{x}_3) = E[P_1 P_2 P_3] - E[P_1] E[P_2 P_3] - E[P_2] E[P_3 P_1] - E[P_3] E[P_1 P_2] + 2E[P_1] E[P_2] E[P_3]$$

where P_i is defined as $P_i = P(x, x_i)$, and $P_1 = P(x)$. The first few joint cumulants are given in (b)-(d). All cumulants are independent of the offset parameter \mathbf{x}_1 , this emphasizes that because of stationarity only the relative offset between sampling matters, so we are

free to choose a coordinate system centered on the P_1 distribution. This is apparent in **(b)**, which is simply the density of the point process.

Examining the expressions in **(b)-(d)**, a recursive pattern becomes apparent. The n th cumulant is related to the full correlation function defined in Equation (3.3.2), corrected by a combination of terms appearing in lower order correlations. If the expression is rearranged to solve for the full correlation function, a physical meaning for the cumulant can be understood. For example, consider the second order full correlation function:

$$(3.3.4) \quad E(P_1 P_2) = E[P_1]E[P_2] + c_2(\mathbf{x}_2)$$

The expression $E[P_1]E[P_2] = E[P]^2$ is simply the expectation of observing events offset by the vector \mathbf{x}_2 by chance. The cumulant then reflects some “extra” probability produced by correlations between pairs of points in the point process, which justifies its common name, the pair correlation function. This function is widely used in fields ranging from solid state and statistical physics [e.g. Le Ballac] to neuroscience [e.g. Cruz]. The title *irreducible* two-point correlation function differentiates it from the full two-point correlation. The impetus for the *irreducible* name is illustrated by the three-point irreducible correlation. The probability of observing three points with offsets \mathbf{x}_1 , \mathbf{x}_2 , and $\mathbf{x}_1 - \mathbf{x}_2$ in a random point process would simply be $E[P_1]E[P_2]E[P_3] = E[P]^3$. However, unlike in the two-point case, the difference between this and the total expectation $E[P_1 P_2 P_3]$ is not simply due to interactions involving triplets of points. One must also consider the impact of pair-wise interactions between points. These contribute terms of the form $E[P_i]E[P_j P_k]$ to the full correlation function:

$$(3.3.5) \quad E[P_1 P_2 P_3] = c_3(\mathbf{x}_2, \mathbf{x}_3) + E[P_1]E[P_2 P_3] + E[P_2]E[P_3 P_1] + E[P_3]E[P_1 P_2] - 2E[P]^3$$

The $c_3(\mathbf{x}_2, \mathbf{x}_3)$ contributes extra probability from interactions that cannot be reduced to combinations of two-point interactions, hence the term irreducible.

One question that naturally arises is how many orders of correlation functions must be calculated to sufficiently characterize a point process. In many cases this can be deduced from the physics if the character of the interaction is known. If this is not the case, the mathematics of cumulants provide their own limit. The cumulant of any set of distributions containing two or more independent random variables is zero. Thus if a cumulant $c_n(\mathbf{x}_1, \dots, \mathbf{x}_n) = 0$, then $c_{n+k}(\mathbf{x}_1, \dots, \mathbf{x}_n) = 0, k \in \mathbb{N}$.

Tessellation Based Descriptions

While the correlation function approach can give a rigorous description of a point process, they can pose problems in estimation and calculability, and do not always give an intuitive reflection of the physical system. Tessellations provide a description by subdividing the embedding space of the point process into polygonal domains belonging to each point. The properties of the domains, for example the number of sides, or volume, can be computed for a number of well-known point processes and compared to the experimental distribution. For some systems, for example space-filling systems such as the growth of crystalline domains around seed points described by Pineda, et al., tessellation models offer a natural mathematical underpinning for descriptions of the system.

The Voronoi diagram subdivides a space containing a set of seeds $\{P_i\}$ into a set of domains. The domain of seed p_i embedded in the space X contains all points in X that

are closer to p_i than to any other seed $p_{i \neq j}$. In precise mathematical terms, the domain of site i is defined as:

$$3.3.6 \quad V_i = \{\mathbf{x} \in X : \|\mathbf{x} - \mathbf{p}_i\| \leq \|\mathbf{x} - \mathbf{p}_j\|, \forall \mathbf{p}_j \in \{P\}, j \neq i\} \text{ [Calka]}$$

Typically the Euclidean L_2 norm is used, however other measures can be substituted, such as the Manhattan L_1 norm, or even a transformation on the space, such as the time-based norm famously used by John Snow in his identification of the Broad Street pump as the source of London's 1854 cholera outbreak [Brody].

The Voronoi diagram can be thought of as defining density and other structural properties typically associated with an ensemble of points at the level of a single cell and its surrounding neighborhood. This gives quantitative meaning to several intuitive descriptions of structure. For example, the variance of domain size gives a measure of how ordered a system is. The variance of domain size is zero for a lattice, inversely proportional to density for a random set of points, and larger still for systems exhibiting inhomogeneities such as clustering. The Voronoi diagram defines adjacent neighbors to each cell, the number of and angles between which can be used to measure "angular regularity." [da Fontura Costa] Measurements based on the distribution of Voronoi domains will be precisely defined at the point they are used in analyses.

The properties of the Voronoi diagram of the Poisson point process have been thoroughly elucidated. They are of great utility in the study of nucleation and growth problems, such as those encountered in metallurgy, geology, biology, and ecology [Pineda]. The domain size distribution can be accurately approximated by a gamma distribution:

3.3.7 $P(V) = V^{\nu-1} \exp(-\nu\rho V)$

where V is the length, area, or volume in one, two, or three dimensions, ρ is the density of seed points, and ν is a dimension dependent parameter that takes on values of 2, 3.575, and 5.586 in one, two and three dimensions [Pineda, et al.]. This can be used to supplement tests of spatial randomness based on correlation functions, or in instances where correlation functions are difficult to implement, as we will encounter in our analysis of astrocytes. Similar formula have been developed for the number of sides of, which although very complex, are related to the Poisson distribution $\lambda^k/k!$, with mean close to six in two dimensions [Calka].

3.4 Computation of Descriptors

Two-Point Correlation Function: Radial and Vector Pair Correlation, and Estimators

The two-point correlation function comes in two flavors – the one dimensional radial distribution function, typically denoted $g(r)$, which measures the change in probability as a function of distance from a reference particle, and the more general two-point correlation function $g(\mathbf{r})$, which measures the change in probability as a function of the vector displacement from the reference point. We will use the notation $c_2(\mathbf{r})$ to refer to the mathematically equivalent second joint cumulant, when the framework of probability may increase understanding. The general correlation function has the same dimension as the embedding space. The primary advantage of the radial distribution function is that it increases the number of samples in a bin of a given size. To illustrate, in $d = 3$, the data samples that would be counted in the bin between r and $r+a$ in an estimate of the radial correlation function would be split between $4\pi r^3$ bins of size a^3 in

an estimate of the general correlation function. In the following discussions we will use the notation $g(r)$, all properties of the general correlation function hold for the radial correlation function with the substitution of $r = \|\mathbf{r}\|$ for \mathbf{r} . A slight modification of equation 3.3.4 is made to make the experimental sampling method apparent and eliminate dependence on sample size:

$$(3.4.1) \quad p[P(\mathbf{r})] = \rho^2 (1 + g(\mathbf{r})) \Delta V^2$$

Note that the meaning of P has changed – in this equation it represents a pair of points separated by \mathbf{r} . The random variables P_1 and P_2 in equation 3.3.4 are the probabilities of two spatially separated volumes of size ΔV being occupied. The left side of 3.4.1 should be read as the probability p a pair of randomly chosen volumes separated by \mathbf{r} will be simultaneously occupied, $P(\mathbf{r})$. The term $\rho^2 \Delta V^2$ corresponds to the expected number of random coincidences $E[P_1]E[P_2]$, while $g(\mathbf{r})$ introduces changes in the probability due to interactions.

The two-point correlation function can be directly computed using two general classes of methods: pair counting estimators and geometric estimators that employ a sampling window. Indirect computation is common in solid-state physics, and takes advantage of the fact that the correlation function is a Fourier pair with the structure factor, which can be measured through scattering experiments. Both classes of methods base their estimate of $g(\mathbf{r})$ on counting the number of pairs of points separated by \mathbf{r} . This count can depend on the geometry of the sampling volume, including both the shape of the boundary and existence of holes. Different estimators vary in the method used to normalize the raw count to minimize the boundary effect. This problem was first

studied in depth in the analysis of galactic surveys, notably by Peebles [e.g. Davis and Peebles], whose work was refined by many others [e.g. Szalay].

Pair counting methods take advantage of the fact that $c_2(\mathbf{r}) = 0$ for unrelated distributions. The points in a random gas are not interacting, thus spatially distinct volumes will not be related. Thus, by considering a set of random points, R , with the same density as a set of data points, D , $g(\mathbf{r})$ can be calculated by taking a ratio:

$$(3.4.2) \quad \frac{p[P_D]}{p[P_R]} = \frac{1 + g(\mathbf{r})}{1} \frac{\cancel{\rho^2 \Delta V^2}}{\cancel{\rho^2 \Delta V^2}}$$

This is of use because biases in the pair count can be caused by the shape of the sampling volume. Any biases in the data pair count introduced by the sampling region should also be present in the random pair count, and are canceled out by taking the ratio. The following discussion of pair counting methods is based on the analysis and notation in Kerscher et al. Consider a set of some points of interest (denoted D for data) in an experimental volume V . The number of pairs of points in D separated by \mathbf{r} is denoted by the pair counting function $P_{DD}(\mathbf{r})$:

$$(3.4.3) \quad P_{DD}(\mathbf{r}) = \sum_{\mathbf{x} \in D} \sum_{\mathbf{y} \in D, \mathbf{y} \neq \mathbf{x}} \Phi_{\mathbf{r}}(\mathbf{x}, \mathbf{y})$$

$$\Phi_{\mathbf{r}}(\mathbf{x}, \mathbf{y}) = \begin{cases} 1 & (\mathbf{x} - \mathbf{y} - \mathbf{r})_i \leq \Delta_i \\ 0 & \text{otherwise} \end{cases}$$

Note that the subscript i denotes that the inequality must hold for each component. The vector parameter Δ describes the binning of the count. This count is symmetric, $P_{DD}(\mathbf{r}) = P_{DD}(-\mathbf{r})$, which implies double-counting in the case of the radial correlation. Now consider a set of randomly generated points, R , of equal number to D , deposited in the

same volume. The pair counting function P_{RR} is defined analogously to P_{DD} , with points \mathbf{x} and \mathbf{y} drawn from R instead of D . Since both counts use the same Δ parameter and have the same density, we can take a ratio to obtain $g(\mathbf{r})$.

$$3.4.4 \quad g(\mathbf{r}) = \frac{P_{DD}}{P_{RR}} - 1$$

This is known as the natural estimator of the pair correlation function. It is not necessarily the best estimator of $g(\mathbf{r})$. Several others have been introduced, primarily by the astrophysics community, with the intent of increasing the rate of convergence as a function of sample size and eliminating bias, or dealing with certain types of boundary conditions. The other estimators involve the P_{DD} and P_{RR} pair counts introduced above, and an additional mixed pair count P_{DR} :

$$3.4.5 \quad P_{DR}(\mathbf{r}) = \sum_{\mathbf{x} \in D} \sum_{\mathbf{y} \in R} \Phi_{\mathbf{r}}(\mathbf{x}, \mathbf{y})$$

Note that because \mathbf{x} and \mathbf{y} are taken from different sets, we no longer need to apply the restriction $\mathbf{x} \neq \mathbf{y}$. This increases the number of DR pairs to N^2 , as compared to the $N(N-1)$ DD and RR pairs. When combining DR pairs with non-mixed pairs, it is necessary to normalize the P counts by the total number of pairs. Five popular estimators are listed by Kerscher, et al.:

$$3.4.6 \quad g_N = \frac{P_{DD}}{P_{RR}} - 1 \quad g_{DP} = \frac{P_{DD}}{P_{DR}} - 1 \quad g_{He} = \frac{P_{DD} - P_{DR}}{P_{RR}} \quad g_{Ha} = \frac{P_{DD} P_{RR}}{P_{DR}^2} \quad g_{LS} = \frac{P_{DD} - 2P_{DR} + P_{RR}}{P_{RR}}$$

the names of which, other than the Natural estimator, reflect their authors, who are, from left: Davis and Peebles, Hewett, Hamilton, and Landy and Szalay [Kerscher et al.]. The P_{DR} count can be interpreted as being a relative of the cross-correlation between the

random set of points and the data points, which could only be correlated through the effect of the sampling volume. As such, P_{DR} should be highly sensitive to bias induced by the sampling volume. Kerscher, et al. give an in-depth examination of the relative performance of the various estimators in the context of galactic surveys, concluding that boundary effects are relatively unimportant at small scales, and that at large scales the natural estimator is the most sensitive to boundary effects, while the Hamilton and Landy-Szalay estimators are the least.

However, the estimation of $g(r)$ in the brain has a few important differences. The effect of holes is very important, since neural tissue contains a large density of blood vessels. Accurate understanding of short-range behavior is relatively more important, and long-range less so, when considering the interactions of cells rather than galaxies. A comparison of estimators will be conducted in the following pages, but first a discussion of the generation of random points is necessary.

Geometric estimators have not been used in our analyses of the brain, but they will be briefly described for the sake of completeness. These count the pairs in a window, and weight the pair counts based on the intersection of the window and the total sampling volume. The isotropy of the radial correlation simplifies the form of these weights. The geometric estimator of the correlation function in three dimensions is:

$$g(r) + 1 = \frac{|W|}{N(N-1)} \sum_{\mathbf{x} \in D} \sum_{\mathbf{y} \in D, \mathbf{y} \neq \mathbf{x}} \frac{\Phi_r(\mathbf{x}, \mathbf{y})}{4\pi r^2 \Delta} \omega(\mathbf{x}, \mathbf{y})$$

$$3.4.7 \quad \omega_R(\mathbf{x}, \mathbf{y}) = \frac{4\pi r^2}{\text{area}(\partial B_r(x) \cap W)}$$

where $|W|$ is the volume of the sampling window, and $\omega(x, y)$ is the weighting function. As an example, the weighting function used by [Ripley] is the ratio of the

surface area of a sphere of radius r to the fraction of the surface area of the sphere $B_r(x)$ with radius $|x-y|$ centered at x that is inside the window W [Kerscher et al.]. Kerscher et al. state that the pair-counting estimators are Monte-Carlo counterparts of geometric estimators with appropriate weighting functions.

Two-Point Correlation Function: Computation with Pair Counting Method

Computation of the P_{AB} pair counts, with A and B some combination of the random and data point sets, is straightforward. A sample algorithm for the radial correlation function:

```
P_AB = array_of_zeros(size = Max_radius/bin_width)

for each x in A:

    for each y in B:

        P_AB[ int(|x-y|/bin_width) ]+=1
```

The time for this counting is proportional to $N_A N_B$. Statistical fluctuations can be introduced by the random points used to calculate P_{RR} and P_{DR} . To reduce the size of these fluctuations, it is typical to generate several random sets of points, and find the

average pair count at each radius over the sets, i.e. $P_{RR} = \frac{1}{N_s} \sum_{i=1}^{N_s} (P_{RR})_i$, which adds a factor of N_s to the computation time: $N_s N_A N_B$. Besides the form of the estimator, the computation of $g(r)$ is also sensitive to the method used to produce the random sets of points.

The subtlety of defining the method of producing a suitable random distribution lies in defining the probability of where a random point is placed. The most straightforward

method is to generate random points such that each infinitesimal volume has equal probability of containing a point. This generates a Poisson distribution of points. We will define this type of distribution as pure spatial randomness.

An alternative to pure spatial randomness is processes that randomize a given distribution of points. This can be done through the addition of noise, or the application of some transformation, for example randomly shuffling a time series. This is useful when large-scale externally imposed inhomogeneities produce correlations in a point process. If applied correctly, randomization should destroy the interesting small-scale structure, while preserving large inhomogeneity, allowing the correct normalization of the P_{DD} count. In the language of Equation 3.4.1, the pair probability becomes spatially dependent through its dependence on ρ . The irreducible part of the correlation can be recovered as in Equation 3.4.2 if we can obtain a random distribution with the same large scale spatially dependent density, but with $g(r) = 0$.

$$3.4.8 \quad \frac{p[P_D(\mathbf{x})]}{p[P_R(\mathbf{x})]} = \frac{1 + g(\mathbf{r})}{1} \frac{\rho(\mathbf{x})\rho(\mathbf{x} + \mathbf{r})\Delta V^2}{\rho(\mathbf{x})\rho(\mathbf{x} + \mathbf{r})\Delta V^2}$$

To make the effect of randomization mathematically precise, consider a one dimensional point process with a spatially varying density $\rho(x)$ and correlation function $g(r)$. The probability that a randomly selected point has a neighbor at $r \pm \Delta L$ can then be expressed in terms of density and the pair correlation function:

$$3.4.9 \quad p(r \pm \Delta L) = \frac{1}{N} \sum_{i=1}^N \Delta L \rho(x_i + r)(1 + g(r))$$

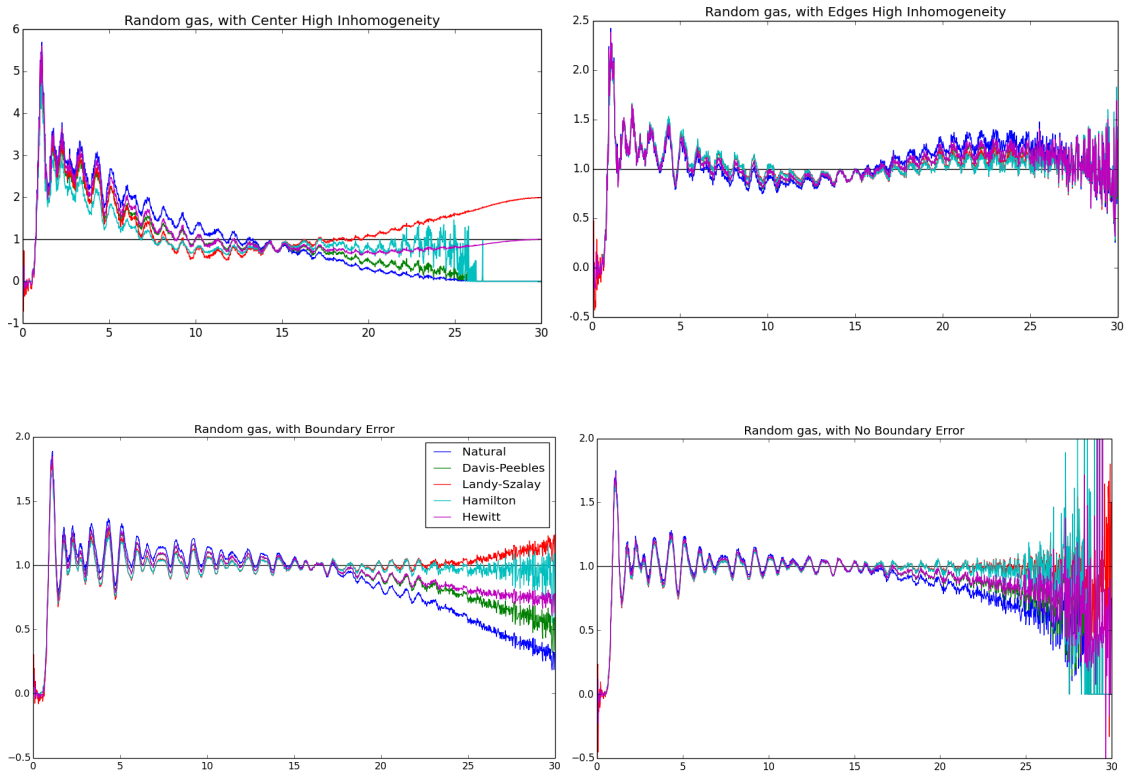


Figure 3.1. A sample of the effect of inhomogeneity on the estimation of $g(r)$. A 3D diamond lattice with vectors $(1,0,0)$, $(0.5,1,0)$, $(0.5,0,1)$ was prepared in a cube $1 \leq X, Y, Z \leq 20$, and shuffled with 16 randomly directed steps of length 0.1. Inhomogeneous density was introduced in the top row by randomly removing points with a location dependent probability. Top left: Spherical density distribution decreasing toward edge of volume, simulating unevenness due to illumination. Top right: “Hollowed out” distribution, density decreases towards center of volume as $\rho(1 - \exp[-(r-r_c)^2/2L^2])$. Bottom left: The random points were allowed to occupy the volume $-0.5 \leq X, Y, Z, \leq 20$, simulating incorrect boundary placement, or uncertainty in the boundary. Note that in this case the Hewett estimator is insensitive to the error. Bottom right: Original distribution. Each

inhomogeneity produces large background fluctuations in $g(r)$, which can cause significant difficulties in parametrization and comparison.

Now consider the addition of noise σ_i to each position. Two points with initial separation r_{ij} will now be separated by $r_{ij} + \sigma_i + \sigma_j$. This causes a mixing of the neighbor probability:

$$3.4.10 \quad p_\sigma(r) = \int_{\sigma_{\min}}^{\sigma_{\max}} p(\sigma) P(r - \sigma) d\sigma$$

and modify the right hand side of 3.4.9 to:

$$3.4.11 \quad p(r) = \int_{\sigma_{\min}}^{\sigma_{\max}} d\sigma p(\sigma) \sum_{i=1}^N \Delta L \rho(x_i + r - \sigma) (1 + g(r - \sigma))$$

In most useful experiments, the environmental influence on density varies slowly compared to the spacing of points. If the mean displacement due to noise is $\sim \rho^{-1/D}$, density will be approximately constant over the integral $\rho' / \rho \ll 1 / (\sigma_{\max} - \sigma_{\min})$. This leads to the approximation:

$$3.4.12 \quad p(r) \cong \Delta L \sum_{i=1}^N \rho(x_i + r) \left(1 + \int_{\sigma_{\min}}^{\sigma_{\max}} d\sigma p(\sigma) (g(r - \sigma)) \right)$$

In biological systems, it is very rare to observe interactions with much larger range than a few times the typical intercellular spacing, $g(r) \rightarrow 0, r \gg \rho^{-1/D}$. Conservation of probability implies that the interaction range must include both repulsive ($g < 0$) and attractive ($g > 0$) regions, and that the average over the interaction range must be equal to zero. This implies that for most biological point processes, the proper choice of σ can

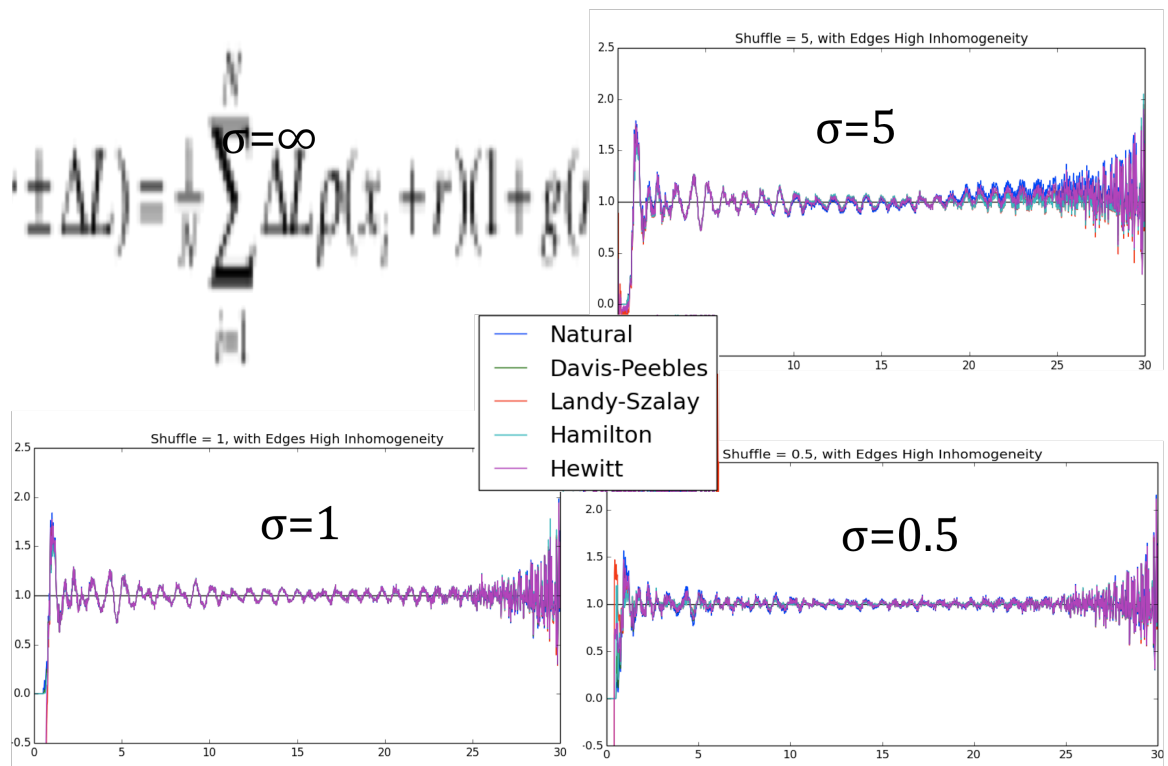
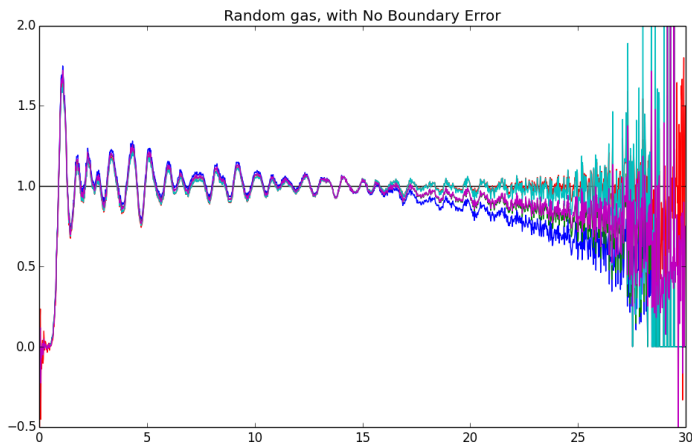


Figure 3.2 Estimation of pair correlation using shuffled normalization. A diamond lattice with vectors $(1,0,0)$, $(0.5,1,0)$, $(0.5,0,1)$ was prepared in a cube $1 \leq X, Y, Z \leq 20$, and shuffled with 16 randomly directed steps of length 0.1. The correlation function of the lattice is shown in row 1. Inhomogeneous density was induced by randomly selecting

points to be removed with the probability: $p(x,y,z) = 1 - 0.9 \exp[-(\mathbf{r} - \mathbf{r}_c)^2 / 5^2]$, with $r_c = (10, 10, 10)$. Normalizing with a purely spatially random points produced a $g(r)$ with a large background oscillation, (middle left). A shuffled set of points was produced by adding a vector with each component drawn from the uniform distribution on $\{-2.5, 2.5\}$. This range is equal to the standard deviation of the random point removal, but using it to compute P_{RR} and P_{DR} appears to remove most of the inhomogeneous effect (middle right). A smaller shuffling vector, with each component drawn from $\{-0.5, 0.5\}$ accurately estimate the correlation to long range (lower left), despite a maximum shuffling step the same size as the lattice spacing. Estimation is finally degraded with a shuffling vector with components drawn from $\{-0.25, 0.25\}$ (lower right). This estimator shows decreased peak magnitude, as the integral in the denominator of 3.4.12 no longer sums to zero. Estimators other than the Natural, which does not employ P_{DR} , show a false peak at low radius due to correlation between the shuffled and non-shuffled point sets.

cause the integral in 3.4.12 to evaluate to zero. The ratio of the noiseless points neighbor probability (Equation 3.4.9) to equation 3.4.12 gives

$$3.4.13 \quad \frac{p(r)}{p_\sigma(r)} = \frac{\Delta L \sum_{i=1}^N \rho(x_i + r)(1 + g(r))}{\Delta L \sum_{i=1}^N \rho(x_i + r) \left(1 + \int_{\sigma_{\min}}^{\sigma_{\max}} d\sigma p(\sigma)(g(r - \sigma))\right)} = 1 + g(r)$$

The precise form of the noise used to displace points (e.g. Gaussian or uniform) does not appear to cause any significant change in the estimation of $g(r)$. Simulations show that a known structure can be reliably recovered without sensitivity to the size of the noise parameter for most estimators listed above. If the range of interaction in the system is unknown, the magnitude of $|\sigma|$ is chosen to be as large as possible while maintaining

$\rho'/\rho \ll 1/(\sigma_{\max} - \sigma_{\min})$. Alternatively, the magnitude of $|\sigma|$ can be chosen to be slightly greater than the interaction range. Choosing $|\sigma|$ to be too small will underestimate $g(r)$, and cause false correlations in estimators that employ P_{DR} .

Correction of externally induced inhomogeneous density is an important consideration in the application of correlation measurements to data produced through the techniques of microscopy, histology, and immunohistochemistry. Large-scale inhomogeneities are introduced from sources such as uneven illumination, shadowing, and differences in staining agent penetration and uptake. These will be discussed in detail in the section on data collection. Uncorrected, these can have a large effect on the estimation of $g(r)$.

Three-Point Correlation Function: Extended Objects and Subsets

Consider how a set of oriented lines is different from a set of oriented pairs of points. The two-point correlation function is similar for both. It is positive along the axis of orientation up to the maximum length/separation distance. The increase in the probability of finding a point at given distance from another is equal to the fraction of pairs separated by that distance. The probability increase caused by a line of points of length L and some density λ greater than the background density ρ is different. Since every point between the endpoints of a line has an increased chance of being occupied, each line of length longer than R will contribute an enhancement, and the pair

correlation function is $g(R) \propto \int_R^{L_{Max}} \frac{\lambda}{\rho} p(L) dL$, where L_{Max} is the maximum line length and

$p(L)$ is the probability of a line of length L . However, this density enhancement could also be produced by a set of point-pairs with a suitable separation distribution. Thus there is nothing in the two-point correlation function that can uniquely identify lines.

The key to the correlation signature of lines, and other extended structures, is the implication of finding a pair of points on certain points intermediate to them: as we just stated, every point between the endpoints of a line has a high probability of being occupied. This means that a set of lines should produce a non-zero irreducible three-point correlation. Lines form the basis of our study, being the simplest extended structure, and having natural biological analogues in columns and long-range axons. We will end this section by discussing how higher order correlation functions may be used for the quantification of more complex extended structures, such as turning or branching axons.

The higher-order correlation signature of interactions involved in extended objects is useful for isolating a single interaction in a complex environment. For example, take the columns of cells that form in the cortex. Cells in a given column share the same radial glia scaffold during development. Their processes form a high density of synapses with one another, and interact in the neuropil. These interactions form the columns we identify by eye. However, there are numerous other pair interactions. Neurons from adjoining columns, and non-columnar interneurons, interact via pair-wise volume exclusion forces. Cell-cell signaling through the eph/ephrin [Marquardt et al.] and semaphorin [De Winter et al.] systems mediates the growth of axons and some neuronal migration [Rudolph et al.], and may cause other pair-wise interactions.

Angle-angle three point expectation

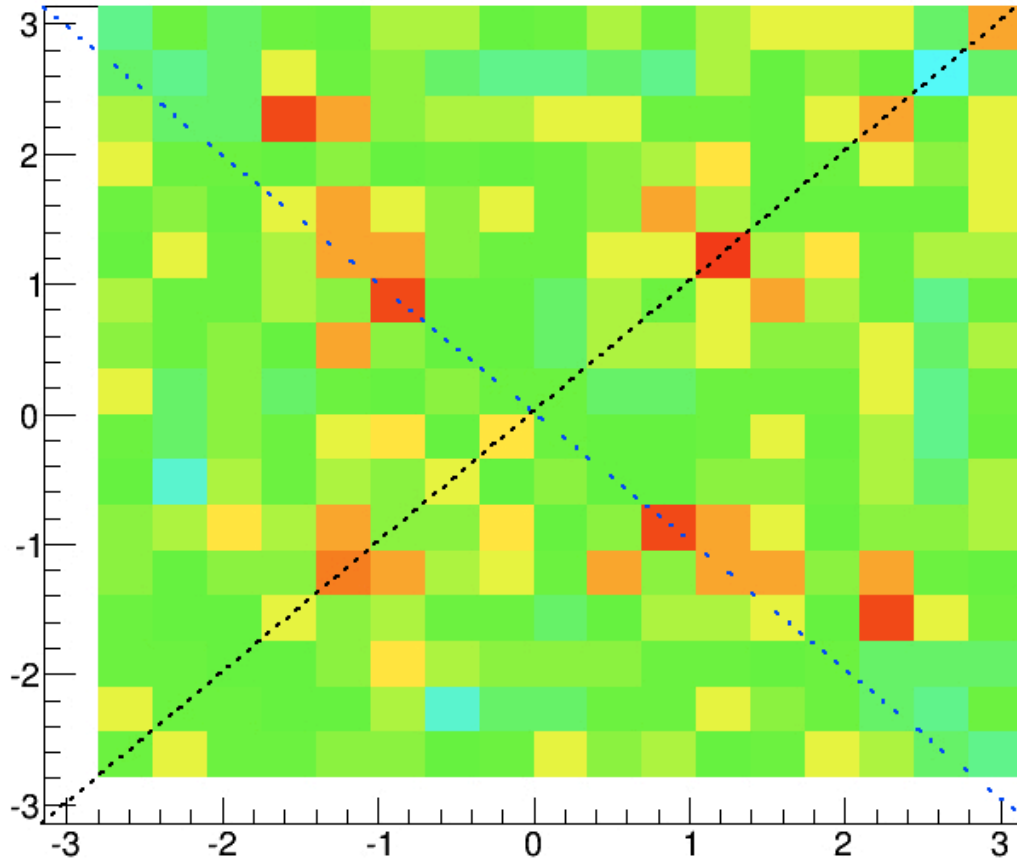


Figure 3.3 Three-point neuron correlation. The three point correlation is a function of two vectors, the displacement from the reference point to a first point \mathbf{x}_1 , and to a second point \mathbf{x}_2 . These vectors can be expressed as $\mathbf{x} = r(\cos(\theta)\mathbf{i} + \sin(\theta)\mathbf{j})$. This plot is a heat map of θ_1 vs θ_2 . The correlation shows enhancement at $\theta_1 = \theta_2$ and $\theta_1 = -\theta_2$, denoted by dashed lines. Columns of neurons in this tissue were aligned at about 60° relative to the image plane, producing a strong signal at that angle. Evidence of other lines of cells are also present.

Filling a correlation function using every combination of pairs is a demanding calculation, proportional to the cube of the number of points in the sample. Since we do not expect long range correlations to be significant, we can achieve a speed up by only considering the second set of pairs if the first is within a certain minimum distance, i.e. $R_{12} \leq R_{max}$. This reduces the time requirement to $(\rho\pi R_{max}^2)N^2$ from N^3 , where N is the number of points and ρ is the density. A sample algorithm implementing this strategy for the number of triplets at different displacements:

```

PP_DD = 4D_array_of_zeros()

for each x in D:

    for each y in D not equal to x:

        if R(x,y) < R_MAX:

            for each z in D not equal to x or y:

                PP_DD[theta(xy),r(xy),theta(xz),r(xz)]+=1

```

This is the raw number of triplets as a function of the vector from x to y and x to z . When normalized by the same quantity for a set of random points, it gives the $E[P_1P_2P_3]$ term in Equation 3.3.3 (d). The two point distribution functions can be computed in parallel, and combined as in Equation 3.3.3 (d) to compute $c_3(x_1,x_2)$.

The above example using neurons illustrates a few of the difficulties presented by the three-point correlation function. The computational constraints are obvious: sets of points typically number in the thousands, so estimation must be restricted to some subset of the full domain. The remedy offered in the sample algorithm may not be sufficient in the case of dense sets of points. We shall discuss a technique to increase the

efficiency of computation, but first we must point out another difficulty, which is the visualization of higher dimensional data.

Display of a function of more than two or three variables requires elaborate techniques, even three-dimensional representation typically uses selected two dimensional surfaces embedded in three dimensional space. A three-point correlation function is twice the dimensionality of its embedding space, making projection along one or more dimensions necessary for intelligible display. Knowledge of the interaction of interest can guide the projection, for example, in a system we believe contains lines, we are primarily interested in the subset of c_3 where $\theta_{xz} = \theta_{xy}$ and $R_{xz} \leq R_{xy}$.

The Three-Point Function and Path Probability

In a system containing continuous extended objects, the $\theta_{xz} = \theta_{xy}$ and $R_{xz} \leq R_{xy}$ projection allows an efficient computation of the three-point correlation using a technique we have dubbed Path Probability. Consider a function f that equals one in a neighborhood of radius Δ around a point. In continuous space, Path Probability (PP) can be defined as the product integral of f along a curve R as follows:

$$3.4.14 \quad PP(\mathbf{r}) = E\left[\prod_R f(s) ds\right] = E\left[\exp\left(\int_R \log(f(s)) ds\right)\right]$$

The product integral is multiplicative equivalent of the Riemann sum. The argument of the expectation evaluates to one if f is one at every point along R ; it is zero otherwise. Path probability is directly related to the three-point correlation function of extended objects. Consider a system, containing lines, whose coordinate system is a discrete lattice, such as an image produced by a microscope. We define a function f on the lattice that equals one where a voxel contains an object. We wish to compute the irreducible

three-point correlation function of the voxels $c_3(\mathbf{r}_1, \mathbf{r}_2)$, where \mathbf{r}_1 and \mathbf{r}_2 are collinear, to determine if there are lines of a given orientation and direction. To compute this correlation, we begin by testing triplets of points offset by \mathbf{r}_1 and \mathbf{r}_2 . There are four possible configurations of lines that can contribute to each point in the triplet being positive, shown in Figure 3.4.

Each of these configurations is represented by a term in the three-point expectation introduced in Equation 3.3.3¹. Configuration 1 produces the irreducible three-point

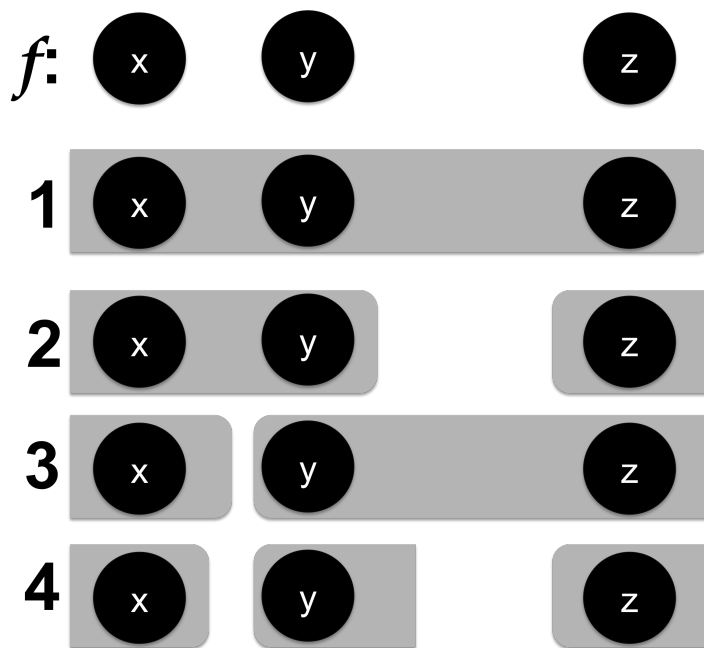


Figure 3.4. Diagrammatic representation of three-point correlation. Configurations of lines that can lead to $f = 1$ in the voxels denoted by black circles in the top line f . Values of f in other voxels considered unknown. Lines are represented by gray rectangles.

¹ $E[P_1 P_2 P_3] = c_3(\mathbf{x}_2, \mathbf{x}_3) + E[P_1]E[P_2 P_3] + E[P_2]E[P_3 P_1] + E[P_3]E[P_1 P_2] - 2E[P]^3$

correlation c_3 ; it obviously cannot be broken up into combinations of pair and single point correlations. Configurations 2 and 3 correspond to $E[P_x P_y]E[P_z]$ and $E[P_y P_z]E[P_x]$, the third two-point correlation does not contribute because there is no linear line that can connect the x and z without also intersecting the y . Configuration 4 corresponds to $E[P]E[P_y]E[P_z]$, with a line randomly intersecting each voxel.

From this single test, we have no way of knowing which interaction is causing $f(x)f(y)f(z)=1$. We can make multiple tests with the same offsets throughout the sample, and combine the averages of other tests according to Equations 3.3.3.5 (a)-(d) to solve for c_1 , c_2 , and c_3 . However, by taking advantage of continuity, we can accelerate the calculation and determine with high probability whether c_3 was responsible for the outcome of this particular test.

In configuration 1, the outcome of the test is independent of the location of the intermediate point y . In order for this to be true for the other configurations, they would have to fill the entire space by random coincidences of pairs and single points, highly unlikely unless density is extremely high or R_{xz} is small. Thus if we find the combination $f(x)f(y)f(z)=1$ for every value of y on the vector from x to z , we do not need to correct for pair and single point coincidences. It is easy to see that Path Probability performs just such a test. On a discrete lattice, Path Probability is defined as

$$3.4.15 \quad PP(\mathbf{r}) = E\left[\prod_{\mathbf{r} \in R} f(r)\right]$$

where R contains every site on the lattice intersected by the vector \mathbf{r} , and its relationship to the three point correlation function can be summarized as:

$$3.4.16 \quad c_3(\mathbf{r}, a\mathbf{r}) = PP(\mathbf{r}), \quad 0 < a < 1$$

the three point correlation function of any two collinear vectors, in a system where the irreducible three-point correlation is produced by continuous lines of objects, is equal to the Path Probability of the vector with greater magnitude.

Path Probability takes the $2D$ c_3 function (where D is the dimension of the space) into D dimensions by essentially projecting from $a = 0$ to $a = 1$ along the second argument in Equation 3.4.16. Of course this same projection would be possible if we had access to the full three-point function. Path Probability would not be useful unless it offered a large advantage in computational efficiency. Fortunately, Path Probability can be calculated using convolutions. The convolution theorem states that the convolution of two functions is the Fourier pair of the product of the function's Fourier transforms. Furthermore, Fast Fourier Transform algorithms can compute transforms in $N\log[N]$ time, where N is the number of sites in the lattice. Typically, we are interested in the three-point correlation function of a two-dimensional image of about 2000×3000 pixels, roughly 15% of which have $f=1$. If the time for the Path Probability calculation has a prefactor C_{pp} , and the full calculation has prefactor C_{3F} , then the full calculation will require more time than the Path Probability calculation by a factor of over a billion $T_{3F}/T_{PP} = C_{3F}(0.15 \cdot 2000 \cdot 3000)^3 / (C_{pp} \cdot 2000 \cdot 3000 \cdot \log[2000 \cdot 3000]) \approx 7.8 \times 10^9 (C_{3F}/C_{pp})$, given reasonable assumptions for prefactors. One caveat is that calculation of Path Probability requires a convolution for each \mathbf{r} , so the time required is proportional to the radial and angular precision.

Figure 3.4 shows a typical sample of an image from 2D confocal fluorescence microscopy of white matter tissue containing axons. The calculation of Path Probability for such an image requires three basic steps: the creation of a suitable matrix for each \mathbf{r} to convolve with the image, the convolution itself, and the computation of the product

given in Equation 3.4.16 based on the result of the convolution. In the sample algorithm that follows, the image is a binary two-dimensional array, and R is a sequence that contains tuples of the image indices that a vector from 0 to r would intersect numbered from 0 to N.

```
def PrepareRMatrix(list R):  
  
    M = matrix_of_zeros(Nrows= R[N][0],Ncols = R[N][1])  
  
    for r in R:  
  
        M[r[0],r[1]] = 1  
  
    return M  
  
def PP[image,R]:  
  
    M = PrepareRMatrix[R]  
  
    im_c = convolve(log(image)+1,M)  
  
    //each pixel x,y in im_c contains the sum of  
    //log(im[x+R[i][0],y+R[i][1]]).  
  
    //In this hypothetical sample, the computer language can  
    //handle log[0] = negative infinity  
  
    im_PP = exp(im_c) //component-wise  
  
    return mean(im_PP)
```

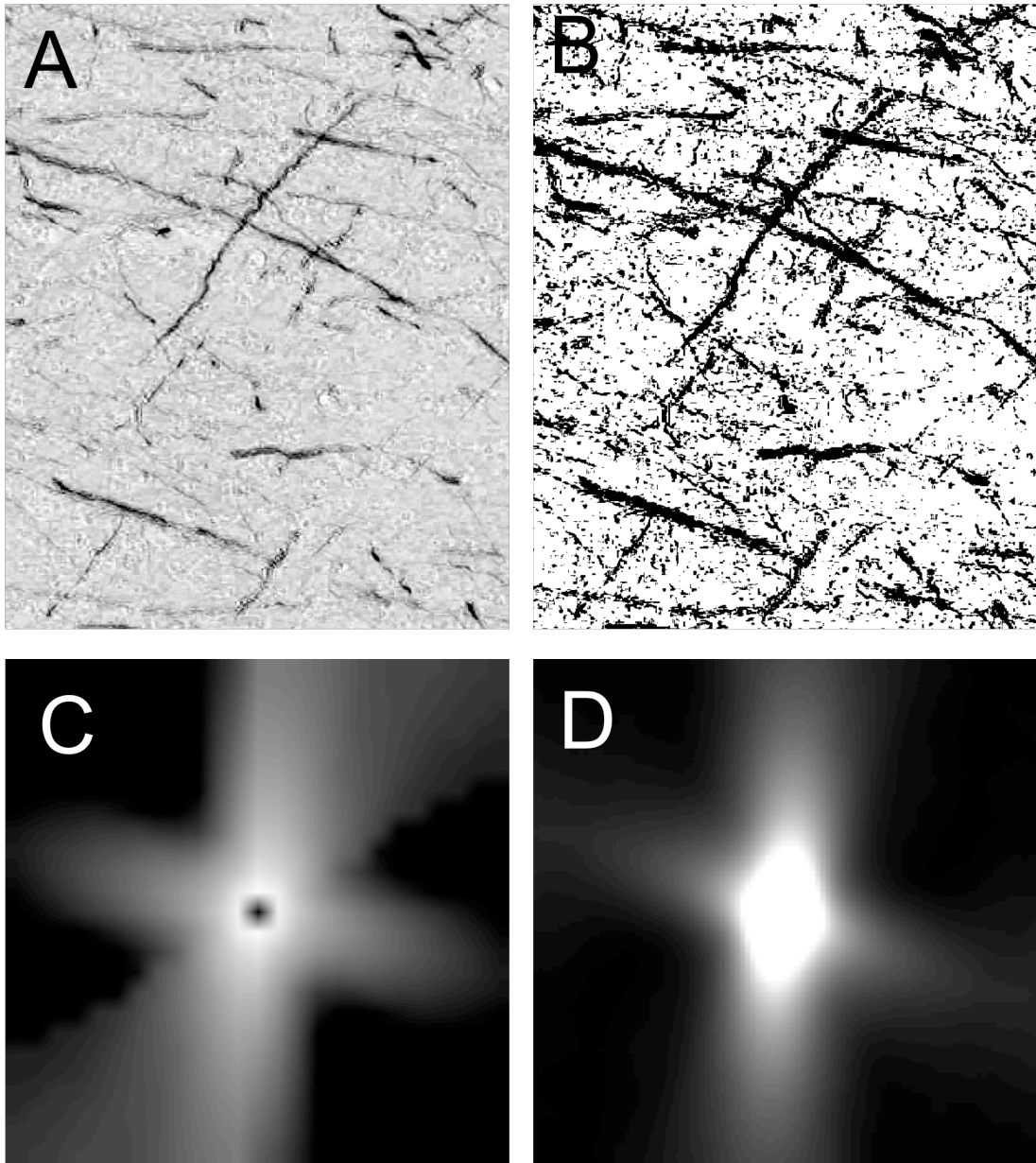


Figure 3.4 A sample of a bright field microscopy image of white matter axons. (A) is the original, (B) has been binarized by thresholding on intensity. Path Probability applied to the full image this selection was taken from results in the spectrum shown in (C). For comparison, the 2-point correlation is shown in (D) (contrast has been adjusted for visibility of lobes).

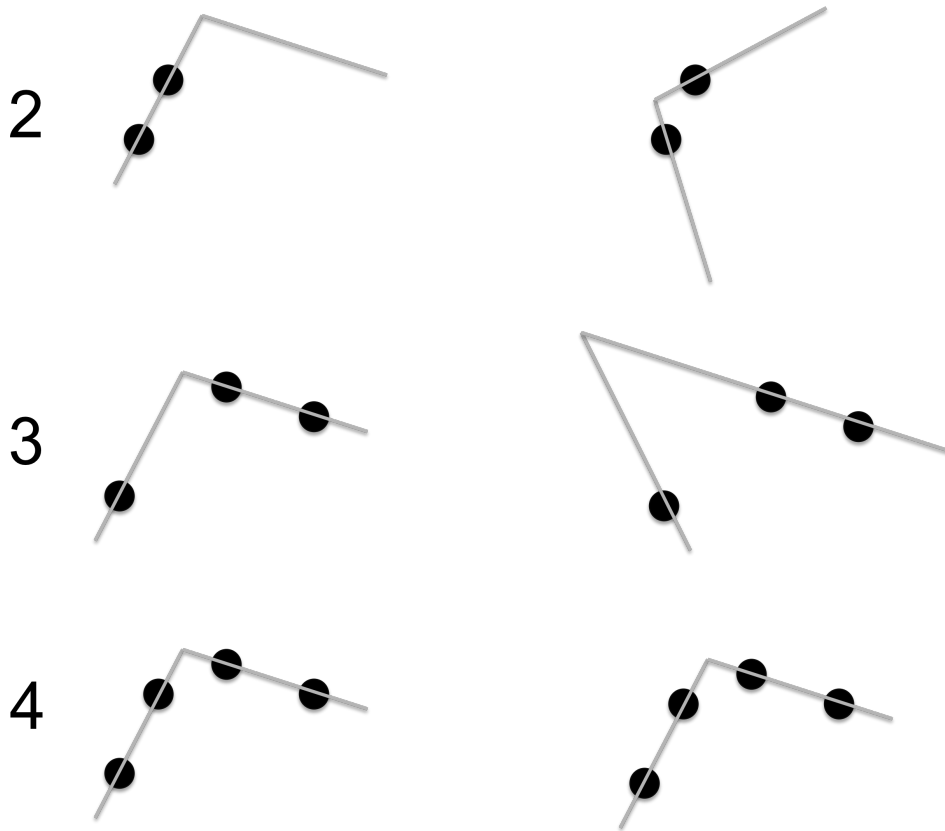


Figure 3.5. Correlation functions of complex shapes. Two linear lines, or four points can unambiguously describe a kinked line. Analogously to the linear line, the position of the two interior points does not matter, as long as one is on each side of the apex. The figure illustrates that many kinked lines can pass through a set of two or three points, however only one can intersect a set of four.

Since most efficient programming languages do not implement handling of infinities, the binary image is typically transformed by $C^*(Im-1)+1$, with C a very large number.

In summary, the three-point correlation function is a sensitive tool for detecting interactions that create extended structures. Path Probability can efficiently compute interesting subsets of the three-point correlation for linear continuous objects. It may be

possible to ease these restrictions on Path Probability, allowing for quantification of non-continuous objects, and more complex shapes. For example, an interaction may produce a line of objects with a probability of a certain number of gaps per unit length. Path Probability in this system could be adapted to produce a probability that a line of objects of length L with a given number of gaps is the result of the extended interaction. An extended interaction might produce a more complex shape. In this case, the order of the correlation function of interest is equal to the minimum number of point necessary to unambiguously describe the shape. This is illustrated in Figure 3.5.

Voronoi Diagrams

The computation of Voronoi diagrams has received extensive attention, both from mathematicians and the computer graphics community. Several efficient algorithms for constructing the diagram of a set of points in a continuous space exist. Fortune's sweep line algorithm can compute the diagram of a set of N points in two dimensions in $N \log[N]$ time using memory proportional to N [Fortune]. Many algorithms first compute the Delaunay triangulation, which is the dual of the Voronoi tessellation. An example is the construction based on the Quickhull algorithm in the QHull package [Barber et al.] In three dimensions the algorithms are generally less efficient, typically taking time of order N^2 to N^3 [Ledoux].

The native space of our spatial analyses is almost always a digital image, which mathematically is a discrete lattice. Furthermore, the space can contain holes (excluded volumes), which in general are "rough" and voxelated, and cannot be accurately represented by a smooth shape (see Figure 3.6). When measuring the volume distribution of a Voronoi diagram, in many cases it is desirable to subtract these holes

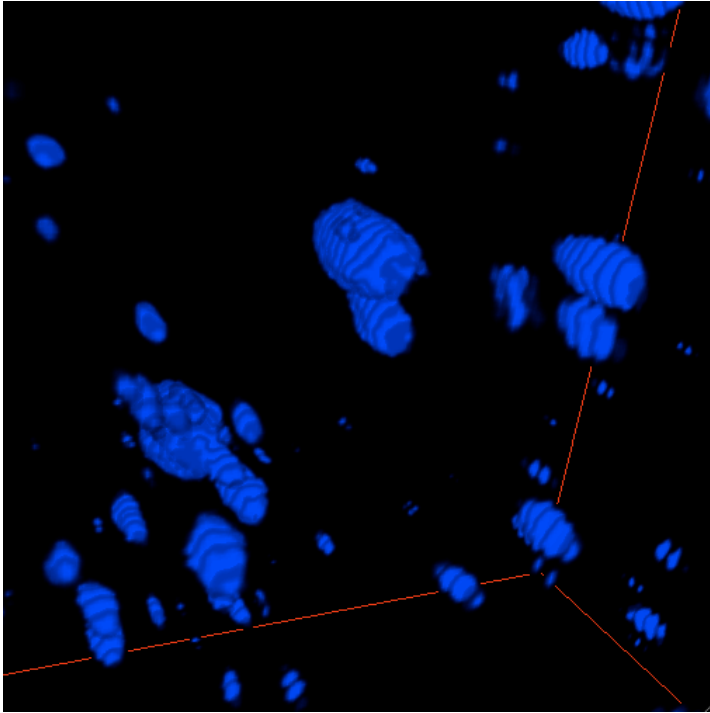


Figure 3.6. A 3D rendering of amyloid plaques, which are subtracted from the volumes of the Voronoi domains of astrocytes in our analysis. The rough boundary cannot be approximated accurately by a continuous curve.

from the individual Voronoi domains. This subtraction must be done in a discrete space, which requires a discrete space Voronoi diagram.

The discrete Voronoi diagram could be computed in a straightforward manner from the continuous one: for each site in the lattice, iterate through the domains until one is found containing that site within its boundary. This requires coding a function to check if a polygon contains a site, which can be difficult in three dimensions. Instead a simple algorithm was implemented to compute the Voronoi diagram in three dimensions. For a set of seed points S , and a three-dimensional lattice L of with N sites in each dimension:

```

for x in L:

    minDist = 2*N^2

    for i,s in enumerate(S):

        d = (x[0]-s[0])^2 + (x[1]-s[1])^2 + (x[2]-s[2])^2

        if d < minDist:

            minDist = d

            L[x] = i

```

This produces a lattice with every site numbered by the index of the seed whose Voronoi domain it belongs to. This computation takes time $N_s N_L$ where N_s is the number of seeds and N_L is the number of sites in the lattice. The time can be reduced by sorting the seeds according to position along one axis and only considering seeds within a certain distance of the lattice site, which introduces the possibility of error. The maximum distance from a lattice site to a seed can be quickly computed using the distance transform [Kimmel], if all seeds within this distance are considered then possibility of error is eliminated.

4. The Structural Response of Astrocytes in Alzheimer's Disease

Alzheimer's Disease is a progressive dementia that becomes increasingly common with age, although approximately five percent of diagnoses are "early onset," and can occur in people as young as their thirties. Alzheimer's is incurable, fatal, and expensive; it will cost the United States an approximately \$220 billion for care and medicine in 2013. As the population ages, Alzheimer's related costs will rise to an estimated \$1.2 trillion by 2050. [alz.org] Approximately 26.6 million people worldwide were estimated to have Alzheimer's in 2006, worldwide prevalence in 2050 is expected to rise to one in eighty-five, and be still higher in nations with relatively older populations [Brookmeyer et al.]

The diagnosis of Alzheimer's disease must be confirmed with post-mortem brain dissection. The pathological signature is the presence of amyloid-beta plaques and neurofibrillary tangles. Tau is a protein that stabilizes and regulates the stiffness of the neuron's cytoskeleton in axons. In Alzheimer's and some other brain diseases such as chronic traumatic encephalopathy, normal tau function is disrupted, and it forms distinctive "tangled" aggregates. Amyloid-beta is a protein fragment that is much more common in the brain's of individuals with Alzheimer's than the average healthy person. Amyloid-beta is known to be toxic to neurons, for example, some research suggests that individual oligomers assemble into trimers and n-mers that are able to form ion channels in cell membranes [Lal]. Pathologists diagnose Alzheimer's by the presence of amyloid-beta plaques, combined with the presence of tau tangles.

Glial fibrillary acid protein (GFAP) is a component of the astrocytic cytoskeleton that was first characterized by Eng in 1969 [Eng]. Since its discovery, it has become a very popular histological marker for astrocytes. Soon after this development, it was recognized that GFAP expression was markedly increased in Alzheimer's disease, [e.g. Panter, et al.] and that astrocytes in the vicinity of Amyloid-Beta plaques in particular expressed high levels of GFAP. [e.g. Burbach, et al.] [See Figure 4.1] Astrocytes are known to be a major component of the response to injury in the CNS [Fawcett and Asher].

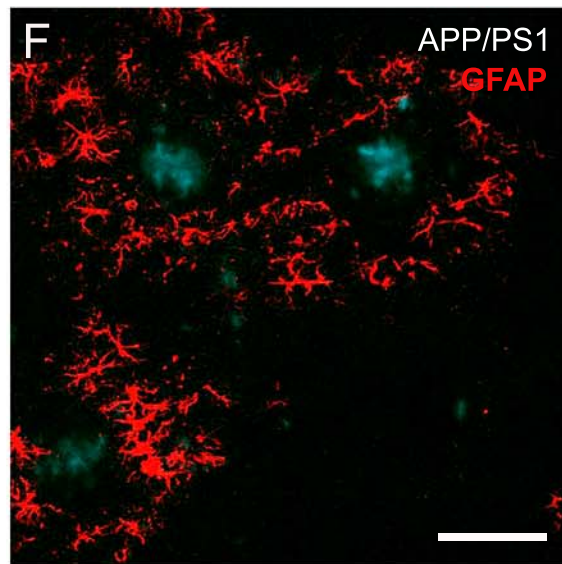


Figure 4.1. Astrocytes visualized through a fluorescent antibody to GFAP (red) appear to cluster around Amyloid-beta plaques (blue) in a transgenic mouse model of Alzheimer's disease.

This line of research led to a widespread assumption that plaques attract astrocytes. For example, many papers on Alzheimer's disease contain statements such as "astrocytes migrate to amyloid-b plaques" and "amyloid-b plaques recruit astrocytes,"

in analogy with their assumed role in other CNS insults. To summarize this line of thinking, a subset of astrocytes detects injury, and increases its GFAP expression. These “reactive astrocytes” migrate to the site of injury as part of the CNS immune response. Recent studies, however, dispute the hypothesis that this response involves an active migration.

Here we re-examine whether astrocytes migrate to plaques. Instead of relying on GFAP expression to identify astrocytes, since reactivity may be spatially dependent, we employ a pan-astrocyte antibody, sulforhodamine 101 (SR101). [Nimmerjahn et al.] This allows us to characterize astrocyte distribution in healthy wild-type mice and Amyloid-beta expressing transgenic mice in an unbiased manner. By characterizing structural changes between wild-type and Alzheimer’s model mice, we can determine the response of the global astrocyte population to amyloid-beta plaques.

4.1 Summary of Findings and Impact

The clustering of GFAP immunopositive astrocytes around amyloid-b plaques in Alzheimer’s disease has led to the widespread assumption that plaques attract astrocytes. Recent studies, however, question the ability of astrocytes to move in their natural environment. In this study we deduce the existence of migration by analyzing spatial structure of astrocytes, and its modification near amyloid-beta plaques, in a set of 3D images taken in living mice. These images are produced using 2-photon microscopy in transgenic APP/PS1 mice and wild type littermates that have had a transparent window surgically installed in their craniums. In wild type mice, cortical astrocyte topology can be modeled as a fluid with Lennard-Jones like interactions. Plaques do not appear to disturb this arrangement at a global scale, except perhaps at very large plaque

loads. Density around plaques is subtly perturbed by outward shifts of the astrocytes, in contrast with the attraction previously hypothesized. Shift magnitude is closely related to the topological distance between the astrocyte and plaque. This suggests that astrocytes respond to plaque-induced neuropil injury by changing phenotype, and hence function, rather than location.

This has significant impact on the role of astrocytes as a therapeutic target in Alzheimer's. In the paradigm of reactive astrocytes as a mechanism for reducing amyloid-beta related harm to neurons, therapeutic strategies focused on utilizing this response to mitigate harm. Astrocytes themselves are known to have many important roles in normal CNS function. This study puts forth the possibility that the reaction of astrocytes instead serves to mitigate the effect of amyloid-beta toxicity on the astrocyte system itself, and that dysfunction of this system may have a role in the cognitive dysfunction associated with Alzheimer's disease.

4.2 Experimental Design

An unbiased comparison of astrocyte structure in healthy wild-type and Alzheimer's model mice required careful consideration of experimental design. These techniques have been recently developed, and have not been previously been combined in an analysis of this nature. The experimental improvements and experimental system are described in this section.

Three-Dimensional Location Acquisition

Astrocytes are distributed throughout all layers of the cortex. Description of their spatial structure has been limited, but there are suggestions that it may be interesting.

For example, it has been observed that the processes of astrocytes do not overlap, forming discrete domains. [Bushong] Magavi, et al., have shown that astrocytes are produced by the same precursor cells as neurons, and that clonally related astrocytes are spatially localized in the cortex, suggesting that they may share a similar columnar arrangement to neurons. In order to avoid missing possible structure, it is desirable to have full three-dimensional location data (as opposed to the thin quasi two-dimensional slices common in many imaging modalities). Ideally, the field of acquisition should extend throughout the depth of the cortex.

Imaging should also acquire non-astrocyte objects that can affect the spatial distribution of astrocytes. This includes identification of the boundary below the topmost layer of the cortex, which lack neurons and has a higher than average astrocyte density, and of blood vessels, which create large excluded volumes.

In-Vivo Imaging

Most neuroanatomical studies make use of preserved post-mortem tissue. Many techniques are available to visualize cells and cellular components of interest in preserved, or fixed, tissue. Dissected brain tissue is also much more amenable for imaging using common laboratory microscopy setups. However, tissue-fixing techniques introduce shrinkage in at least one dimension, altering apparent spatial relationships.

Although this was not pursued in the current study, in-vivo imaging would allow monitoring of cytoarchitecture in the same animal throughout disease progression. Longitudinal studies of cytoarchitecture with single cell resolution could

offer new, previously unobtainable insight on cause-and-effect relationships in many processes involved in brain disease and adaptive processes.

Pan-Astrocytic Labeling

The most common target for the labeling for astrocytes, GFAP, may have differential expression in diseased and healthy animals. This makes inferences on structural changes of GFAP labeled astrocytes difficult to interpret. A label that targets all astrocytes regardless of the presence or lack of amyloid-beta pathology enables a fair comparison.

Overview of Experimental System

Cranial windows are optically transparent material, used to replace a section of the skull. Figure 4.2 shows a live mouse with the cortical surface visible through such a window. Images were captured *in vivo* through cranial windows using 2-photon fluorescence microscopy, capable of imaging up to 200 μm below the cortical surface. Astrocytes were labeled with the pan-astrocytic dye SR101. In addition to astrocytes, dense-core plaques were labeled, in order to investigate their effect on surround astrocytes, as were blood vessels, since they create a large excluded volume that can have an effect on cellular structure. Locations of astrocyte cell bodies, blood vessels, and plaques were obtained using custom image analysis algorithms. The structural relationships of these cortical components were quantified using correlation function and Voronoi tessellation methods.



Figure 4.2 A cranial window installed in a live mouse. The dorsal surface of the cortex is visible, and the dark line down the center is the division between the hemispheres. The thick ring around the window is sealant.

4.3 Experimental Methods

Animal care and preparation were performed by out collaborators in the Massachusetts Alzheimer's Disease Research Center of Massachusetts General Hospital, director

Bradley T. Hyman, PhD, MD. Dr. Elena Galea performed all experiments. Brief descriptions of these procedures are given below.

Animals and Surgery

APP^{swe}/PS1^{dE9} (APP/PS1) double transgenic mouse model (APP/PS1) mice were purchased from the Jackson laboratory (stock number 00462), and bred in house. These mice express a human mutant amyloid precursor protein gene containing the Swedish mutation K594N/M595L, as well as the presenilin 1 gene deleted for the exon 9, both under the control of the prion promoter [Verghese, et al.]. Mice were handled according to the guidelines of the Institutional Animal Care and Use Committee (IACUC). Mice, of both genders, were 5-9 months old. We used 6 wild-type (WT) and 6 APP/PS1 mice.

To install cranial windows, mice were anesthetized with 1.5% (vol/vol) isoflurane in oxygen, and immobilized in a custom-built stage with mounted ear bars and a nosepiece, similar to a stereotaxic apparatus. A 2–3 cm incision was made between the ears, and the scalp was reflected to expose the skull. One circular craniotomy was performed between the cranial reference points Bregma and Lambda [Paxinos et al.], extending to 3-5 mm on both sides of the sagittal suture, using a high-speed drill ([Fine Science Tools](#), Foster City, CA) and a dissecting microscope ([Leica](#), Wetzlar, Germany) for gross visualization. Heat and vibration artifacts were minimized during drilling by frequent application of calcium/magnesium phosphate-buffered saline (D-PBS, Gibco). The dura (the membrane internal to the skull enclosing the brain) was carefully removed with fine forceps.

The astrocyte labeling agent SR101 was applied at this point in the animal. After topical application of SR101, the window was closed with a glass coverslip (8-mm

diameter), creating a reservoir filled with D-PBS. The coverslip was sealed to the skull with a mix of dental cement and crazy glue.

Labeling Procedures

Methoxy-XO₄ was injected (4 mg/kg i.p.) one day before each imaging session to label amyloid-beta plaques (36). SR101 (0.25 mg/mL in D-PBS) was applied topically for 30 min before sealing the craniotomy with a coverslip. Fluorescein-labeled dextran (FITC-dextran, 70,000 Da; Life technologies) was injected into a lateral tail vein (0.2-0.3 ml of 12.5 mg/mL) to visualize vessels.

In-vivo Imaging

Fluorescence microscopy is an imaging technique that uses photons to excite an electron in a target dye molecule into a higher energy state. When this state decays, it emits a photon that can be captured by an imaging apparatus. Two-photon imaging is a specific technique in which the energy of the excitatory photons is one half of that required to excite the dye molecule. This means that coincident arrival of the photons is necessary to produce an excitation. This is advantageous because it allows the use of infrared excitatory light. Biological tissue has much lower absorption of infrared light, in relation to higher frequencies, allowing for much greater penetration depth, and reducing the effects of phototoxicity on neural tissue.

Images of SR101-labeled astrocytes, amyloid-beta plaques, and FITC-dextran filled angiograms were obtained by Olympus Fluoview 1000MPE with prechirp optics and a fast AOM mounted on an Olympus BX61WI upright microscope. A wax ring was placed on the edges of the coverslip of the cortical window, and filled with distilled water to create a well for an Olympus Optical 25x dipping objective (numerical aperture,

1.15). A mode-locked titanium/sapphire laser (Tsunami; Spectra-Physics) generated two-photon fluorescence with an 800 nm excitation, and three photomultiplier tubes (Hamamatsu) collected the emitted light in the range of 380–480, 500–540, and 560–650 nm. Methoxy-XO4, FITC-dextran and SR101 were spectrally separated into these three channels. Stacks of images were collected 0-200 mm below the pial surface at a 4 mm-step and 1x zoom. Typically, 5-6 non-overlapping stacks were acquired from each hemisphere.

Image Processing: Advantages and Challenges of Data Extraction from Fluorescence Microscopy

Compared to traditional microscopy, fluorescent microscopy's chief advantage is the specificity with which individual labels can be extracted. Antibodies to specific neural components of interest can be conjugated with fluorophores that emit light with a limited range of wavelengths. A detector tuned to the wavelength of a specific fluorophore can detect each component individually. Individual channels for each label are shown in Figure 4.3.

The chief challenges in identifying individual components in fluorescent imaging arise from bleed-through and uneven illumination. Fluorophores are only available with a limited range of emission spectra, most of which have peaks in the visible range. Each fluorophore's emission spectrum has a finite peak, typically on the order of 100 nm. In multi-label experiments, this means that spectral overlap is unavoidable, leading to the complication known as bleed-through. Bleed-through creates an ambiguity, in which it is impossible to tell based on signal frequency alone which fluorophore is being excited. This primarily is a problem when one label has much higher density than another, for

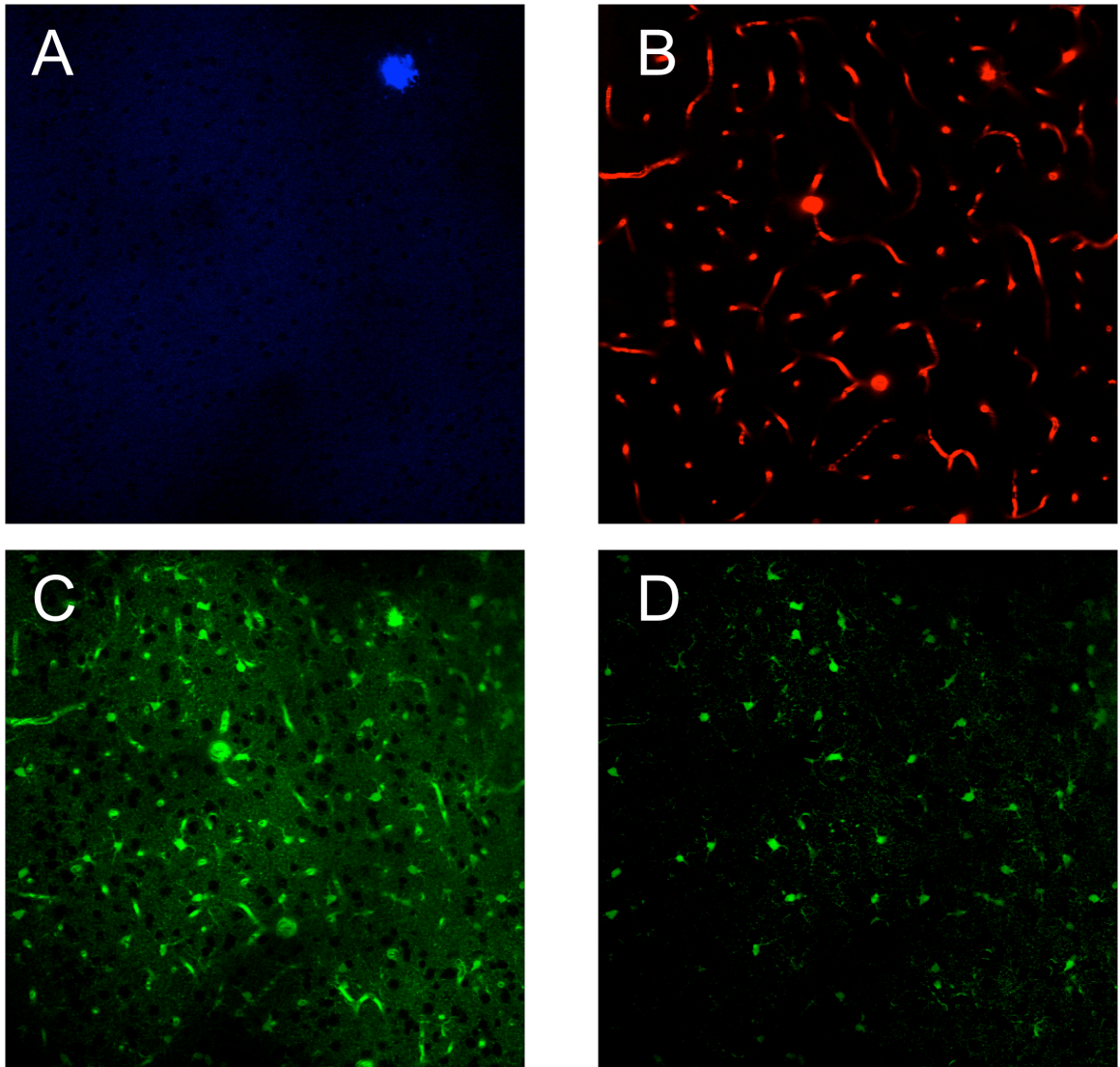


Figure 4.3 Individual fluorescent labels for targeted objects. Images are samples of typical 4 micron deep focal planes. (A) Methoxy-XO₄ labeled amyloid beta plaques. A single amyloid plaque is visible in upper right of image. (B) Flurorescein-labeled dextran label for blood vessels. (C) SR101 labeled astrocytes. Background is due to labeling of astrocyte proceses, cell bodies are high intensity globules. Extended tubular structures are blood vessels, visible in this channel due to a combination of bleed-through and end

feet (see Figure 4.9). Amyloid plaque also visible bleeding-through in upper right. (D) Astrocyte channel with blood vessel and amyloid-beta channels subtracted.

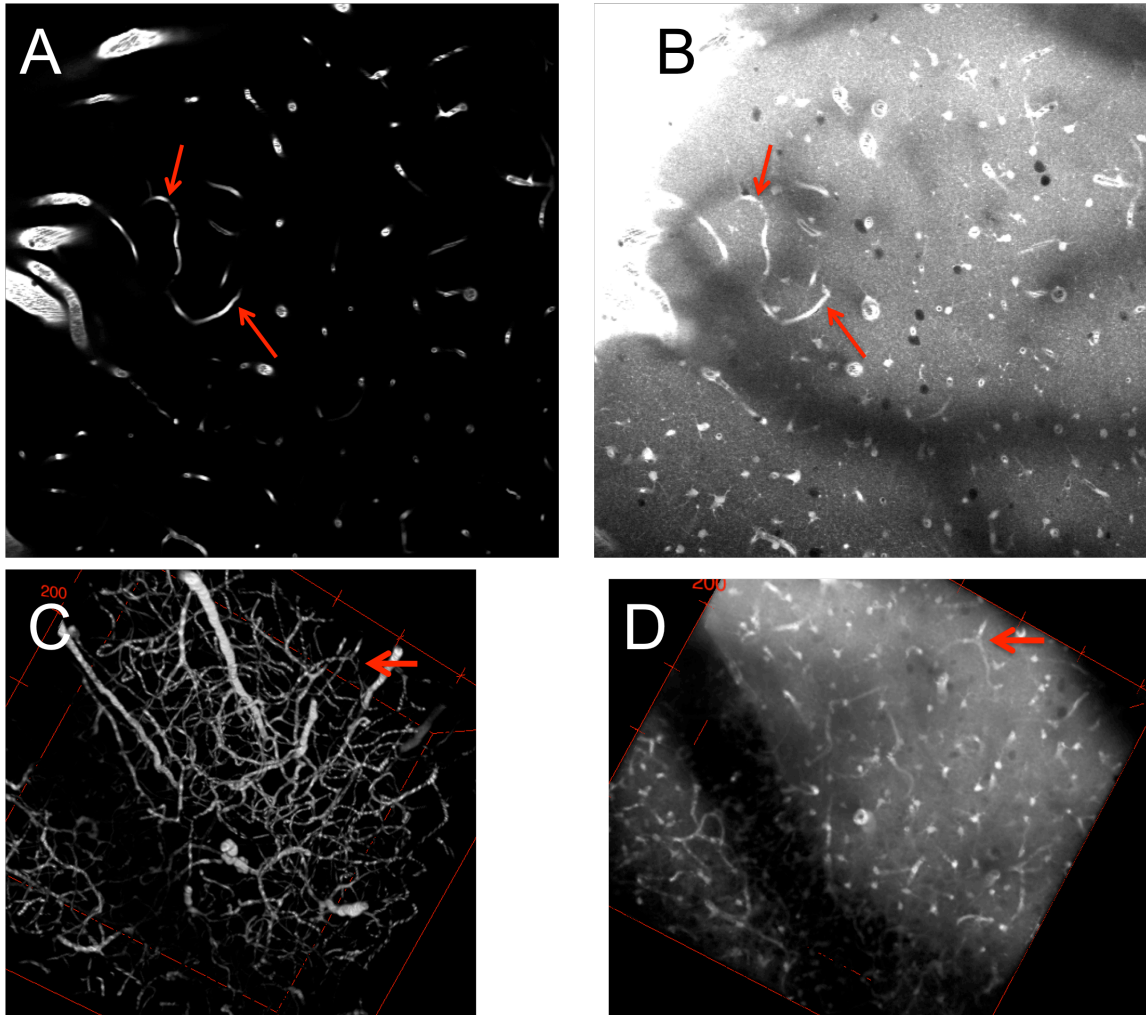


Figure 4.4 Demonstration of bleed through from blood vessel to astrocyte channel. (A) Single plane of blood-vessel channel, (B) same plane of astrocyte channel. Some distinctive objects appearing in both channels marked with red arrows. (C) and (D): 3D renderings of blood vessel channel (C) and astrocyte channel (D). Arrows again point out selected structures appearing in both channels.

example in our case Fluorescein-dextran labeled blood vessels are much more present than SR101 labeled astrocytes. The tail of the fluorescein-dextran emission spectrum in the vicinity of blood vessels creates a background complicating the extraction of astrocytes. An example is shown in Figure 4.4.

Uneven illumination is the second major challenge for data extraction from fluorescence images. The intensity of fluorescence is proportional to the intensity of the excitation laser. Although the infrared excitation used in our two-photon microscopy setup provides a broad field of illumination with good depth penetration, intensity is attenuated at the edges and bottom of the sample (see Figure 4.5). Object recognition must therefore compensate for the spatial variation in fluorescence.

Image stacks were coded in the Olympus Origin Import Filter OIF format. All data extraction was performed using ImageJ image processing software [Rasband] with the Fiji interface and algorithm suite [Schindelin et al.].

Image Processing: Plaque Extraction

Amyloid-beta plaques have distinctive morphology, and their large size minimizes the effect of bleed-through from other channels on their identification. Plaque size is a parameter of interest. It is suspected the plaque size is related to the concentration of toxic amyloid in the surrounding tissue, which may be an important determinant of the effect on astrocyte structure. Plaques have diffuse edges, with density decreasing away from the center of the plaque. Since plaques lack an unambiguous boundary, it is desirable to implement an unbiased automated method for plaque identification. Figure 4.6 shows an example of the plaque channel in comparison with extracted plaques.

Extraction Algorithm:

1. Auto-threshold stack using the intermodes method, which identifies the peaks of an assumed bimodal intensity distribution [Prewitt and Mortimer]. The automated threshold avoids bias, and the intermodes method agreed with the boundaries identified by eye.
2. Apply 3D erosion and despeckle (i.e. median filter) each plane. This removes very small objects.
3. Apply 3D dilation to reverse effect of erosion from previous step.
4. Remove plaques with radius < 4 pixels.

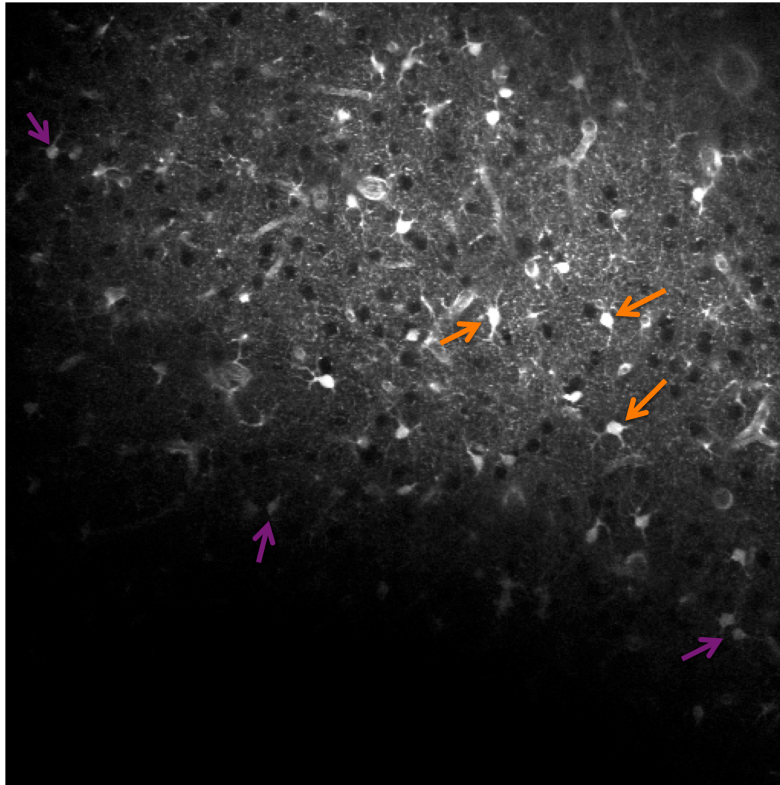


Figure 4.5 Uneven illumination causes variation in label intensity. Astrocytes near the center of the sample (orange arrows) have higher fluorescence intensity than those towards the edge (purple arrows).

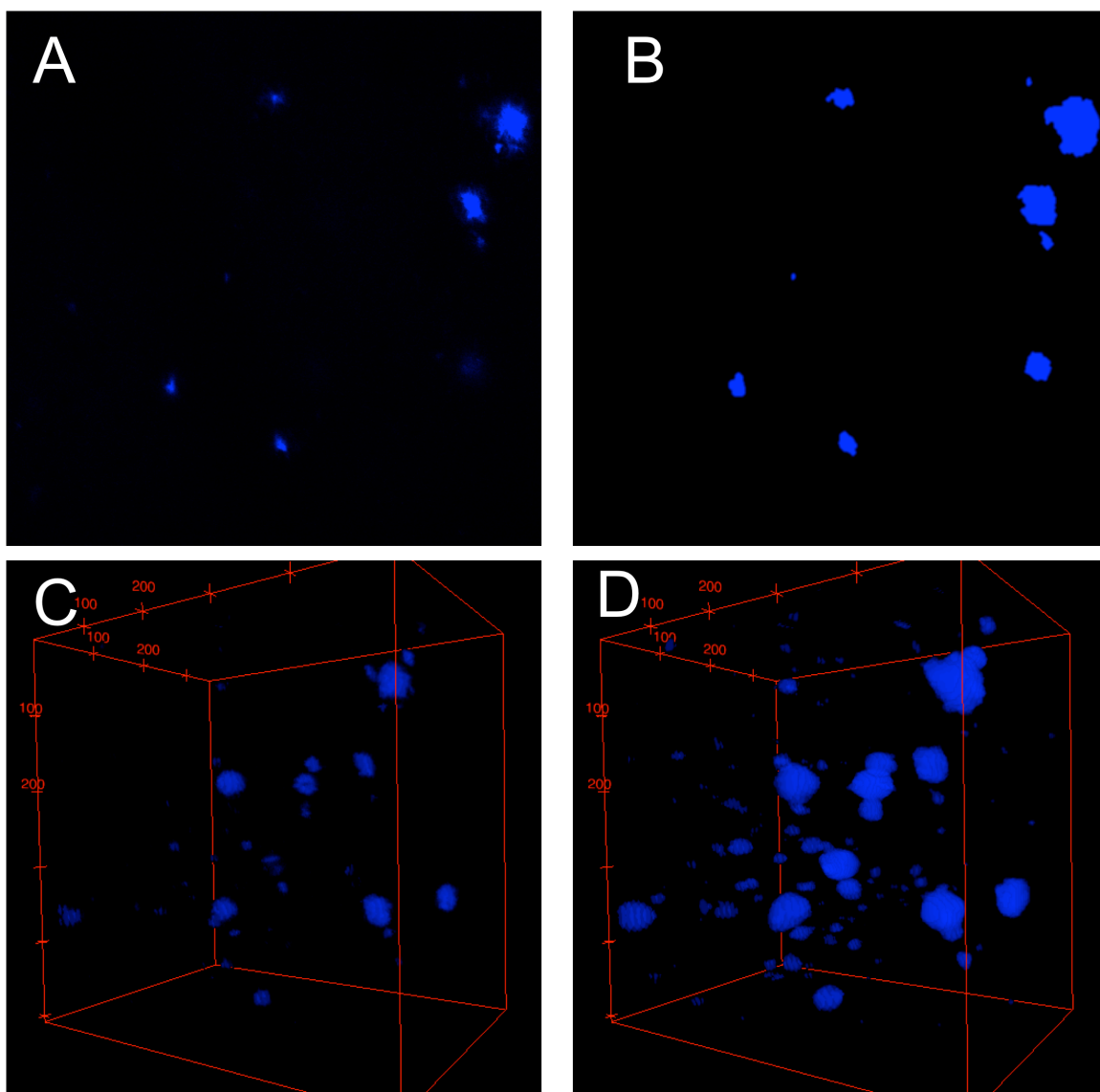


Figure 4.6 Plaque extraction. Raw plaque fluorescence channel (A) and (C) vs extracted plaques (B) and (D). Panels (A) and (B) show a single plane, while (C) and (D) are 3D renderings. Reconstructed plaque boundaries extend into the lower density region around the dense amyloid core.

Image Processing: Blood Vessel Extraction

In contrast to plaques, blood vessels have a well-defined boundary. The fluorescein-dextran injection smoothly labels blood vessels without patchiness. Because blood vessels are a large source of background bleed-through and excluded volume, it is important to identify all blood vessels. The converse of this is that it is also desirable to avoid false-positive identifications, which would cause unnecessary exclusion of astrocytes.

False positives can be avoided by recognizing that blood vessels are part of a continuous network: they cannot exist in isolation. Every blood vessel must therefore be part of a connected component that contacts the image edge.

Extraction Algorithm:

1. Smooth by convolution with a three-dimensional Gaussian kernel with a sigma of 2.0.
2. Auto-threshold using the Max-Entropy method, which maximizes the entropy between the foreground and background classes of pixels [Rasband]. Threshold is applied to each plane individually.
3. Find 100 largest 3D-connected regions. Discard any connected regions that do not contact the edge of the imaging volume.

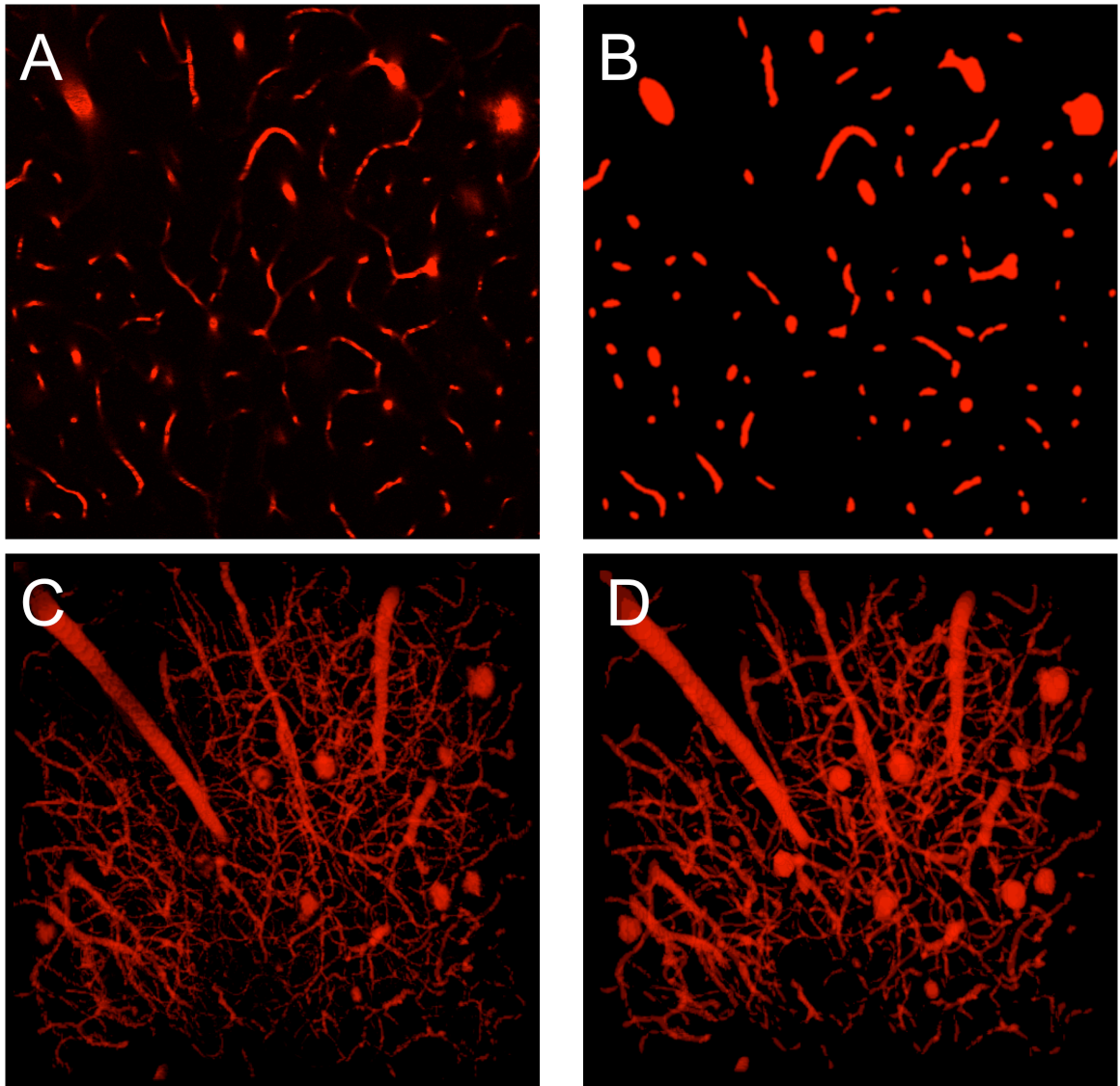


Figure 4.7 Raw blood vessel fluorescence channel (A) and (C) vs extracted blood vessels (B) and (D). Panels (A) and (B) show a single plane, while (C) and (D) are 3D renderings. Blood vessels take up a significant portion of cortical volume, which must be accounted for in analyses. Boundaries of blood vessels are well defined in comparison to those of both plaques and astrocytes.

Image Processing: Astrocyte Extraction

SR101 labels all parts of the astrocyte, including the processes. Since astrocyte processes permeate the neuropil, this creates diffuse background fluorescence, which should be proportional to *(volume of astrocyte processes per unit cortical volume) × (excitatory laser power)*. Processes are long, thin, tendrils, whereas the cell body of the astrocyte is roughly spherical with a diameter approximately 5 times that of the processes. An astrocyte cell body can therefore be discriminated from the background as a continuous region with significantly higher intensity than the background.

Two complications arise with this approach: the first being how to define what a “significantly higher” intensity is without bias, in the face of a variable background intensity, and the second being that astrocyte also exhibit a morphological feature known as end-feet. Astrocyte end-feet are thickened regions at the end of processes that form part of the blood-brain barrier. They clump together on the surface of blood vessels, and these clumps form continuous high intensity regions that could be mistaken for cell bodies. Isolated end-feet also occur around synapses, but these have volumes much smaller than cell bodies.

The unbiased definition of a significantly higher intensity is addressed through the application of a local auto-thresholding method. This method applies an algorithm to define a threshold between foreground and background based on the pixel intensity histogram from a local neighborhood around a pixel, rather than the entire image.

Astrocyte end-feet clumps are eliminated by exploiting their proximity to blood vessels. Blood vessels identified in the previous image recognition step are dilated by

two voxels. Any astrocyte candidate overlapping this dilated region is eliminated as a potential end-foot.

Extraction Algorithm:

1. Subtract blood vessel channel, and plaque channel if it is an APP/PS1 mouse, from astrocyte channel to remove fluorescence bleed through across channels
2. Smooth by convolution with a three-dimensional Gaussian kernel with a sigma of 2.0.
3. Apply rolling ball background subtraction on each plane to remove an approximately constant background (Sternberg, 1983).
4. Apply local neighborhood Bernsen auto-thresholding to each plane with a radius of 30 pixels (Bernsen, 1986);
5. Smooth by convolution with a three-dimensional Gaussian kernel with a sigma of 5.0. This has the effect of connecting nearby foreground pixels from the previous step (e.g. isolated foreground pixels will have their intensities greatly reduced, while clusters of foreground pixels will be essentially unaffected).
6. Auto-threshold using the Otsu method [Otsu] applied to the intensity distribution of the entire stack. Combined with the previous step this has the effect of preserving clusters of foreground and removing isolated pixels. No hard area cut is required with this method.
7. Dilate blood vessels previously identified. Eliminate any thresholded regions from step (6) that have non-zero overlap with dilated blood vessels.

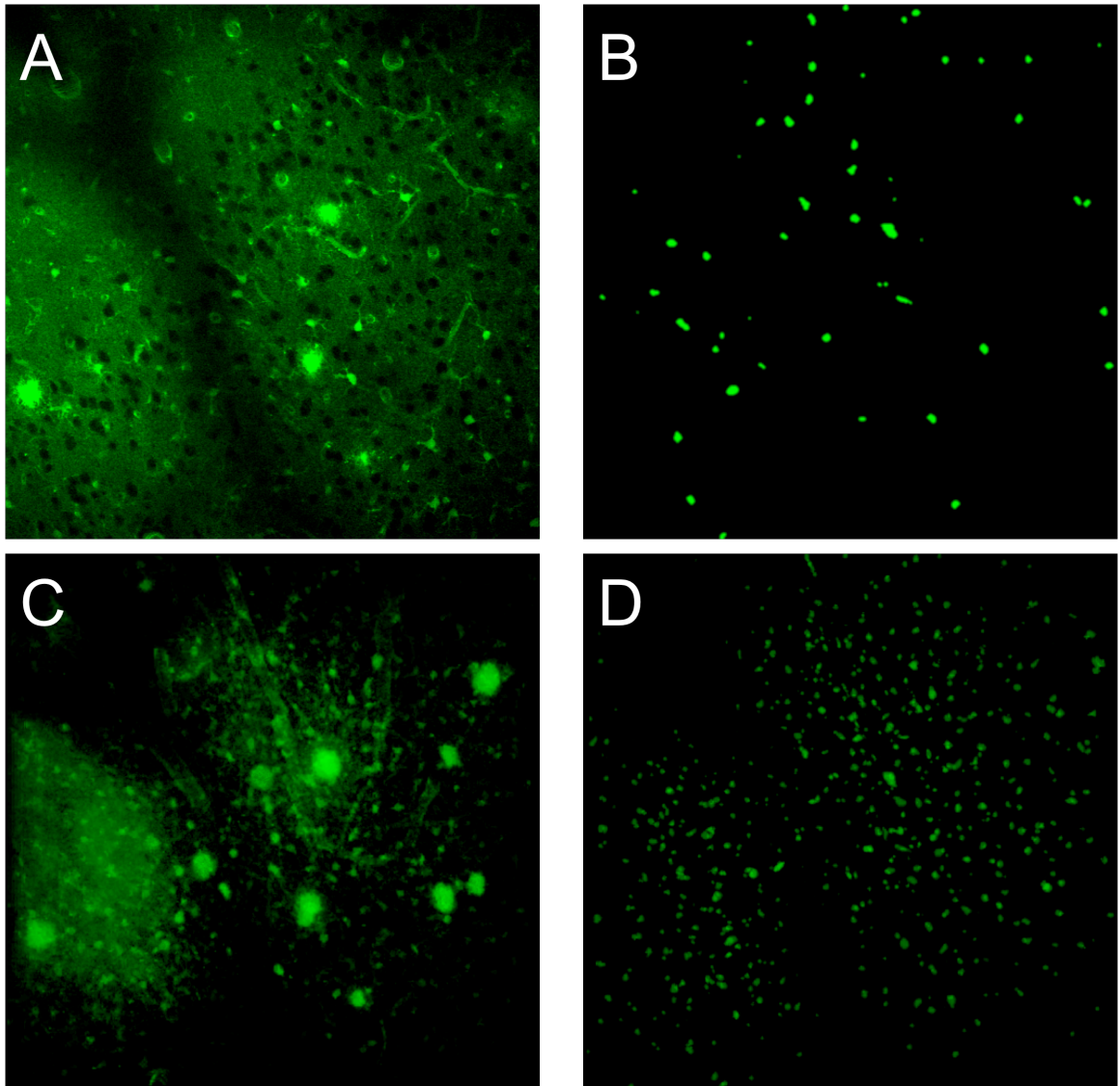


Figure 4.8 Astrocyte Imaging. Raw astrocyte SR101 fluorescence channel (A) and (C) vs. extracted astrocytes (B) and (D). Panels (A) and (B) show a single plane, while (C) and (D) are 3D renderings. The raw 3D rendering clearly shows the variable intensity throughout the stack, which has been compensated for in the algorithm. The extracted astrocytes have approximately homogenous density. Plaques and blood vessels are also clearly visible in the raw 3D rendering in (C).

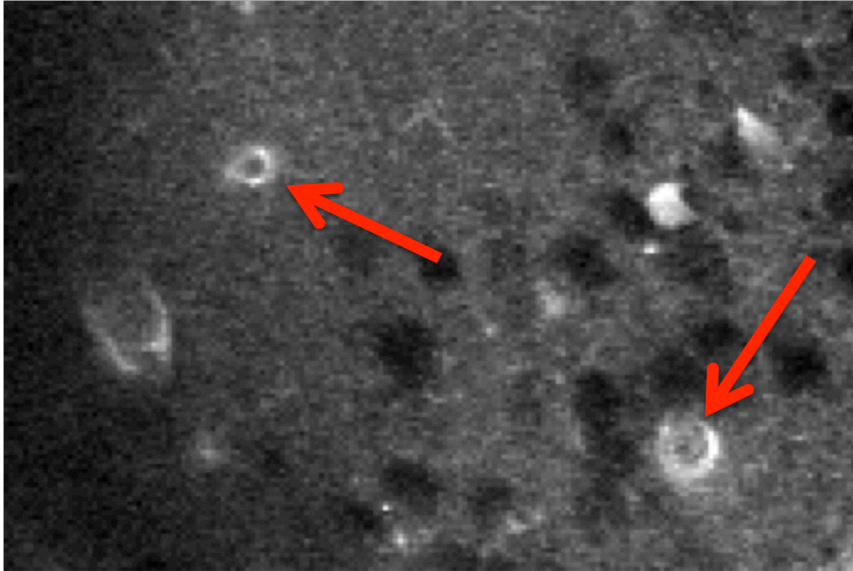


Figure 4.9 Example of astrocyte end-feet, marked by red arrows. They can be identified by their stereotypical hollow circle or C shape. End-feet can also be recognized by comparison of the astrocyte channel with the blood vessel channel.

Data Summary

From six wild-type and six APP/PS1 mice we obtained 77 usable 3D stacks (stacks were discarded if channel bleed-through was too great to overcome in astrocyte extraction). From these stacks, we obtained about 50,000 astrocytes, split approximately evenly between wild-type and APP/PS1 mice. From the 42 APP/PS1 stacks, we obtained 470 plaques. A composite 3D rendering showing plaques, blood vessels, and astrocytes together is shown in Figure 4.10.

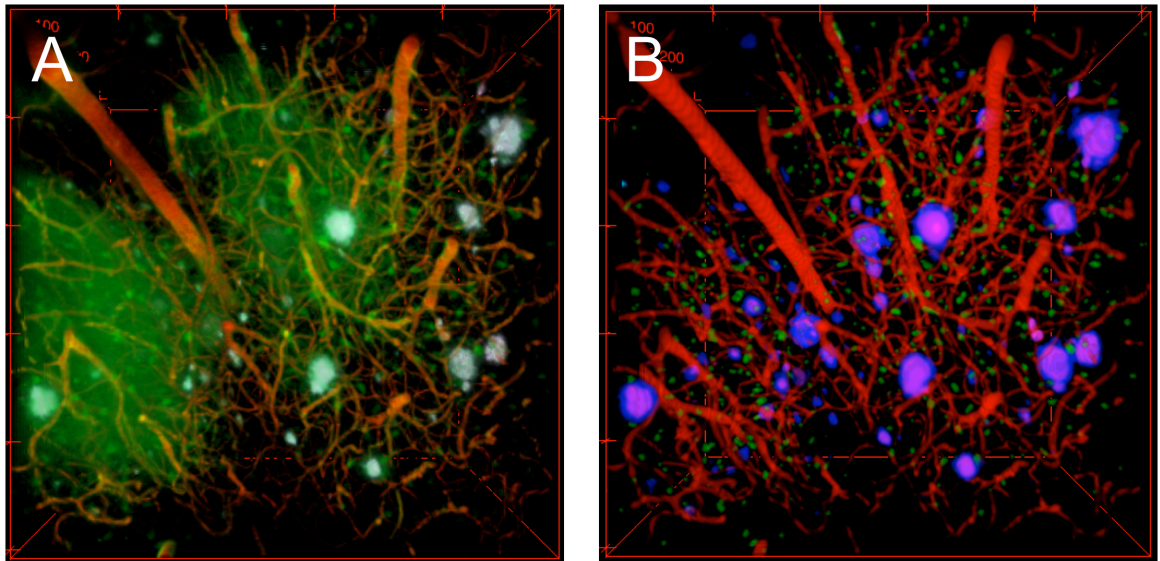


Figure 4.10 Three-dimensional renderings of composite images showing astrocytes (green), blood vessels (red), and amyloid-beta plaques (blue, bluish white). Raw fluorescence is shown in (A), and extracted objects in (B).

4.4 Astrocyte Pair Correlation Analysis

The spatial structure of astrocytes has been the subject of relatively little investigation, in comparison to the more popular neurons. Up to this point, the most well recognized observation is that astrocytes establish exclusive, non-overlapping domains: that is, the volume containing the processes of one astrocyte will not overlap with the volume containing the processes of any other astrocyte [e.g Bushong].

This implies the existence of some interaction, at least between the processes of astrocytes. It remains unknown whether the interaction that prevents processes from extending into another astrocyte's domain can exert a force on the cell body, or whether astrocytes are arranged in a manner that creates some functionally advantageous

distribution of domain sizes. For example, astrocytes might be structured such that locally high densities and voids that would naturally occur at some frequency with a Poisson point process are suppressed. Another open question is whether astrocytes are associated with the neuronal columns widely distributed in the cortex. If amyloid-beta causes a large-scale migration and reconfiguration of the spatial distribution of astrocytes, it is reasonable to expect that interactions between astrocytes during this process might be different than those experienced by immature astrocytes during development, when they initially establish their position in the cortex.

Equation 3.2.2 states that any pair-wise interaction is related to a signal in the pair-correlation function. This was thus our first avenue of analysis. An estimation of the full three-dimensional correlation as a function of the vector between each pair of astrocytes, as it should unambiguously reflect any existent columnar structure. Unfortunately, most stacks contained only a few hundred usable astrocytes, and many had as low as one hundred. Furthermore, the small size of the mouse brain leads to a cortex with high curvature, making combining correlation functions from multiple stacks impossible. If uncorrected, this curvature may have obscured three-dimensional relationships even if stacks with sufficient statistics were obtained, a fact that will have to be taken into account in future studies. Due to the curvature and limited statistics, the correlation function was only considered as a function of the radial distance between astrocytes.

To summarize the description of the pair-correlation function presented in Chapter 3.2, the pair-correlation function, $g(r)$, infers forces from the patterns they leave in the relative spatial distribution of the objects. Both the range and nature of these interactions can be measured from $g(r)$. Within the range of interaction, an attractive

force will cause clustering of objects, while a repulsive force will cause exclusion. At inter-particle distances larger than the range of the force, the distribution will return to randomness.

The pair correlation function was estimated by the Natural estimator (see chapter 3.4, Figure 3.1 for example), and normalized by a randomized point set created through the shuffling method (also described in Chapter 3.4, see Figure 3.2 for example). The Natural estimator was chosen to avoid introducing false correlations in the P_{DR} term through the use of a shuffled normalization method. A shuffled normalization method was necessary due to the inhomogeneous astrocyte density. Inhomogeneous density is

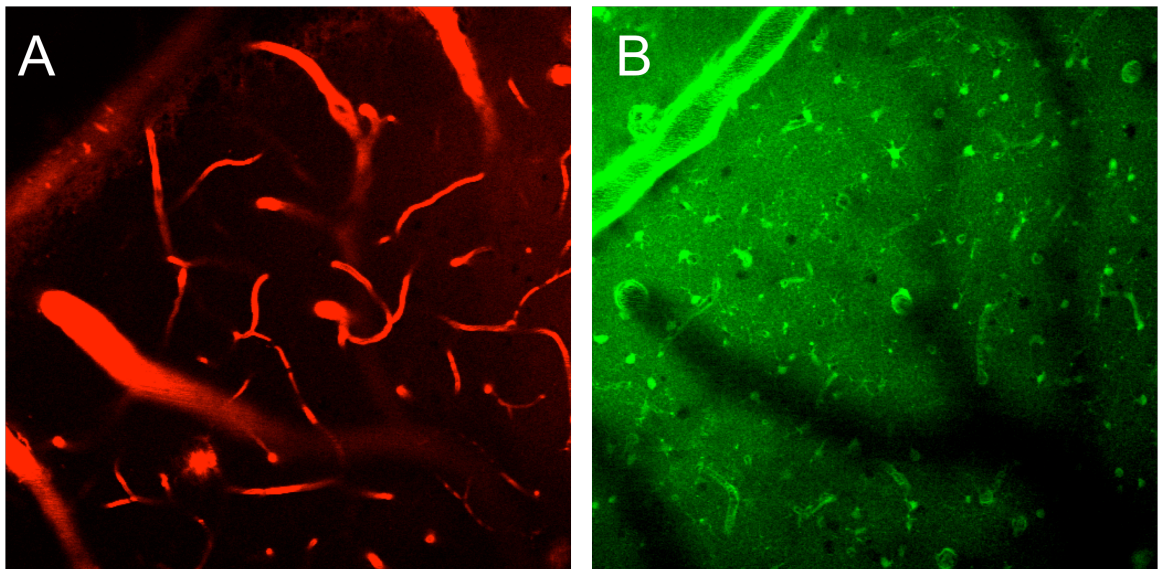


Figure 4.11. Shadowing. (A) Blood vessels near the cortical surface. (B) SR101, staining for astrocytes, 24 microns below the plane pictured in (A). The shadowed regions clearly visible in the astrocyte channel correspond to more superficial blood vessels.

caused by uneven illumination, as discussed in the preceding section, and illustrated in Figure 4.8. Another source of inhomogeneity is shadowing due to large, opaque blood vessels. Shadowing is difficult to correct for, since the blood vessels that cause the shadow do not occupy the same space as the shadow – they are above the shadowed region, towards the cortical surface (see Figure 4.11). Blood vessel identification cannot therefore identify the boundary of the excluded volume. The shuffling normalization method was used to reduce the effect of shadowed regions. A randomized point set created by shuffling the real astrocyte locations will have diminished density inside shadows, depending on the length of the randomization vectors.

Typical astrocytes in these samples were spaced about 35 microns from their nearest neighbor. A shuffling vector of 40 microns was used. As shown in chapter 3.2, this is sufficiently large enough to avoid artifact. A 40 micron vector is small enough to avoid placing a high density of random points in large shadowed regions, the region in the bottom right of Figure 4.11 has a width of about 90 microns, for example. This vector is also small enough to track inhomogeneous density caused by uneven illumination fairly closely, for example that seen in Figure 4.8. Lastly, the convex hull of the real astrocyte locations was used as the experimental volume; this ensured that the real and randomized point sets had the same density. Astrocytes in the convex hull were excluded from the calculation of the correlation function.

The $g(r)$ function was computed in 5-9-month-old WT and APP/PS1 mice, an age at which the transgenic mice have abundant plaque pathology. According to our measurements, plaques represent 0.02-0.205 % of the total brain volume in cortical layers II and III. This is below the plaque volume percentage in humans, which ranges from 0.8% up to 6% in advanced cases [Perez-Nievas et al., Urbanc et al.]. These values

represent a moderate plaque load for APP/PS1 mice. Qualitatively, under visual inspection at low magnification, astrocytes do not appear to possess a strong spatial order, although there seems to be a dearth of neighbors with low radial separations in both WT and APP/PS1 mice. (See Figure 4.12). This of course does not rule out some type of organization, for example Magavi et al.'s columnar clusters, especially given the difficulty of software based visualizations of three dimensional structure. Obvious visual evidence of a strong interaction between plaques and astrocytes is also lacking, despite the previously popular assumption of a chemo-attractant effect. SR101 stained astrocytes were not arranged in plaque-centered concentric rings, as frequently documented in studies making use of the GFAP stain. These rings were present in a brain section from a litter-mate of our APP/PS1 mice stained *post-mortem* for GFAP (Figure 4.1).

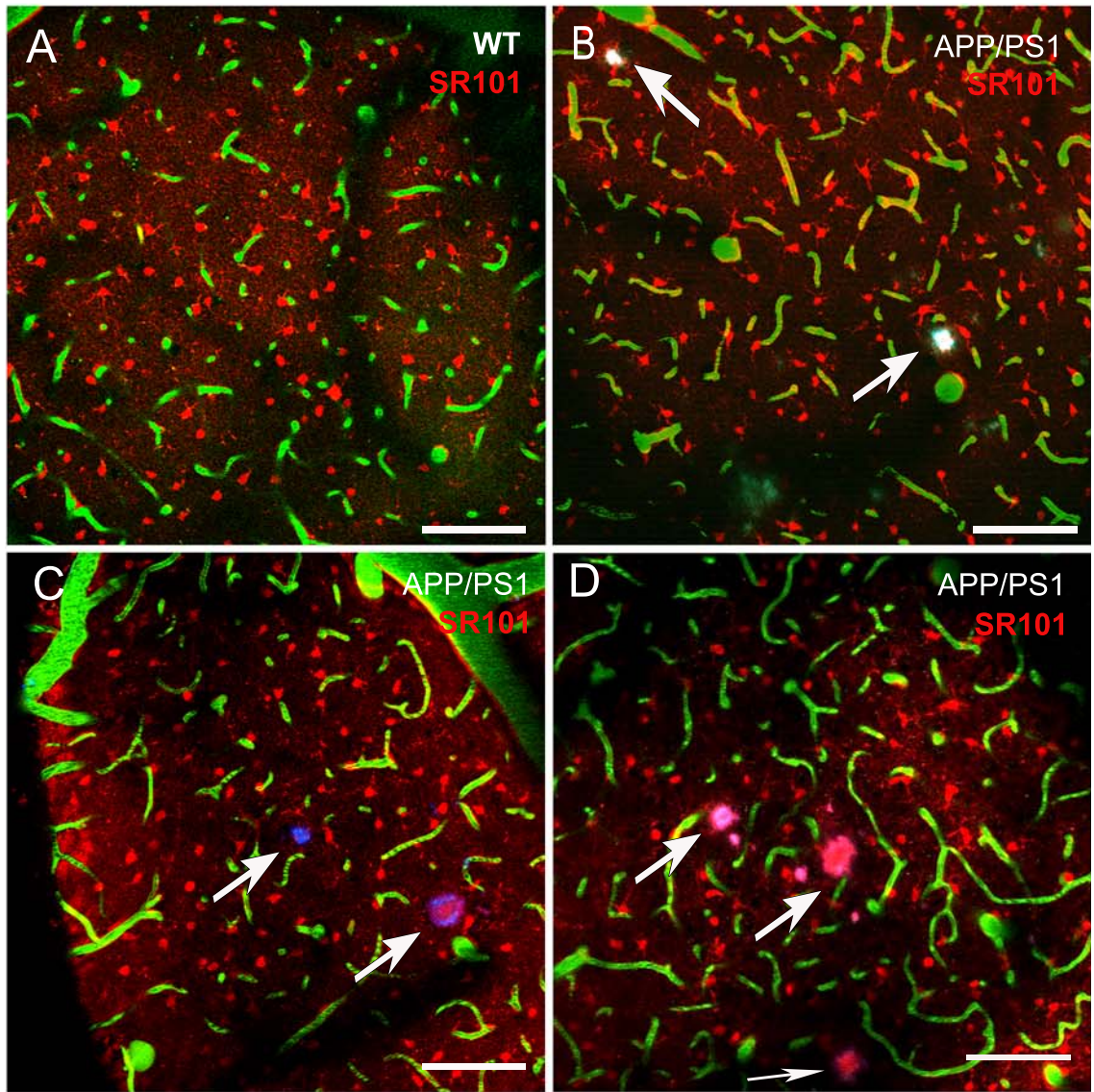


Figure 4.12 Examples of astrocytes (red) in planes from wild-type (A) and APP/PS1 (B)-(D) mice. Blood vessels are green in these images, plaques can be purple, blue, or whitish, and are denoted by white arrows. No pattern in astrocyte spatial distribution is obviously discernable.

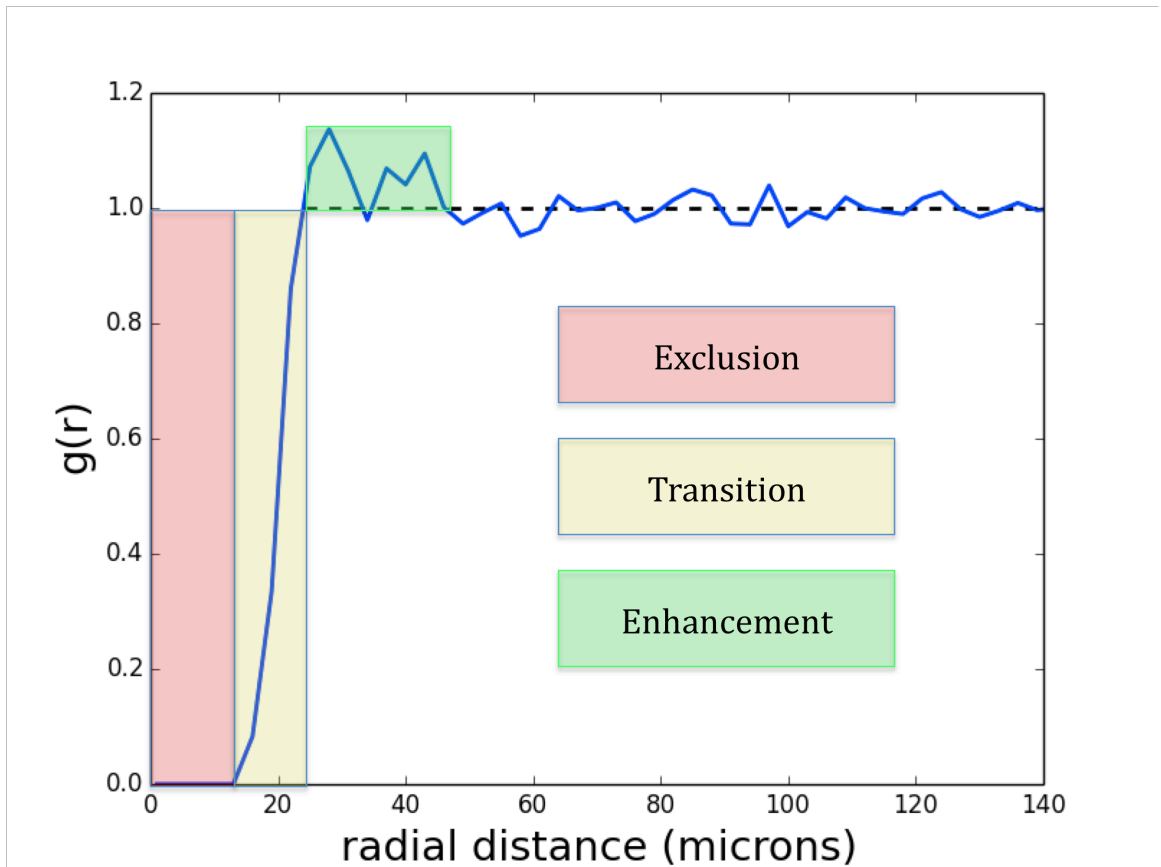


Figure 4.13 A typical astrocyte-astrocyte radial correlation function. The correlation function shows three zone: (1) Exclusion, denoted by the red region at low radius below about 18 microns, where other astrocytes are excluded. (2) Transition, denoted by the yellow region from about 18 to 25 microns, where probability of finding a neighbor increases rapidly. (3) Enhancement, a relatively broad region from about 25 to 50 microns, where the probability of finding a neighbor is higher than the probability expected in a random distribution.

All radial distribution functions for both wild-type and APP/PS1 mice had the same typical shape: a region at low radius where $g(r) = 0$, a steep transition regions, an

enhanced region immediately following the transition with one or several peaks, and a featureless region thereafter where $g(r) = 1 \pm (\text{noise})$. This is illustrated in Figure 4.13. We parameterized $g(r)$ by fitting using a hyperbolic tangent $f(x) = \tanh((x - X_0)/S)$, with center X_0 , and steepness S . (See Figure 4.14). The fitting function reaches a value of $1/2$ at $x = X_0$. This is a measure of width of the exclusion region, or the *minimum* allowable separation between the somas of two astrocytes. X_0 is calculated from the center of mass of the astrocyte soma, and astrocyte somas *without processes* are approximately $7 \mu\text{m}$ -wide (i.e. $3.5 \mu\text{m}$ radius). This means the range of the exclusionary interaction cannot be due to the steric effects of the cell body. The parameter S measures the steepness of the transition region, with larger S corresponding to a shallower slope. S is proportional to the variability in the inter-astrocyte separation (Fig. 2D). Unfortunately, this study lacked sufficient statistical power to reliably characterize the width and magnitude of the enhancement region. Figure 4.13 shows an example of $g(r)$ from an animal with a larger than average number of astrocytes, and even in this animal the signal-to-noise ratio of the enhancement region is close to unity. Future studies should focus on obtaining sufficient statistics for this region, as we shall see that it appears to be a non-trivial consequence of the specific long-range interaction between astrocytes, and may therefore be functionally important. For example, the interactions that create this enhancement may suppress the existence of large voids, as compared to the case of simple hard spheres.

The spatial distribution of astrocytes resembles a liquid of polydisperse hard spheres. Hard spheres also exhibit an exclusion region, at separation distances up to $2xR$, where R is the sphere radius. The radial correlation of hard spheres with uniform radii displays a discontinuous transition, with $g(r) = 0$ for $r < 2xR$, and $g(r) \geq 1$ for

$2xR < r < (2+\Delta)xR$, where Δ is a fraction determined by the packing density of the system [Santos]. This abrupt transition is relaxed in a system of spheres with a polydisperse radius distribution. A hard-sphere liquid also displays a density dependent peak following the exclusion region. We will find, however, that the shape and size of the peak observed in astrocytes cannot be explained through hard-sphere interactions.

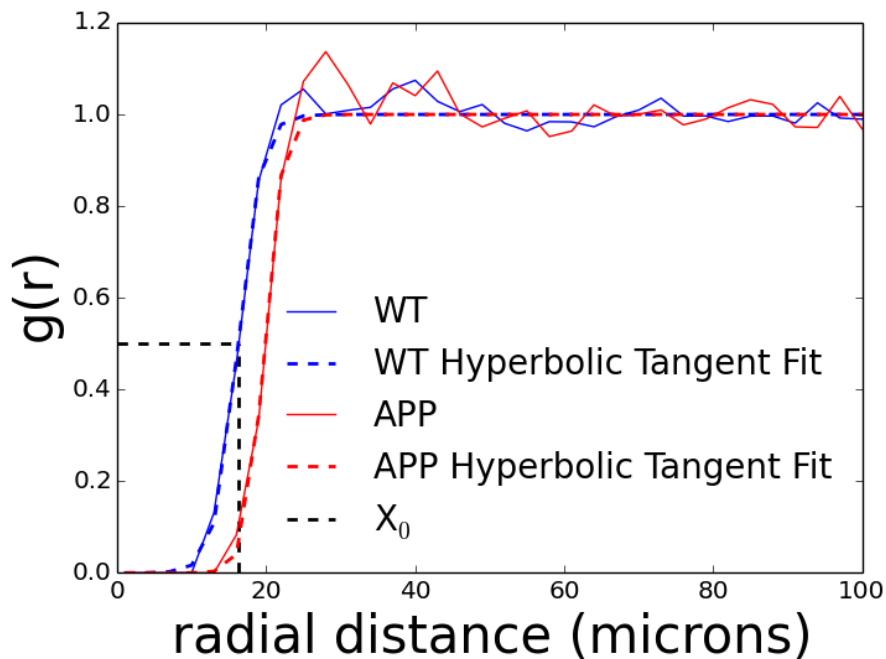


Figure 4.14. A demonstration of the fits using a hyperbolic tangent on typical radial correlation functions from wild-type (blue) and APP/PS1 (red) mice. Black lines denote where X_0 is measured, S is extracted from slope of the hyperbolic tangent. In this particular example, X_0 is greater for the APP/PS1 mouse, and S is approximately the same for both.

Since both wild-type and APP/PS1 mice exhibited the same basic set of regions in their radial correlation, we checked if the size of these regions varied. In wild-type, $X_0 = 17.61 \pm 1.25$ mm and $S = 2.89 \pm 0.57$ mm (means \pm SEM, $n=6$). Plaques occupy volume and would therefore reduce the available volume for the spheres. At the observed plaque loads, however, the effect of this effective reduction in volume would be expected to be negligible. The radial correlation function of astrocytes does not show the oscillations that indicate the stacking interactions important in higher density fluids, which would make volume reduction significant. Typical spacing between astrocytes is about $4X_0$, and with plaques occupying about 0.2% of the cortex at most, the volume reduction alone should not lead to any rearrangement. Simulations of hard sphere fluids confirm that at high densities, the addition of an immobile foreign body representing a plaques will prevent efficient packing, leading to slightly lower astrocyte density in the surrounding region.

The spatial structure of astrocytes may be altered however, if we consider the possibility of attractive or repulsive interactions between astrocytes and the plaque. Astrocytes competing for energetically favorable positions, either close to (attractive interaction) or far from (repulsive interaction) plaques would interact strongly with one another. If astrocyte interactions remain unchanged, this competition would produce a large effective volume reduction, causing astrocytes in favorable regions to adopt a close-packed configuration, indicated by a peak in $g(r)$ at X_0 . It was also hypothesized that plaques and compression of astrocyte may reduce the ability of astrocytes to repel one another, resulting in both a smaller S and X_0 . However, function appearance and parameters for APP/PS1 mice were $X_0 = 17.51 \pm 1.16$ mm and $S = 2.96 \pm 0.46$ mm (means \pm SEM, $n=6$), values not significantly different to the ones computed in WT mice (Fig. 2C, D).

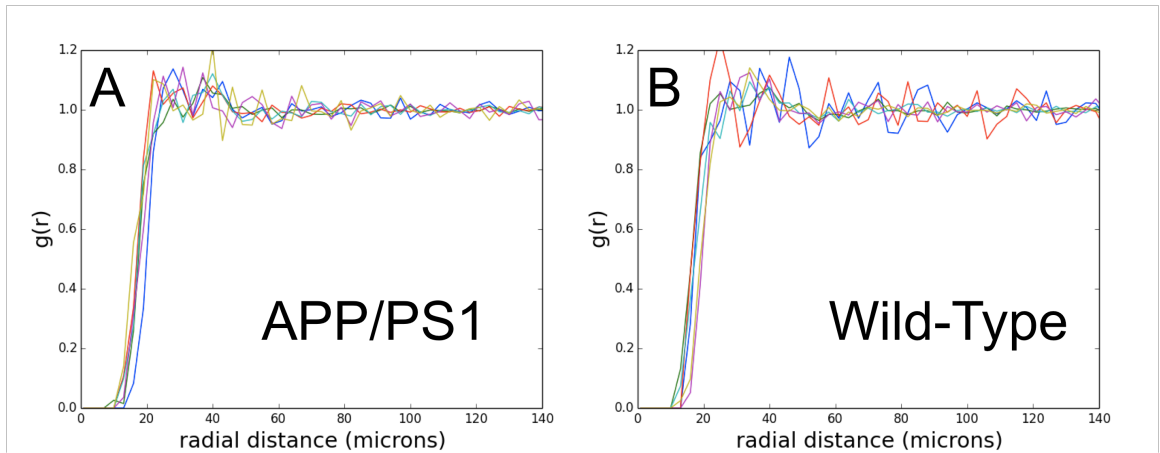


Figure 4.15 Comparison of radial correlation functions of APP/PS1 mice (A) and wild-type (B). Fit parameters: APP/PS1 mice: $X_0 = 17.51 \pm 1.16 \mu\text{m}$ and $S = 2.96 \pm 0.46 \mu\text{m}$ (means \pm SEM, $n=6$), Wild-type $X_0 = 17.61 \pm 1.25 \mu\text{m}$ and $S = 2.89 \pm 0.57 \mu\text{m}$ (means \pm SEM, $n=6$). Although fitting was not performed, enhancements region shape and magnitude appears consistent in APP/PS1 and wild-type mice, especially if correlation functions with high noise (red and blue lines wild type, yellow APP/PS1) are ignored.

These results suggest that plaques do alter the interactions between astrocytes, and that the magnitude of the attraction, if any, is not large enough to change their spatial structure on a global scale. However, plaques represent only up to 0.205% of the brain volume in the mice analyzed. This raises the possibilities that only a small subset of astrocytes is affected at this plaque load, or that not enough astrocytes migrate to be forced into a close-packed configuration. To address these possibilities, we asked whether plaques disturb the spatial structure of the astrocytes closest to the plaque. This is accomplished by examining the size of domains defined through the Voronoi

tessellation as a function of their distance from plaques, and by simulating the effect of larger plaque loads on $g(r)$.

4.5 Astrocyte Voronoi Tessellation Analysis

Analysis with the pair correlation function shows that the global distribution of astrocytes is not altered by the presence of plaques. The possibility remains, however, that plaques alter the local spatial structure of astrocytes. One tool with which this could be studied is the plaque-astrocyte cross-correlation function, which is analogous to the normal pair correlation, except that we consider the radial separations of mixed plaque-astrocyte pairs. This was unfeasible because of the low number of plaques per stack, and their apparent tendency to cluster, which complicates the production of a good normalizing point distribution. A correlation function also discards some potentially useful information on the distribution of densities at each distance, using only the mean.

An alternative analysis makes use of Voronoi tessellations, reviewed in Chapter 3. The Voronoi tessellation subdivides a space into separate domains, one per astrocyte. Voronoi tessellation has been used before to study the spatial arrangement of neurons [e.g. Duyckaerts and Godefroy], and has some key advantages for our system.

The Voronoi domain is the most finely grained measurement of density possible, and is sensitive to details lost in other approaches. Since a local density can be assigned to individual cells, it also allows density to be parsed in ways (i.e. the tiers used below) that are not available using estimators such as kernel density.

A second advantage deals with the fact that astrocytes are large extended objects exposed to many influences, so that the distance from their soma to the plaque edge may not accurately capture their degree of amyloid-beta exposure. In a correlation function approach, this creates an ambiguity in the identification of the proper distance to

describe interaction. Voronoi tessellation defines neighbors, allowing us to measure domain size as a function of the topological distance between an astrocyte and a plaque. The topological distance is defined as the smallest number of domains you must travel through to reach the astrocyte starting from the plaques. Astrocytes are thus arranged into several concentric tiers (as observed in GFAP staining). We expect that tiers may form more homogenous groups than astrocytes divided into distance bins. Individual tiers can be analyzed for plaque-size effects. Tiers are defined as follows (see Fig. 3A-C):

1. The first tier consists of astrocytes with domains that contact the surface of the plaque.
2. The second tier contains neighbors of the first tier not already in the first tier.
3. The third tier consists of neighbors of second-tier astrocytes that are not already in the first or second tiers.
4. Remaining domains are used as control.

This tiered approach is especially advantageous if the effect of a plaque on an astrocyte is “buffered” or shielded by the presence of other astrocytes, or if the plaque has a complicated effect on surrounding structure, for example repelling the closest astrocytes because of its toxic halo, while attracting astrocytes at ensuing shells. Amyloid-beta concentration will be a function of topological distance if each astrocyte can absorb up to a finite amount of amyloid beta. The change in concentration across a biological (process defined) astrocyte domain of size L centered at a distance d from the plaque will be approximately $\Delta C = \max[(1-(r-L)^2/(r+L)^2) + \Delta C_A, C]$, where ΔC_A is the reduction due to absorbance. If ΔC_A is large compared to $1-(r-L)^2/(r+L)^2$, ΔC can be approximated by topological distance, as long as Voronoi domains are close to biological domains. It has been shown that Voronoi domains are identical to the domains generated in a system where processes grow at a uniform rate from a set of seed points until they collide with

the processes of a neighbor and stop growing [Pineda, et al.]. This is similar to the growth of crystalline domains, and is termed a Poisson-Voronoi nucleation process. The typical linear size L_C of the Voronoi domain (Table 4.1) closely matches the radii of process-defined domains measured by Wilhelmsson et al.

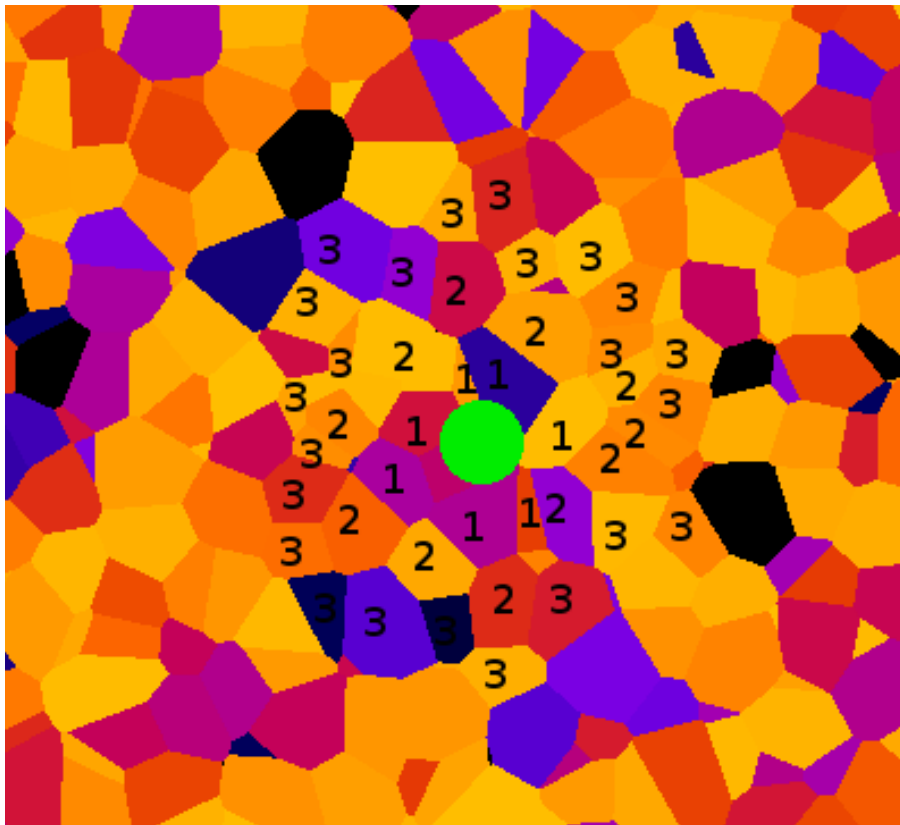


Figure 4.15. Single plane of stack showing Voronoi domains of simulated astrocyte seeds (multicolored polygons) around a plaque (green circle). Domains in tiers 1-3 around the plaque are numbered. Colors are for visual discrimination only, they do not reflect properties.

The Voronoi domains and geometric neighbors of astrocytes in the APP/PS1 and wild-type mice were computed as described in Chapter 3.3. Domain sizes of astrocytes in the first three tiers around plaques in APP/PS1 mice were then compared with more distant astrocytes, which are at least four tiers away from any plaque. Astrocytes in the fourth and greater tiers should be approximately $3-4 \times L_c$ from any plaque, a distance of 75 – 100 μm , where the effect of plaques should be negligible [Koffie et al.]. Mean domain size was largest for domains bordering the plaque, and decreased in each successive shell (Figure 4.17, and Tables 4.1 and 4.2). Linear domain sizes in the first, second and third tiers were enlarged by an average of 4, 2.5 and 1 μm , respectively, in comparison to the domains of more distant astrocytes. These results indicate that plaques push astrocytes away, and that the effect, is sensed by at least three shells of astrocytes, with interaction strength diminishing at each tier.

Shells	Means \pm CI*
1 st shell	28.04 \pm 0.50
2 nd shell	26.58 \pm 0.17
3 rd shell	24.93 \pm 0.10
Control	24.06 \pm 0.15

Table 4.1 Means of linear domain size in each tier over all APP/PS1 mice. One half width of 95% confidence region calculated through bootstrapping given as uncertainty.

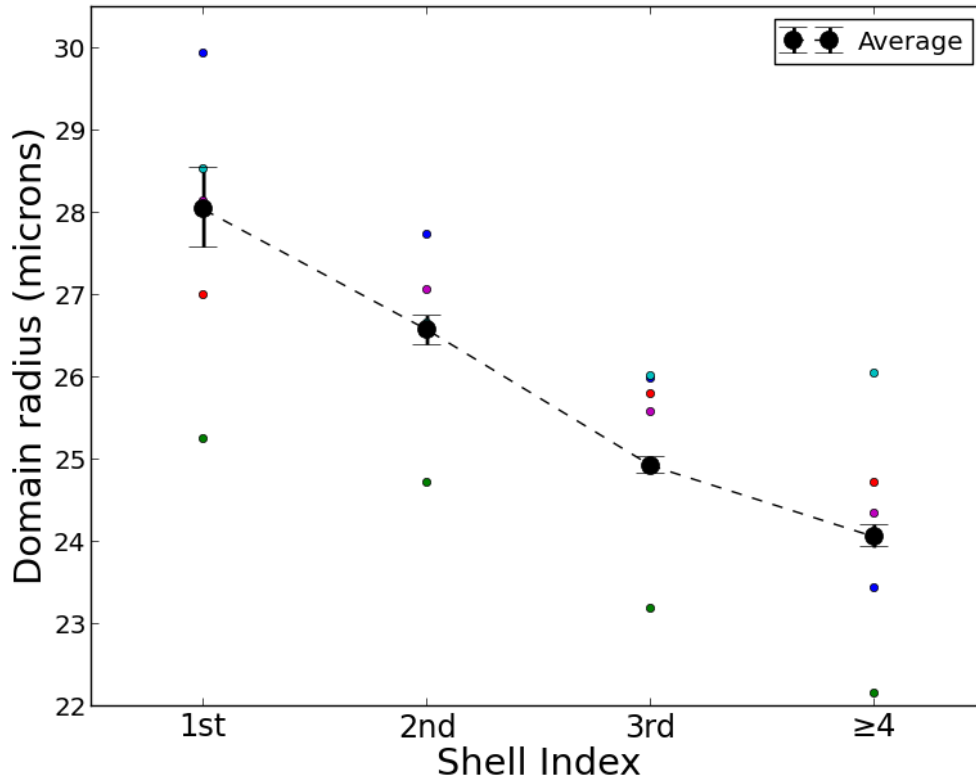


Figure 4.17. Mean linear size of domains in each tier. Colored dots show means for each animal (one animal excluded for insufficient statistics, less than 10 plaques with first shell astrocytes). Black points show mean over all animals, error bars are 95% confidence interval, as calculated through bootstrapping.

Shell	1 st	2 nd	3 rd
2 nd	8.5		
3 rd	18.8	23.6	
Control	23.6	32.9	14.5

Table 4.2 Domain size distributions were compared using Welch's t-Statistic to determine if the mean linear domain size was significantly different from tier to tier. Table gives Welch's t-statistic for the hypothesis that the tier listed in the column is greater than that of a given row. This test confirms that domain size decreases significantly at each tier.

This data indicates that an interaction between astrocytes and plaques exists, but its effect on the spatial distribution of astrocytes is repulsive: precisely the opposite of what was commonly assumed. The surprising nature of this result leads us to parse it more carefully, and model the system to confirm that a repulsive interaction leads to the observed domain reorganization.

One potential explanation for the conflict with prior studies is a dependence of the character of the interaction between astrocytes and plaques on plaque size. Older studies may have only observed a subset of plaques that caused an attractive interaction. To explore this possibility, we plotted domain size of first tier astrocytes as a function of the size of the plaque they are adjacent to. In the case of domains adjacent to multiple plaques, domains were associated with the largest adjacent plaque. We observed a small increase in the magnitude of the shift away from plaques at larger sizes, but the domains of astrocytes adjacent to plaques of all sizes were enlarged in comparison to those of more distant astrocytes. This result is shown in Figure 4.18.

Finally, it is also possible that a subpopulation of greatly enlarged domains drives the increase in the mean, while most domains are unaffected, or possibly even reduced. Domain size distributions are shown in Figure 4.19. Domain size distributions are well approximated as gamma distributions, which are well-known as the limit of the

distribution of domain sizes for the Voronoi tessellation of a Poisson point process.

Pineda, et al. showed that a three-parameter gamma distribution also models the sizes of domains with finite radius hard-sphere seeds. This indicates that the interaction affects all adjacent domains, and neither cell death nor limited enlargement of a subset of domains cause the observed change in the mean.

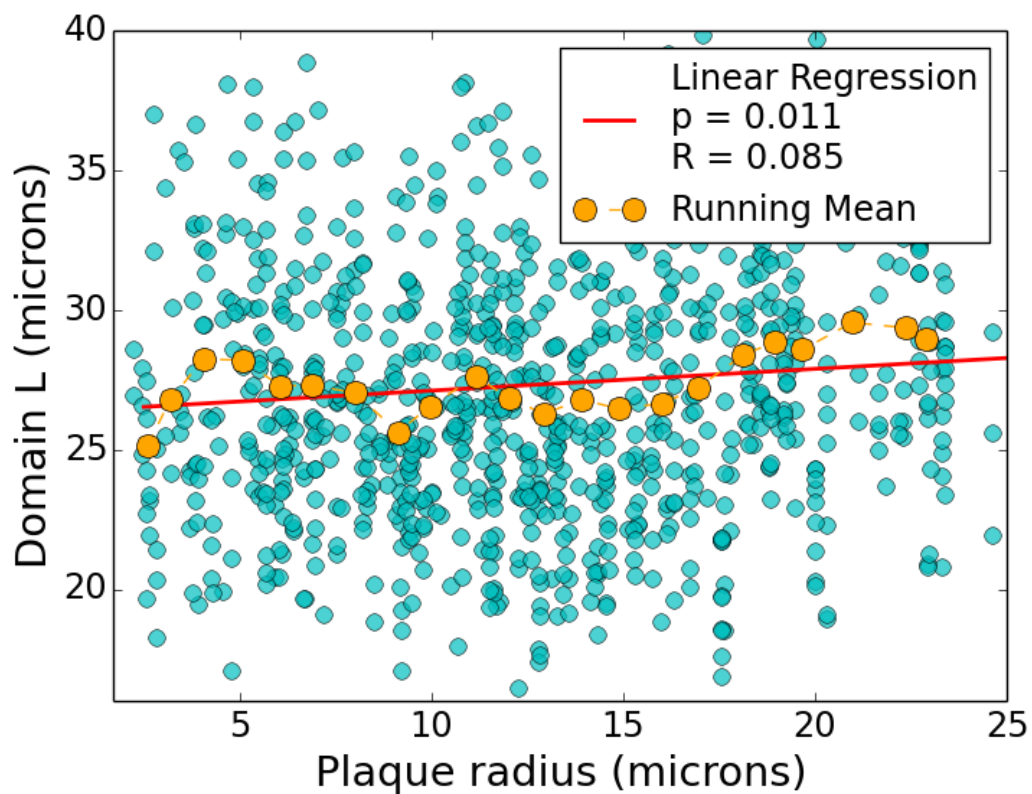


Figure 4.18. Domain size vs. Plaque size. Each aqua dot represents a single first shell domain, with its linear size on the Y-axis, and the radius of the adjacent plaque on the X-axis. Orange circles and dotted line show a running average, with window size ± 2 microns, red line is a linear fit. Domain size is weakly dependent on plaque size and increasing, with no evidence of an inverted interaction at any plaque size in this sample.

First shell domain size at all plaque radii was greater than that of control domains, although domains associated with very small plaques do approach control.

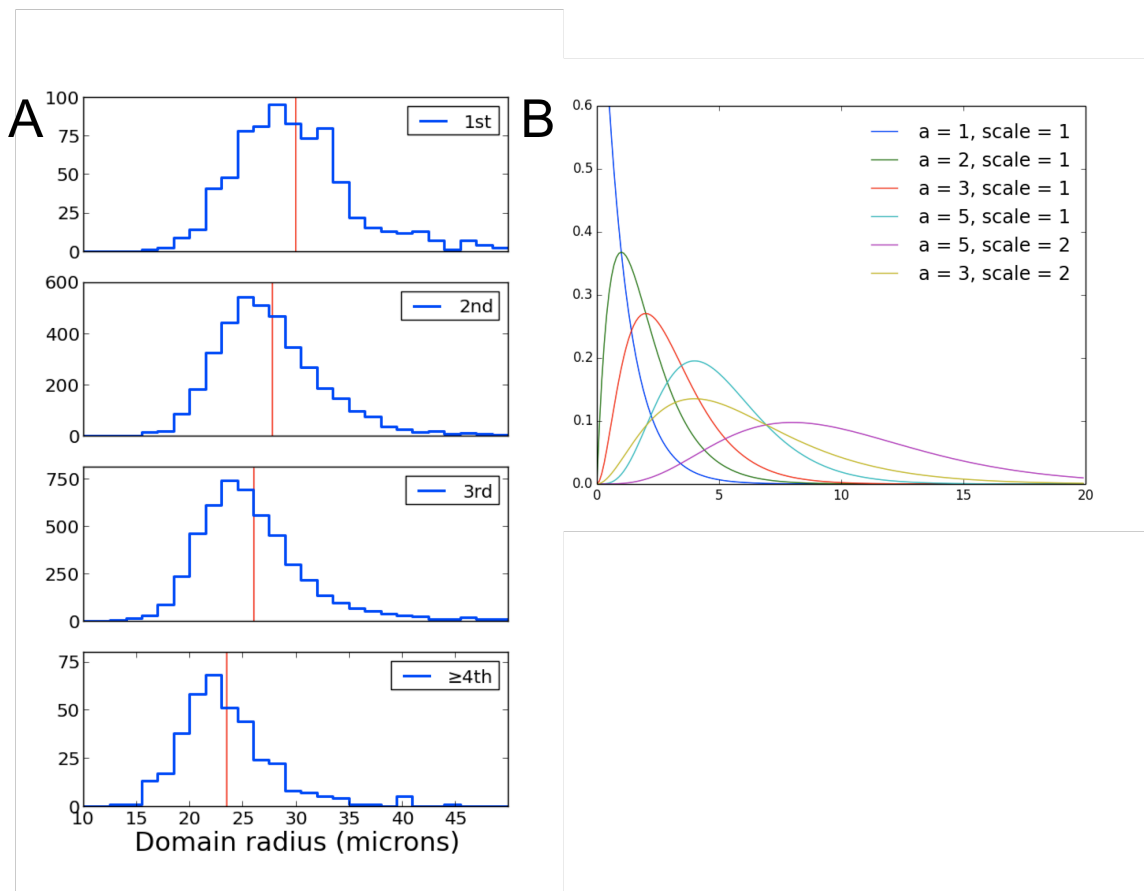


Figure 4.19. Domain size distributions. (A) Domain sizes for the 1st through control tiers, top to bottom. Red line indicates mean of each distribution. (B) Gamma distribution shown with different scale and location parameters. Domain distributions show the typical positive skew of a gamma distribution.

4.6 Simulation of Astrocyte-Plaque Interactions

Simulations were used to help interpret the effects of attractive, repulsive and contact interactions on domain size distributions and $g(r)$, and investigate how astrocyte topology would be affected in the presence of higher plaque loads in the upper limit of what could be found in humans with age. Astrocytes were compared with a model of polydisperse hard spheres, with mean diameter of λ_0 , and density matched to the value of a typical section from an APP/PS1 mouse, to investigate the cause of the enhancement region of $g(r)$. A fluid of hard spheres with long range interactions with a fixed set of spheres representing plaques was then used to investigate potential structural changes at higher plaque loads.

Plaque volumes followed an approximately exponential distribution with a 3000 μm^3 decay length, corresponding to a mean radius of about 9.5 μm and a mean volume of 3500 μm^3 . This matched the size distribution recovered by our image analysis. Hard spheres representing plaques with sizes randomly selected from this exponential distribution were added to the simulation space until their volume fraction reaches 0.059%, which was the plaque volume fraction of a test subject with density in the middle of our APP/PS1 cohort. Total simulation volume was 1.3 mm^3 , and contained 84 plaques and 39,000 astrocytes.

To simulate scenarios in which astrocytes were attracted toward or repelled from the plaque, the hard-sphere astrocytes were treated as thermalized particles in a $1/r^2$ potential. This potential was chosen to simulate a potential proportional to the concentration of some chemical emitted by the plaque. Lastly, we found that simulations exhibited the monotonic relationship between domain size and shell index we observed

in our measurements only if the $1/r^2$ potential was set to zero outside a finite range of approximately 60-100 μm . This finite range potential is roughly the same size as the toxic zone around plaques previously reported [Koffee et al.]. It may indicate shielding of amyloid toxicity, either by astrocytes, or possibly another agent.

Our first investigation was of the radial correlation function of a set of particles with only hard sphere interactions. We found that hard-spheres with logistically distributed radii produced a radial correlation function with exclusion zone and transition region exactly matching the experimental correlation function. The logistic distribution function was chosen for the radii because its cumulative distribution function is the hyperbolic tangent – the steepness parameter S of the hyperbolic tangent correlation function is precisely the width parameter of the logistic radius distribution:

$$(4.6.1) \quad P_R(r, X_0, S) = \frac{1}{2S} \operatorname{sech}^2\left(\frac{r - X_0}{S}\right)$$

The hard shell interactions failed, however, to reproduce the observed enhancement region. In comparison to experimental data, the enhancement region in simulation decayed much more quickly, approaching no correlation at 35 microns in comparison to approximately 50 microns. This indicates that though astrocytes repel one another at short range, the interaction is attractive at longer range, similar to the familiar Lennard-Jones potential.

Because the attractive part of the astrocyte interaction should not affect spatial structure at high densities, we used a hard sphere model to investigate higher plaque loads. Our primary interest was whether the small repulsive force detected between astrocytes and plaques, enough to cause the nearest astrocytes to move a few microns, would increase packing interactions enough to disturb $g(r)$. While in APP/PS1 mice the

percentage of brain covered by thioflavin or methoxy-labeled plaques can reach 1%, in humans it can range between 0.8-6.0%, with an average of around 3% [Urbanc et al., Perez-Nievas, et al].

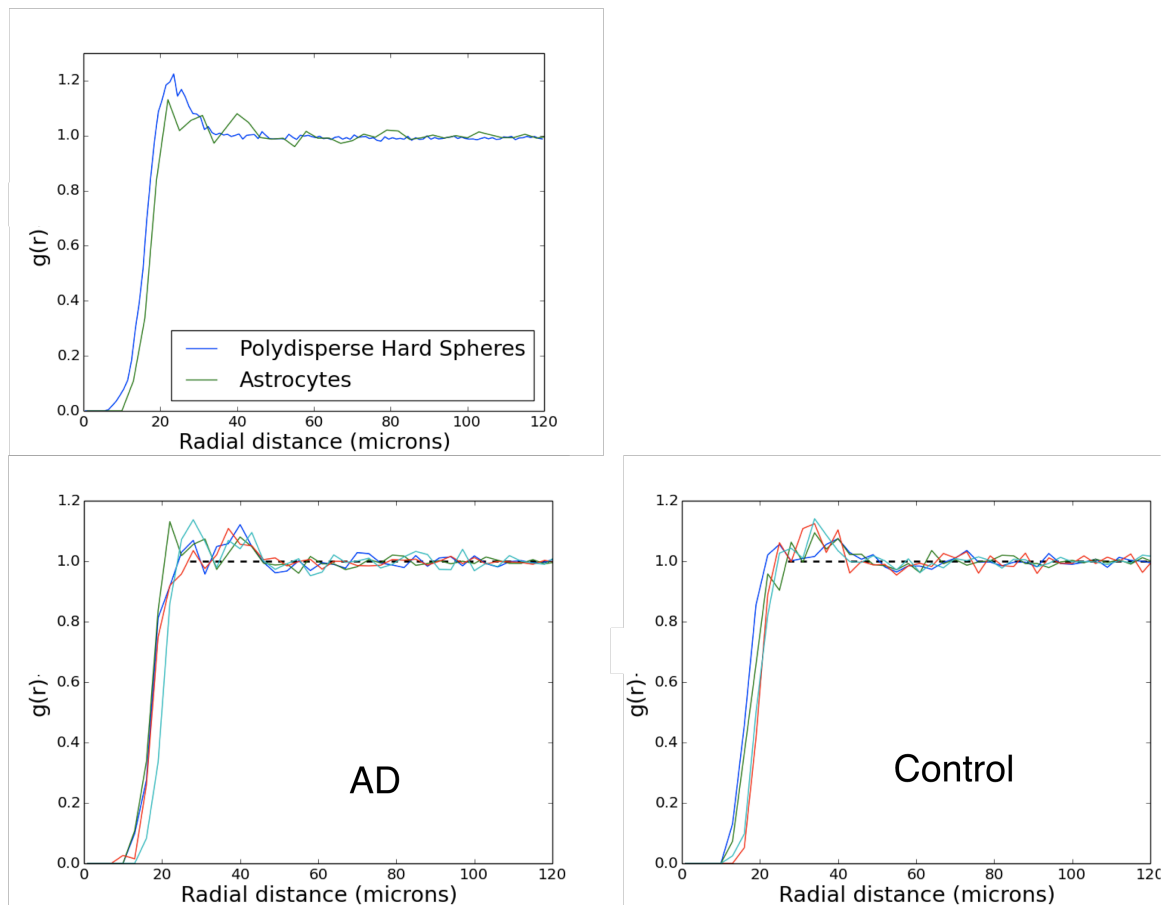


Figure 4.20. Comparison of enhancement zone with model. A hard sphere model shows that an enhancement in $g(r)$ due to packing interactions only decays more quickly than the observed enhancement region. Plots of $g(r)$ are shown for four mice from each cohort – the four remaining mice had high noise and were visually distracting. Each mouse shows evidence of the extended enhancement region.

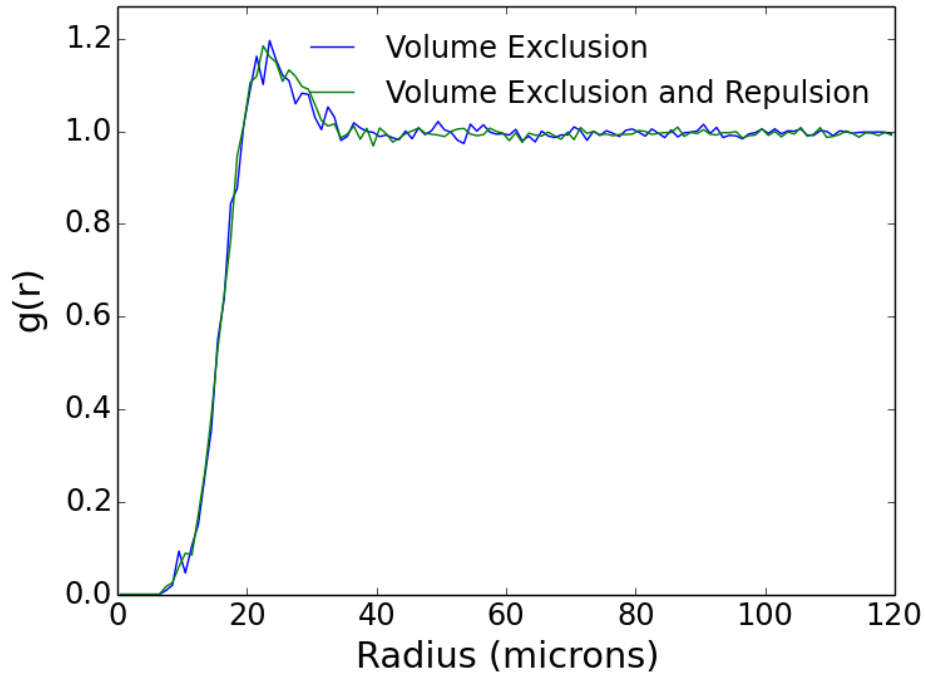


Figure 4.21. Radial correlation of spheres with hard-core interactions only. Green-line shows lack of change when repulsive interaction between astrocytes and plaques with a 0.07% volume fraction is introduced. Enhancement region extends only to about 35 microns, in contrast with the 50 microns observed experimentally.

We first increased the plaque load in our simulations with hard sphere astrocytes to 5%, to establish whether plaque load has any impact using a value in the upper limit observed in humans. We observed that a 5% plaque load has no effect on $g(r)$ if the only action of the plaque is to occupy space (Figure 4.21). If a small repulsive interaction between plaques and hard spheres mimicking the one observed is introduced, a large peak appears in $g(r)$ at X_0 , followed by a small valley, and a smaller, broader peak, before decaying to one (Figure 4.22).

This implies that at high plaque loads, plaque-astrocyte interactions force astrocytes to be more tightly packed, so that the inter-astrocyte interactions become an important factor. Although a “shielding” of the astrocyte-plaque interaction due to amyloid absorbance was not considered in the simulation because of its computational cost, at a 5% plaque load, the system enters a regime with nearly every astrocyte (>99%) directly adjacent to a plaque, i.e. in the “first shell,” making buffering impossible. Thus it is possible that the effect at high plaque load may be even more extreme than the simulation predicts.

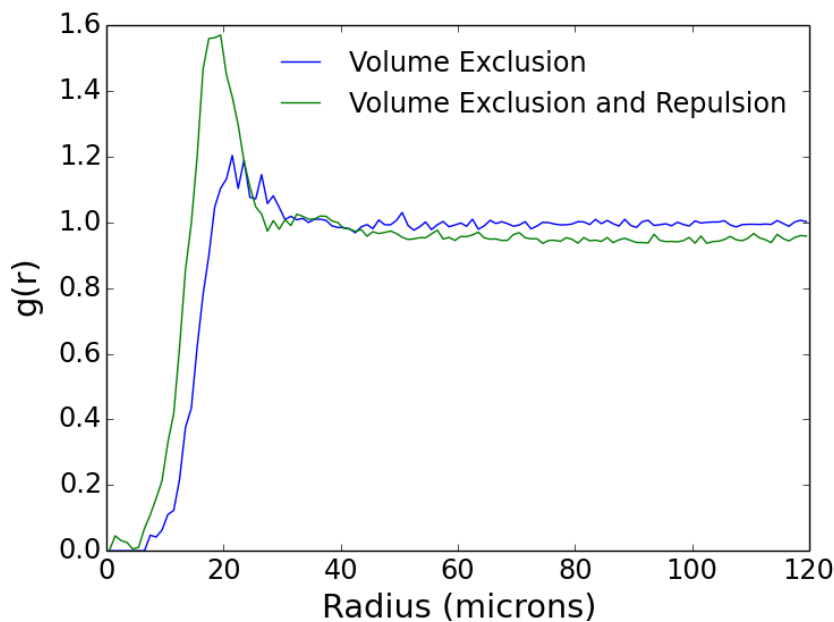


Figure 4.22. Radial correlation of spheres with hard-core interactions only. Green-line shows large change when a repulsive interaction between astrocytes and plaques is introduced with plaques occupying 5% of cortical volume.

We next explored the effect of intermediate plaque loads, taking into consideration two variables, plaque load and plaque size. We found the $g(r)$ was insensitive to plaque load in the ranges we encountered in experiments up to 1% (Figure 4.23A). The most rapid changes occur between 1% and 3%, with the peak shifting to lower values and transition region steepening.

The fraction of astrocytes in the first shell is important for shielding effects, it is also a proxy for the amount of configurations available to the distribution of astrocytes in the cortex. If a high fraction of astrocytes are adjacent to plaques due to energetics, the number of potential configurations are highly constrained. At just less than 1% plaque

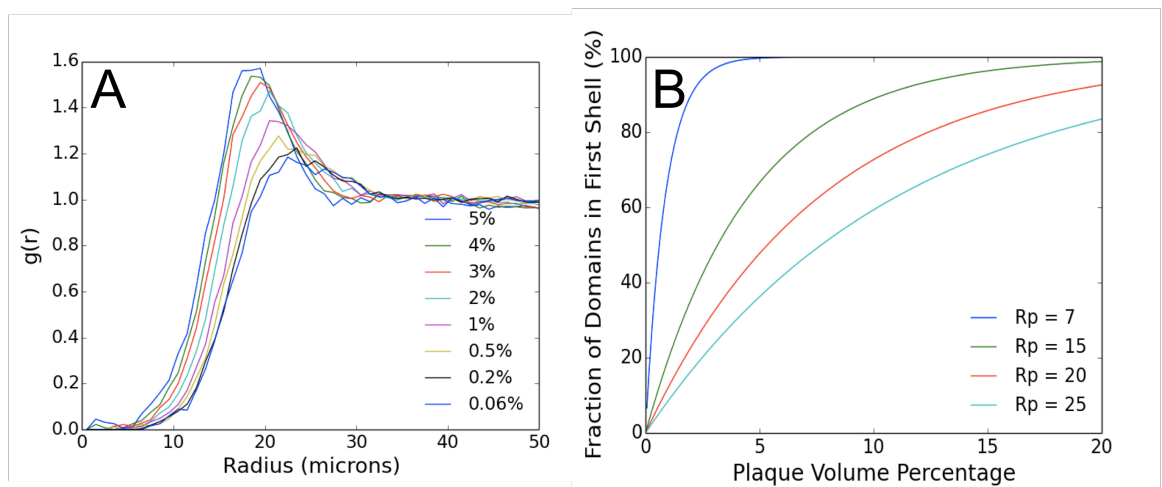


Figure 4.23 Simulation of high plaque loads. (A) The radial correlation function is dependent on plaque load at volume fractions higher than what we observed experimentally. The most rapid change occurs between plaque loads of about 0.5% and 2%, with the enhancement peak increasing in magnitude and shifting left. (B) Decrease in astrocyte configuration possibilities, as indicated by the percentage of astrocytes adjacent to plaques, increases more slowly with plaque load for large plaques than small plaques.

volume, the fraction of first shell domains reaches 50%, and increases to 90% at 3% plaque volume. This corresponds to a significant increase in the amount of astrocytes directly affected by the plaque. The effect is highly dependent on plaque size, as shown in Figure 4.22B. While the fraction of astrocytes in the first shell always increases exponentially with plaque load, the change is inversely related to plaque radius so that small plaques cause a steeper increase, probably because large plaques concentrate more amyloid in one place thereby reducing the surface of contact with astrocytes. At a 3% plaque load the fraction of astrocytes exposed to plaques directly ranges between 30% and over 90% depending on plaque size. In summary, the simulations suggest that higher plaque loads, particularly if small plaques are abundant, forces maintaining astrocyte topology may be compromised.

4.7 Biological Interpretation of Alzheimer's Associated Modifications in Astrocyte Structure and Discussion

The analysis of astrocyte topology in normal and transgenic mouse brains with methods commonly used in physics has produced two main results that may help redefine existing and emerging notions about astrocytes. First, the $g(r)$ function indicates that the defining structural feature of cortical astrocytes is a domain-based arrangement caused by exclusionary forces. Second, after examining the effect of plaques on local structure, we did not find evidence that plaques attract astrocytes. On the contrary, our data suggest that something within the plaque microenvironment pushes the nearest astrocytes away up to 4 μm . This repulsion appears to have a negligible impact on the global astrocyte topology at low or average plaque loads, but it may put a stress on inter-astrocyte interactions at the heaviest plaque loads.

Unlike humans with Alzheimer's disease, APP/PS1 mice do not develop tau pathology or substantial neuronal loss. It is possible that these have additional impacts on astrocyte organization, and change in some way the interaction between astrocytes and amyloid plaques. Even though astrocytes do not express tau protein, they are known to interact with neurons, which do.

A chief advantage of this study is the use of SR101 to label astrocytes instead of resorting to GFAP immunohistochemistry. A prototypical response to brain injury is "reactive astrogliosis," which is typified by cytoskeleton hypertrophy and GFAP up regulation. However, GFAP does not stain "non-reactive" astrocytes prominently, which, if not recognized by the experimentalist, can lead to incorrect interpretations on the general role of astrocytes in disease and injury. Alternative labels to GFAP include SR101, used in this study, and also techniques for the immunodetection of glutamine synthase or glutamate transporters, which label astrocyte arbors [Kulijewicz-Nawrot, et al.], and non-specific body filling-dyes such as Nissl stain, GFP, or Lucifer yellow [Wilhelmsson, U. *et al.*].

This pan-astrocytic stain allows investigation into the basic spatial structure of astrocytes. Neurons in the cortex are known to have non-trivial structure, namely an arrangement into linear columns perpendicular to the cortical surface. Recent studies have proposed that astrocytes may also be components of the cortical column [e.g. Magavi]. It has been shown the correlation functions can identify and quantify cortical columns [Buldyrev, Cruz]. Columns are an anisotropic structure, and better suited to detection using a full vector correlation function rather than the radial function used here. However, a periodic structure of columns would still be expected to show enhancements at multiples of the lattice spacing in the radial correlation function, which

we did not observe. It is possible that columnar spacing is not regular enough to be distinguished above noise, or that cortical curvature is a confounding factor. We do note, however, that the spacing of mouse columns would be expected to be narrower than that of monkeys, which is approximately 25 microns. Astrocytes would need to be almost perfectly centered on columns of this spacing in order to agree with the observed exclusion zones. This would produce a very regular arrangement, almost surely observable in the correlation function.

The observed correlation function presents some interesting relationships with known astrocyte cellular structure and biology. We found that astrocytes in the adult brain exclude one another below distances of 18 mm, and are more likely than simple hard-spheres or random particles to have neighbors in the enhancement region of 20-50 mm. Enhancement region separations are compatible with the range of diameters (36.8-50.9 mm) of the extent of astrocyte processes labeled with Lucifer yellow.

[Wilhelmsson,U. *et al*]

The minimum exclusion zone, on the other hand, has no obvious biological correlate, either to a component of the astrocyte, or a known interaction between astrocytes, which raises the question of its meaning. In light of this, we recognize that the Voronoi domain size distribution closely matches the result of a model of crystal growth proposed by Pineda, et al., in which crystalline domains grow at a constant rate from finite sized seeds, until colliding with the growing domain of another seed. In this analogy, astrocytic processes replace crystalline domains, and the finite size of the seeds is due to an inter-astrocyte force that is present during development, when astrocytes establish their position. This force might serve to optimize the size of the astrocyte arbor. It is likely that the signaling mechanism that underlies the interaction is still active in adult astrocytes, since astrocytes in APP/PS1 mice undergo some rearrangement when

interacting with the plaques, and their correlation function remains the same as that of the wild type.

This can be expressed as a developmental principle: body sizes (including soma and processes) do not determine astrocyte topology but, rather, collisions and interactions during development forces determine body size. Neurons and their axons determine one another's positioning through chemicals known as semaphorins and ephrins. It is tempting to speculate that similar chemical cues emanates from astrocytes, maintaining proper spacing. Further, local interactions with neurons, blood vessels, and other glia might contribute to the variability in astrocyte sizes, thereby shaping final astrocyte topology. Overall, there is little understanding, and a theoretical framework is lacking, of the origin and maintenance of the astrocyte domain-based organization, and its contribution to information processing in cortex.

In summary, the accumulation of amyloid- β plaques in 5-9 month-old APP/PS1 mice did not perturb the domain-based astrocyte topology although, locally, plaques had a repulsive effect on surrounding astrocytes that extended to at least three shells, representing a distance of approximately 80 μm from the plaque edge. This 80 μm is far beyond the boundary of the plaque extracted in our images. However, amyloid- β plaques and their microenvironment contain a complex and heterogeneous collection of amyloid- β species in different structural conformations and densities. MethoxyO₄, used in this study, stains only the fibrillar amyloid- β in the compact plaque core, but not the toxic halo of soluble oligomeric amyloid- β surrounding the core. [Koffie, et al.] The average astrocyte (cell body + processes) is over 10 times larger than an average plaque core (filling a volume of 43400 versus 3500 μm^3), making it highly improbable that a plaque kills several astrocytes at once, as it does neurons. [Urbanc et al.] The halo, however, is highly toxic, producing high levels of synapse loss within 6 μm from the

plaque edge, and lower levels up 50 μm away. High levels of synapse loss are consistent with regions where soluble oligomeric amyloid-beta is detected immunohistochemically. [Koffie et al.] Our finding that plaques had a decreasing impact over three shells of astrocytes, mirroring spine loss, can be interpreted in support of a model where a decreasing gradient of soluble oligomeric amyloid-beta is toxic to astrocytes, causing the nearest of them to attempt to distance themselves from the plaques. It is worth noting that the detection of domain expansion in the second and third tiers rules out a scenario in which, in the first tier, migration of astrocytes to the plaques has been masked by astrocyte exclusion from the zone of highest halo toxicity.

Our findings thus contradict the widespread belief that plaques and/or their microenvironment act as a chemo-attractant for reactive astrocytes, which, as part of adaptive defense response, go to plaques, phagocytose fibrillar amyloid-beta and seal plaque-induced injury with a scar, thereby reducing the growth of plaques and their overall impact. This idea is mostly based on evidence from astrocytes transplanted *ex vivo* into brain slices, which have very different properties than normal astrocytes, and deletion of genes for GFAP and vimentin in transgenic mice, which interferes with astrocytic cellular mobility, but also likely interferes with a range of other astrocytic functions.

Overall, our study changes the view of how astrocytes interact with plaques in favor of a model where astrocytes are passively engaged, if not directly deranged, by plaques and their microenvironment. Should astrocytes limit plaque growth, they do so indirectly by clearing soluble oligomeric amyloid-b, [Verghese, P.B. et al.] or recruiting microglia through the release of soluble chemokines. [El, et al.] Time-lapse microscopy has already provided unequivocal proof that microglia migrate to plaques. [Meyer-Luehmann, et al]

Our findings are consistent with the observations of previous analyses of the interaction of microglia, astrocytes and plaques in *human* brains. [Serrano-Pozo et al., a and b] These results showed astrocyte numbers detected with glutamine synthase immunohistochemistry were not greatly altered in Alzheimer's disease, while GFAP immunostaining showed the expected intense clustering around plaques. The density of microglia around plaques, but not that of GFAP-positive astrocytes, correlated with plaque size, suggesting that amyloid-beta attracts microglia, but not astrocytes. Here we extend those observations to directly examine plaques and astrocytes in their vicinity in an experimental model, using 2-photon microscopy and 3D reconstructions from living mice, and conclude that plaques do not attract astrocytes, supporting recent observations suggesting that astrocytes do not move after development to sites of injury.

In summary, our study leads to two main conclusions. One, repulsive, and possibly attractive chemoactive agents are essential for the maintenance of astrocyte spacing even in face of disease. Two, major changes in astrocytes in the vicinity of amyloid-beta plaques are confined to phenotypic alterations including strained inter-astrocyte interactions, increased production of GFAP and development of a "reactive" appearance rather than proliferation or migration towards plaques. Finally, the functional alterations associated with these phenomena remain an outstanding question.

5 Structural Motifs of Long-Range Axons

The brain is compartmentalized into subunits that perform specific functional tasks. In the human brain, for example, there are at least five distinct regions involved in visual processing, performing tasks such as pattern recognition, assembly of contours into shapes and objects, and motion perception. Many neurons are devoted to the local circuitry involved in these processing tasks, and have axons that stay within their region. However, a subset of neurons is devoted to broadcasting the results of this processing to other areas. The axons of these neurons can extend up to several centimeters, as compared to the sub-millimeter range of other axons, and together with supportive glial cells, make up the interior portion of the brain known as the white matter.

These long-range connections play a crucial part in the proper functioning up the brain. A basic result from network science is that the addition of a few long-range connections changes the character of a network from a “large world” to a “small world,” with only a small number of links between any two nodes. [Watts and Strogatz] The particular importance of these long-range connections to intelligence is shown by the increasing ratio of white matter to gray matter in the brain throughout evolution, especially in the prefrontal region responsible for executive tasks (see Figure 5.1) [Schoenemann et al.].

Establishing these long-range connections is a non-trivial problem at the cellular scale. Since connectivity patterns between areas are generally conserved among members of a species, there must be some system of guiding axons between areas. Although it has long been recognized that axonal growth responds to chemical cues,

[Huber et al.] the manner in which local directional signals are integrated into a long-range trajectory remains unknown to neuroscience.

We expect that whatever strategy is used for long-range guidance, it will leave clues in the geometry of axons. For example, what are the similarities, and what are the differences, between two axons both extending from neurons in area A to targets in area B? How are they different from feedback axons going instead from B to A? Where do a

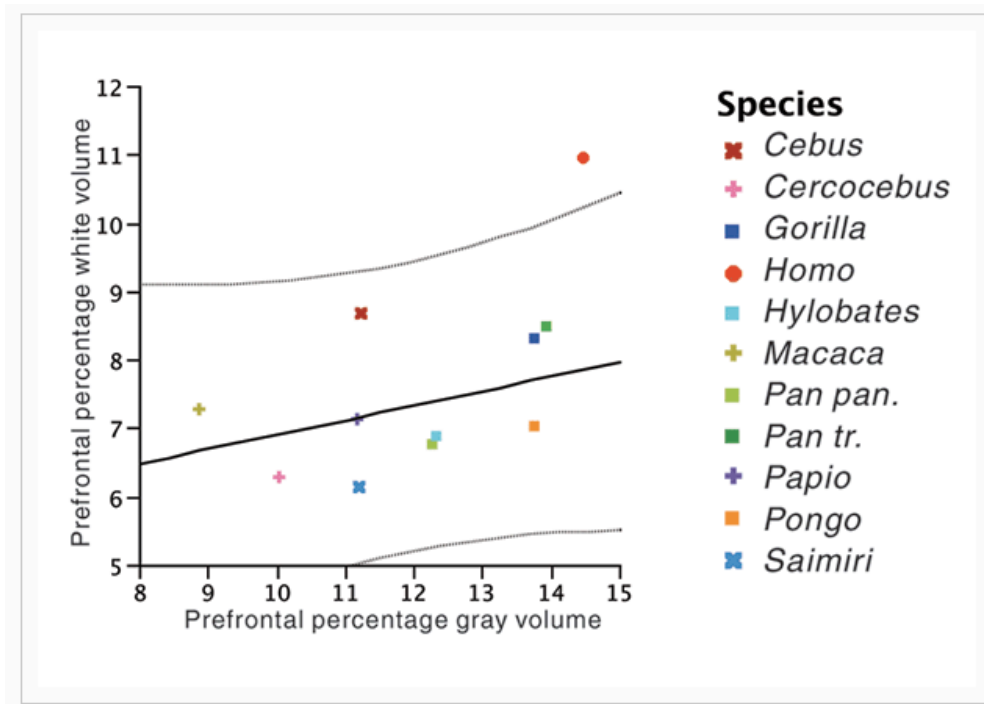


Figure 5.1 From Schoenemann et al. The ratio of prefrontal white matter to prefrontal grey matter is much higher in humans than non-human primates. Units are percentage of total brain volume. The solid line represents least-squares regression based on nonhuman species average values (prefrontal percentage white volume = $4.794 + 0.212$ (prefrontal percentage gray volume)) and the dotted lines represent the 95% confidence intervals.

pair of axons with the same origin, but different targets, diverge?

These types of questions were beyond the limits of experimental neuroscience for most of its history. Recent advances, especially in the fields of 3D microscopy and tissue preparation (e.g. the CLARITY method [Chung et al.]), have made asking these questions feasible for the first time.

A clue to a possible structural motif governing the guidance of axons was discovered by Wedeen, et al. in 2012. This result used a technique called Diffusion Spectrum Imaging, (DSI) a type of high-angular resolution diffusion MRI (dMRI), which images the diffusion propagator of water. Since water in the white matter is confined within the fatty myelin sheaths of axons, its diffusion propagator gives information on the orientation distribution of axons within a dMRI voxel. Wedeen, et al. found that even at high angular resolution, the diffusion propagator in any given voxel had at most three lobes. Furthermore, in voxels with three lobes, the vectors describing the lobes always spanned three-dimensional space – three lobes in a single plane were never observed. In most regions of the brain, in fact, the vectors to the maximum of each lobe were close to mutually perpendicular. Axonal tracts can be reconstructed from dMRI data by connecting the vectors of adjacent voxels into streamlines. The tracts uncovered by DSI were arranged in non-intersecting sheets, a very unique structure almost impossible to create by chance [Wedeen, et al. 2012b]. This white matter structural arrangement was coined “the Grid” by its discoverers.

The smallest dMRI voxels are about $(0.5 \text{ mm})^3$, while axons average about 10 microns in diameter. Furthermore, the diffusion distance of a water molecule during an MRI pulse sequence is only a few tens of microns. Even the most technologically advanced dMRI then, can only report the average behavior of the thousands of axons

contained within a voxel, and the grid, at this point, was a mesoscale phenomena, describing neither long-range trajectories or single-axon behavior, but the average local behavior of several hundred axons.

Our goal in this analysis is twofold: one, to investigate the scale at which the grid constrains individual axons, and two, to formulate a hypothesis on the constraints that the grid puts on the long range trajectories of axons, and understand how long range trajectories are related to events at the microscopic level. The question of how the different scales in a system interact with one another is a common one in statistical physics. We will find that the mesoscale grid description also applies to single axons, and that there is a deep connection between behavior at the microscale and long-range trajectories.

5.1 Experimental Design.

At a basic level, our experiment consisted of comparing descriptions of the geometry of the brain's white matter at two scales: the millimeter scale, using dMRI imaging, and the micron scale, just above the average diameter of an axon, using histology and high resolution microscopy. We chose to examine axons in the white matter below the motor cortex. Most axons in this region are part of the corticospinal tract, a prototypical long-range pathway projecting from the cortex towards structures in the mid and forebrain. Other populations of axons in this region connect the motor cortex with other cortical areas, or simply pass through the area without making a connection. Our experimental program was as follows:

1. Confirm millimeter-scale grid structure in motor area of our experimental subjects using dMRI imaging.

2. Describe distribution of axon orientations at scale of tens of microns. Relate properties to millimeter-scale grid.
3. Attempt to identify notable subpopulations with alternative structural motifs.
4. Identify modalities of long-range navigation in the grid, such as turning and branching between grid axes.

Step one in this program was performed by Dr. Van Wedeen, using the methodologies from Wedeen, et al. 2012. They will be briefly described in the upcoming section. The primary challenges for steps two and three were constructing an unbiased sample of axon orientations, and extracting single axon orientation information from the microscopy. Sampling is important, since a major part of the grid hypothesis is that a region should contain at most three primary orientations. A small sample may not contain sufficient statistical power to distinguish multiple orientations. Our approach to creating an unbiased sample was to image a large continuous area. The continuity of the sample allows for an easy estimation of the effect of brain curvature on the orientation distribution, and avoids selection bias.

The fourth step arises from the constraints the grid places on axon trajectories. An axon restricted to the grid can only target neurons directly in front of it, unless it can switch between the different orientations – a path composed of 10 steps North, 4 East, then two more North, for example. Non-trivial connectivity in a gridded brain requires that axons branch, or execute turns. The length scale of the grid imposes a maximum size on these turns. If, roughly speaking, it is unlikely to find a section of an axon of length greater than L not oriented with one of the grid directions, then the turning radius must be less than $(2/\pi)L$. Turns are necessary for the grid to be a global

organizational principle of the brain, and are an important, testable prediction of the grid.

5.2 Experimental Methods – Animals, Tissue Preparation and Imaging

The animal care, tissue preparation, and tissue microscopy for this experiment were performed by our collaborators at Boston University Medical School, doctors Douglas Rosene, Farzad Mortazavi, and Adrian Oblak. Diffusion MRI imaging was performed by Dr. Van Wedeen of the MArtinos Center at Massachusetts General Hospital. A brief description of their efforts is given in this section.

Subjects:

Three young, adult male rhesus monkeys were used in these experiments. All were obtained from national primate centers or domestic breeders and had known birthdates and health records, which were screened to ensure they were free from disease or experimentation that might compromise the brain. All were part of other ongoing studies and were housed at the Laboratory Animal Science Center on the Boston University Medical Campus (BUMC), which is managed by a licensed veterinarian and fully accredited by the Association for the Assessment and Accreditation of the Laboratory Animal Care. All procedures conformed to the National Institutes of Health guidelines and the Institute of Laboratory Animal Resources Commission on Life Sciences' *Guide for the care and use of laboratory animals* and were approved by the BUMC Institutional Animal Care and Use Committee.

Surgical Procedure and Tracer Injections

Animals were first sedated then anesthetized, while heart rate, respiration, oxygenation and muscle tonus are monitored to ensure a safe surgical level of anesthesia. The head was stabilized, and a midline incision made. A bone flap was removed in one piece and the dura incised to expose the precentral gyrus. Three to five injections of biotinylated dextran amine (BDA) were placed into the hand representation of primary motor cortex, 1.5 mm deep. Once all injections were completed, the dura was closed, the bone flap sutured back in place and the muscle, fascia and skin closed in layers.

Perfusion Procedure and Tissue Harvest

Post-operative survival times ranged from 21 to 36 days after which monkeys were deeply anesthetized and euthanized. Following perfusion with paraformaldehyde, the brain was removed from the skull, weighed, photographed and then post-fixed overnight.

Tissue Processing Procedures

Following MRI scanning (see chapter 5.3), the brain was blocked in the coronal stereotactic plane, photographed and then cryoprotected for 5 total days. Each block was then flash frozen and stored at -80°C until cut in the coronal plane on a sliding microtome into series of sections of 30 μm thickness, spaced at 300 micron intervals. All cut sections stored at -80°C until further processed immunohistochemically (e.g., *Giannaris and Rosene*).

Visualization of Tract Tracers

To visualize the motor cortex projection fibers labeled with BDA, one series of 30 μm thick sections were thawed at room temperature, rinsed remove glycerol, and processed

free-floating. After rinses with contrast agents designed to conjugate with the BDA, mounted on gelatin-coated slides, dried and coverslipped.

Immunohistochemistry for SMI-312 and SMI-32

Series of 30 μm sections adjacent to the BDA series were thawed and rinsed to remove the glycerol. They were then immunohistochemically processed through a blocking solution, irradiated, and then incubated in primary antibody solution of mouse monoclonal SMI-312 antibody or SMI-32 antibody, and irradiated again. Sections were then kept for an additional 36 hours in the primary antibody solution.

Sections were rinsed, then incubated in with fluorescent labels selected to conjugate with the SMI antibodies. Sections were kept in solution overnight, after which they were rinsed, then mounted on gelatin-coated slides and cover-slipped.

Microscopy

Immunostained fibers were visualized using a Zeiss LSM710 laser scanning confocal microscope. Stacks of images were acquired at a z-step of 1.0 μm and reconstructed using ImageJ (version 1.47b).

dMRI Imaging

The existence of the previously observed grid structure in the white matter below the motor cortex was confirmed using the previously described Diffusion Spectrum Imaging methods [Wedeen 2012a]. To summarize the methods:

After 24 hours of fixation the brain was transferred to an MRI scanning solution of perfluorocarbon and Diffusion Spectrum MRI (DSI) was acquired at 9.4 Tesla (Biospec 20 cm, Bruker Corp., Billerica MA) as previously described. [Wedeen, et al., 2005] The

acquisition pulse sequence was a spin echo TR/TE 1000/40 ms with hybrid echo-planar 3D Fourier transform spatial encoding with isotropic resolution of 400 μm – 500 μm depending on brain size. A 3D volume image of the brain for each of 515 diffusion-encoding q-vectors, with maximum sensitivity $b_{\text{max}} = 40 \text{ ms } \mu\text{m}^2$, with spin-echo diffusion-encoding gradient pulse pair with peak intensity $G_{\text{max}} = 440 \text{ mT m}^{-1}$, inter-pulse delay $\Delta = 24 \text{ ms}$ pulse durations $d = 13 \text{ ms}$. Using 4 averages, total scan times were 24-32 hrs. Orientation density functions were reconstructed, orientation maxima identified, and paths computed with streamline tractography and visualized using MGH Diffusion Toolkit and TrackVis software. [Wedeen, et al. 2008]

5.3 Experimental Methods – Image Analysis

Image analysis was performed through a combination of correlation-based measurements to measure fiber orientation distributions, and manual identification and measurement of turning and branching events.

Correlative Orientation Analysis

The application of correlation functions to fibers requires a statement of what is being correlated. One might expect an analysis to begin with an extraction of fibers from an image, followed by measurement of properties of each fiber individually. We resort to a correlation function description because of the difficulty in extracting individual fibers, see Figure 5.2 for examples. Thus what we are actually correlating is the distribution of some contrast agent in the image.

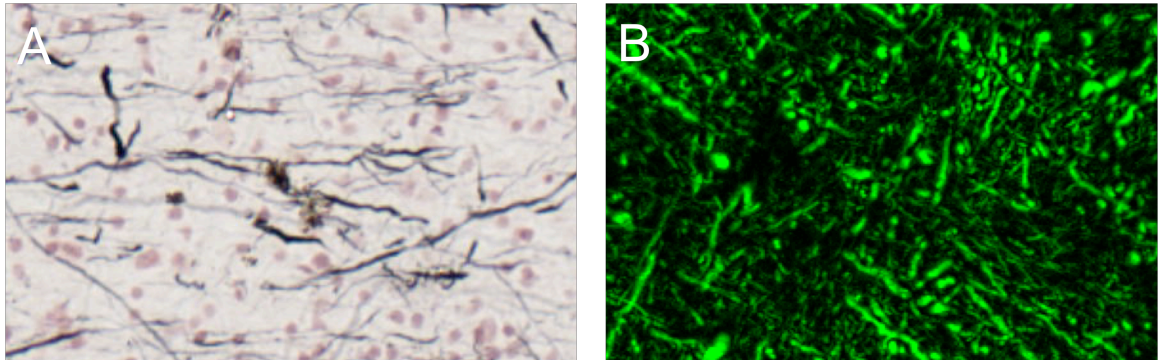


Figure 5.2. Illustration of difficulty of extracting individual fibers. (A) An example of BDA stain, light microscopy. **(B)** An example of SMI-312 fluorescent confocal microscopy. Fibers cross one another many times in both images. Each intersection create an ambiguity. An algorithm may be able to detangle dense fields, but the mathematics may be difficult to understand, unlike our correlative methods.

Correlating the contrast agent is equivalent to the correlation of a sample of points in the volume of an object, as discussed in Chapter 3.3. Correlation functions are estimates of the joint probability of observing events at two spatially separated points. In this particular case, the “event” is a positive outcome for a test of whether or not that point is inside an axon.

One might first consider measuring orientation with the two-point correlation function (see Chapter 3 for background). Consider an image containing axons which have one or more preferred orientations. Given one point x in the image that tests positive for being inside an axonal fiber, it is more likely that another point, y , will test positive if the vector $y-x$ is aligned with one of the preferred directions. Thus anisotropy in the two-point correlation is related to anisotropy in fiber orientations. Our goal, however, is to measure what fraction of axonal trajectories are oriented along some particular direction. (i.e. in a sample of 3 linear millimeters of axonal fibers, 1.5 mm

worth of fibers are at angle θ). Unfortunately, the two-point correlation function will respond to *all* correlations, for example non-uniform density or the clustering demonstrated in Figure 5.2. This makes it unsuitable for our task of describing the orientation distribution of single fibers.

These inter-fiber correlations are strong in the white matter. For example, Figure 5.3 demonstrates anisotropic bundles of multiple axons. The width of a peak in the two-point correlation function will reflect both the distribution of single fiber orientations, and the width of these bundles. The two-point correlation function is also unable to separate the signal of randomly oriented fibers and correlations in image density. These

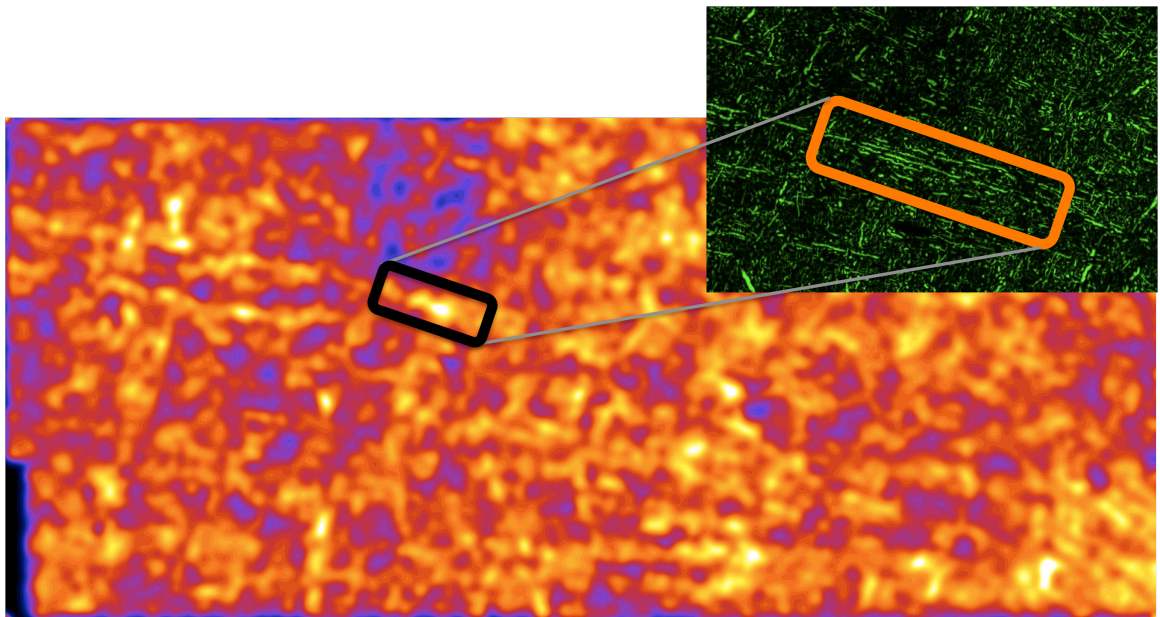


Figure 5.3 A field of SMI-312 stained axons was smoothed by convolution with a Gaussian kernel, with a sigma about 5 times the diameter of a large fiber. A heat map of the density still shows noticeable anisotropy. The sub-selection shows that anisotropy at this scale corresponds to bundles of axons.

fibers would expect to create an isotropic correlation background that decays with radius in proportion to the number of fibers with a given length. This is exactly the same signature produced by correlations in image intensity or fiber density. Such correlations could be caused by a gradient in the density of fibers. A fiber density gradient is expected with tracer injections, since fibers disperse as they move away from their source, and is clearly visible in our BDA tracer injection (see Figure 5.8 B and C). Intensity correlations can also be introduced by the experiment, for example fluctuations in laser intensity over the sample during image acquisition, or variation in the absorption of the contrast agent. A two-point correlation function is shown in Figure 5.6A, and exhibits an isotropic background much higher than that estimated from other methods.

To isolate the single fiber orientation distribution, the Path Probability method for calculating the relevant subset of the irreducible three-point correlation was developed. The theory of this method is discussed in Chapter 3. Briefly, the Path Probability (PP) is a method for estimating the subset of the three-point correlation function where displacements from the reference point are collinear, e.g. $c_3(\mathbf{r}, C\mathbf{r})$, where $C < 1$, and the point distribution is dense, or line-like. As discussed in Chapter 3.3, the three-point correlation function isolates the contribution of single extended structures to the correlation, making it better suited for measurements of orientation than the two-point correlation.

The results of the three-point correlation function were confirmed by comparison with the results of the Structure Tensor method, a technique from computer graphics and digital image analysis. [e.g. Knuttson et al.] Recently Budde and Annese [2012] applied it to measure the orientation distribution of fiber pathways in histological

images of both the corpus callosum and cortical grey matter, and our method follows theirs. It calculates the direction of maximal change in intensity in a small region of pixels by finding the eigenvectors of the second moment matrix of the gradient, averaged over the window, with some averaging function $W(r)$ (equation 5.3.1).

$$5.3.1 \text{ (a)} \quad S_W(\mathbf{x}) = \begin{bmatrix} \langle I_x(\mathbf{x}) \rangle_W^2 & \langle I_x(\mathbf{x}) \rangle \langle I_y(\mathbf{x}) \rangle \\ \langle I_x(\mathbf{x}) \rangle \langle I_y(\mathbf{x}) \rangle & \langle I_y(\mathbf{x}) \rangle_W^2 \end{bmatrix}$$

$$(b) \quad \langle I_x(\mathbf{x}) \rangle_W = \int W(\mathbf{r}) I(\mathbf{x} - \mathbf{r}) dV$$

In our present analysis a 7x7 pixel window was used, which translates to a different real size in each image preparation (BDA image: 1 px/ μm , SMI312: 0.83 px/ μm , SMI32: 1.67 px/ μm). If this region contains a fiber, the direction of maximal change will be perpendicular to the fiber's edge. The orientation reported from the ST method is perpendicular to the direction of maximal change, i.e. parallel to the edge. In contrast to AC and PP, the ST is a local method. It is sensitive to sinuosity of the fibers, since it has no mechanism for averaging fluctuations in orientation over distances larger than the window size. For the Structure Tensor to function properly, window size must be small enough to contain a single fiber. A larger window will average gradients due to multiple fibers, outputting eigenvectors that do not correspond to the orientation of any actual fibers. A small window will usually contain only a single fiber, so the distribution can be directly interpreted as the proportion of fibers with a given orientation. The critical parameter window size must be small compared to its inter-fiber distance, so the ST method performs better with low density images. An anisotropy measurement can also be derived from the ST matrix, for example $anisotropy = |e_1 - e_2| / |e_1 + e_2|$, where e_1 and e_2

are the eigenvalues of the matrix. Filtering low anisotropy pixels from the orientation distribution diminishes the effect of multiple fibers appearing in the same window.

Unlike the three-point correlation function, the structure tensor does not contain length information. It did, however, serve as a useful check on the resolution of the three-point correlation function, especially at short ranges where the Path Probability estimate may be expected to include some contributions from two point correlations, in the form of the $E[P_1]E[P_2P_3]$ and $E[P]^3$ terms from line 2-4 of the diagram shown in Figure 3.4. In all cases no orientation peaks were observed in distributions produced by the Structure tensor that were not also present in those produced by the PP method, although PP did resolve peaks not above noise in the other methods.

Turn and Branch Identification and Measurement

Identification of turning and branching axons in 2D microscopy is still best performed by eye. Automated methods cannot overcome the difficulties of discriminating these from crossing fibers. Identification of sharp turns and of branches is of interest, as the existence of these events is necessary for the grid to govern axons along their entire trajectories, due to the limitations restricted orientation places on connectivity. Besides being strong evidence for the validity of the grid at small scales, a high rate of these events places important constraints on current dMRI techniques as a tool for study of connectivity.

To estimate the lower bound of frequency, we first placed a randomly oriented square counting grid ($30.26 \mu\text{m} \times 30.26 \mu\text{m}$) onto a 20x image of BDA stained tissue. We identified turns and branches within every fourth box in every fourth row of the grid according to the following conservative identification criteria:

1. Fibers must be visible in both the unprocessed image and after smoothing with a Gaussian filter with 5-pixel radius to insure fibers have a minimum size and stain intensity.
2. Fibers must clearly have a linear orientation on all sides of the turn or branch.
3. The apex of the turn or branch must occur within the counting box.

Two separate surveys were done, because it was found that an eye accustomed to looking for branches was less effective at identifying turns, and vice versa.

After counting turns and branches in this way, we estimated the total fiber length in the region sampled by the counting grid through direct and indirect methods, which were compared to ensure their reliability. The direct method proceeded by measuring the length of each fiber in each counting box that passed criteria (1) for turn identification. Error in this measurement could be introduced by shifting acceptance thresholds, a phenomenon known as experimental drift.

Total length was estimated indirectly by dividing the total area occupied by fibers in the sampled region by their mean cross-sectional width. Total area was measured by thresholding the Gaussian smoothed image. The threshold used an HSB decomposition of the image to separate the darker fibers from the light background, and remove colored glial cells (e.g. the cells visible in Figure 5.2). To obtain a threshold that reflected selection criteria (1), we lowered the threshold to the point just below where all identified turn were selected as foreground. Applying an image-wide threshold eliminates the complication of experimental drift.

Width was estimated by measuring, in the thresholded image, the edge-to-edge distance perpendicular to the backbone, of the fiber closest to the center of each

sampling window. This produced 54 measurements, the mean and standard deviation of which were used to estimate the range of possible mean widths for the sample.

The survey was expanded to measure the orientation structure and fraction of turns and branches between each axis. Two images, one 40x and one 20x image of BDA stained tissue were obtained. A grid was placed on each image for bookkeeping purposes, however every box was counted. Two separate surveys, one for turns, another for branches, were conducted for each image.

After identification geometry of both turns and branches was quantified using simple imageJ tools. Ideal sharp turns can be described by three points in space: their apex, and a point on each of their legs. Turning axons are not ideal in this sense: instantaneous orientation fluctuates, a ray from the apex to a random point on the leg may not be parallel with the true long-range orientation, and axons turn with some radius, not instantaneously at a point. Each leg of the turn was approximated with a line segment, which were joined at the apex (see Figure 5.4).

The legs of branching fibers are not symmetric about its apex. Two legs are collinear; these will be referred to as the "trunk." The remaining leg will be referred to as the "branch." These terms reference the view that following one of the legs of the trunk will lead back to the root of the axon, however this assumption is not used in analysis. The branch is approximated by 3 line segments, one for each leg, all joined at the branch point. In analyses the trunk angle refers to the average angle of the two legs of the trunk, relative to the image.

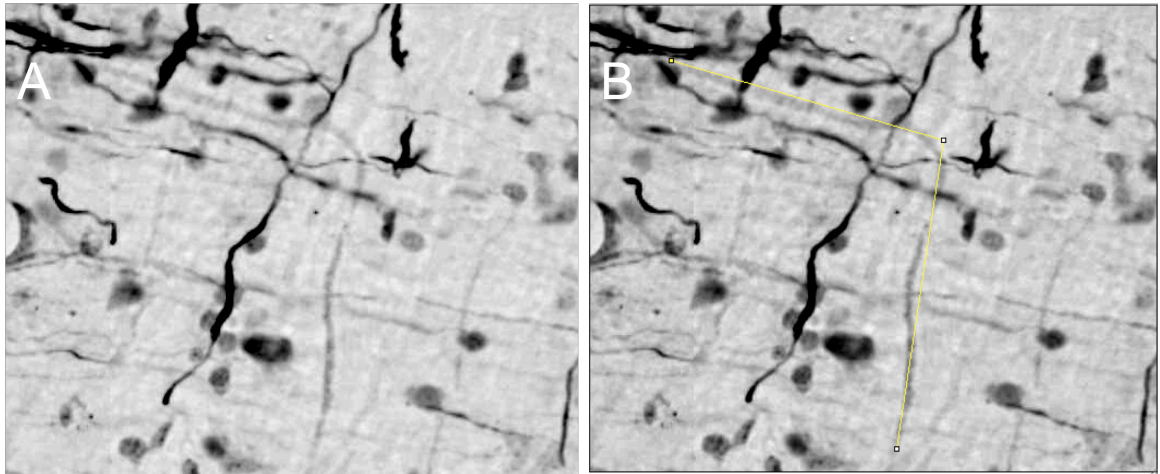


Figure 5.4. Turn geometry measurement. The turn is visible as a light gray fiber in panel (A). The yellow line in panel (B) shows approximation of the turn with two line segments joined at an apex, using the imageJ angle tool.

5.4 Results of Image Analysis

Patterns of Axon Orientation

Figure 5.5 shows an image of the pan-axonal label SMI-312 in the white matter below the hand region of the motor cortex. Visual inspection suggests there are two major orientations, although some fibers do appear to deviate from this pattern. These SMI-312 labeled fibers include axons that originate not just from primary motor cortex but also fibers that pass through this region regardless of their origin or target.

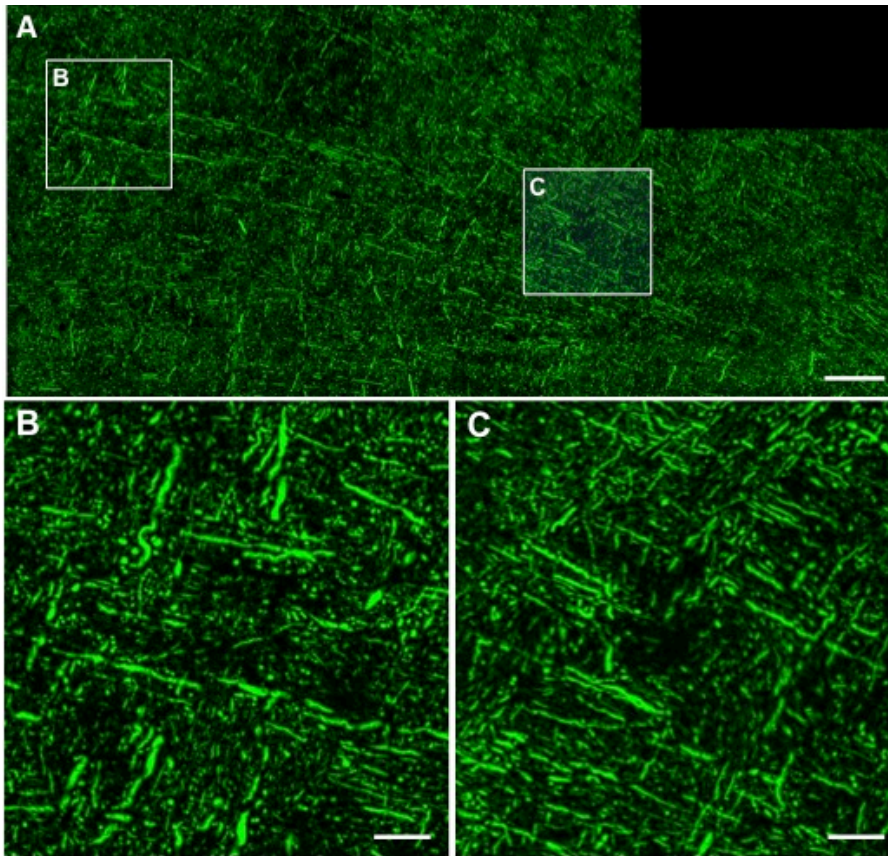


Figure 5.5. Pan axonal labeling. Panel A shows a montage of confocal images of subcortical white matter beneath primary motor cortex that was immunohistochemically stained with the pan axonal antibody, SMI-312 that stains all axons. Panels B and C are higher power images showing that most fibers distribute in approximately orthogonal directions in the x,y plane while others disappear into the orthogonal z-plane. Scale bar in A = 200 μm and in B and C = 50 μm .

Higher power images in Figure 5.5 B and C clearly show a tendency for fibers to align with the 2 dominant average orientations displayed in the image, even at length scales smaller than the 50 micron scale bar. Fibers that appear as truncated segments or small dots intersect the plane of section at angles close to the perpendicular, and have

3D orientation that may not be accurately captured by their projection in this image.

The image was interrogated to identify preferred orientations, estimate the fraction of fibers in each preferred orientation, and estimate the background level of randomly orientated fibers. For the purpose of comparison, the orientation distributions of axons in the image of Figure 5.5 were measured using three methods: Two-Point Correlation, Structure Tensor, and Path Probability (PP), the results of which are shown in Figure 5.6A-C. All three methods produced distributions with two large peaks corresponding to the two most common fiber orientations, with the center of the smaller peak between 64° and 69° for each method, and the larger between 160° and 163° . These primary orientations were almost perpendicular, agreeing with the separation of the lobes identified by dMRI to within its resolution. The separate methods produced a range of offsets from 83° to 86° , where offset is defined as the lesser of the two supplementary angles between the two orientations, i.e. a value between 0° and 90° . Unlike the other methods, PP also shows a minor direction at 97°

To visualize the anatomic distribution of fiber orientations, a color image was created based on the *PP* analysis of Figure 5.5. First the original image is converted to grayscale, so each pixel has brightness (intensity) matching that of the original image, where brightness is proportional to SMI-312 fluorescence. The human visual system has the ability to recognize a range of hues. Orientation at each pixel is specified as the angle that maximizes the $PP(r = 30\mu m, \theta)$ distribution calculated for that pixel. Orientation information is coded as hue, as shown in Figure 5.7, and mapped onto the image. Finally, the visual system can also perceive how saturated a color is. Saturation is related to how power is distributed among the visible wavelengths. A flat power spectrum produces a gray color, and has a saturation of zero, while maximum saturation corresponds to monochromatic light. This translates naturally to anisotropy – at low

anisotropy, all orientations are equally probable, and at high anisotropy, a single orientation is vastly more likely than others. This Hue-Saturation-Brightness (HSB) encoding allows us to represent a three-dimensional vector valued function on a two dimensional map. It has previously used by others in the neuroscience community [e.g. Budde and Annese].

The probability densities produced by each method gives the relative likelihood for a randomly selected *pixel*: i.e. $PP(r,\theta)$ gives the relative likelihood of finding two occupied points along some vector of length r and direction θ from another occupied point, minus contributions from two-point correlations and randomness. This means each fiber is essentially weighted by its diameter and length. This added importance for thicker fibers is not necessarily desirable or undesirable, but it must be taken into account when comparing the relative amounts of fibers in different peaks and background. Steps can be taken to remove this diameter weighting, such as only tabulating the results of the measurement for pixels on an edge, but the weighting and uncertainties they themselves introduce should be taken into account.

The Path Probability method was used to estimate the fraction of fibers in each direction, because of its good angular resolution and discrimination between isotropically distributed fibers and other sources of background. As detailed in the Image Analysis Methods section of this chapter, the estimate of background produced by the two-point correlation method includes contributions from fiber density variation and experimental details, making it unreliable. The two-point method applied to this image produces a very large background, much higher relative to the peaks than the amount of randomly oriented fibers estimated by visual inspection. Background in the distribution produced by the structure tensor method is smaller than the two-point,

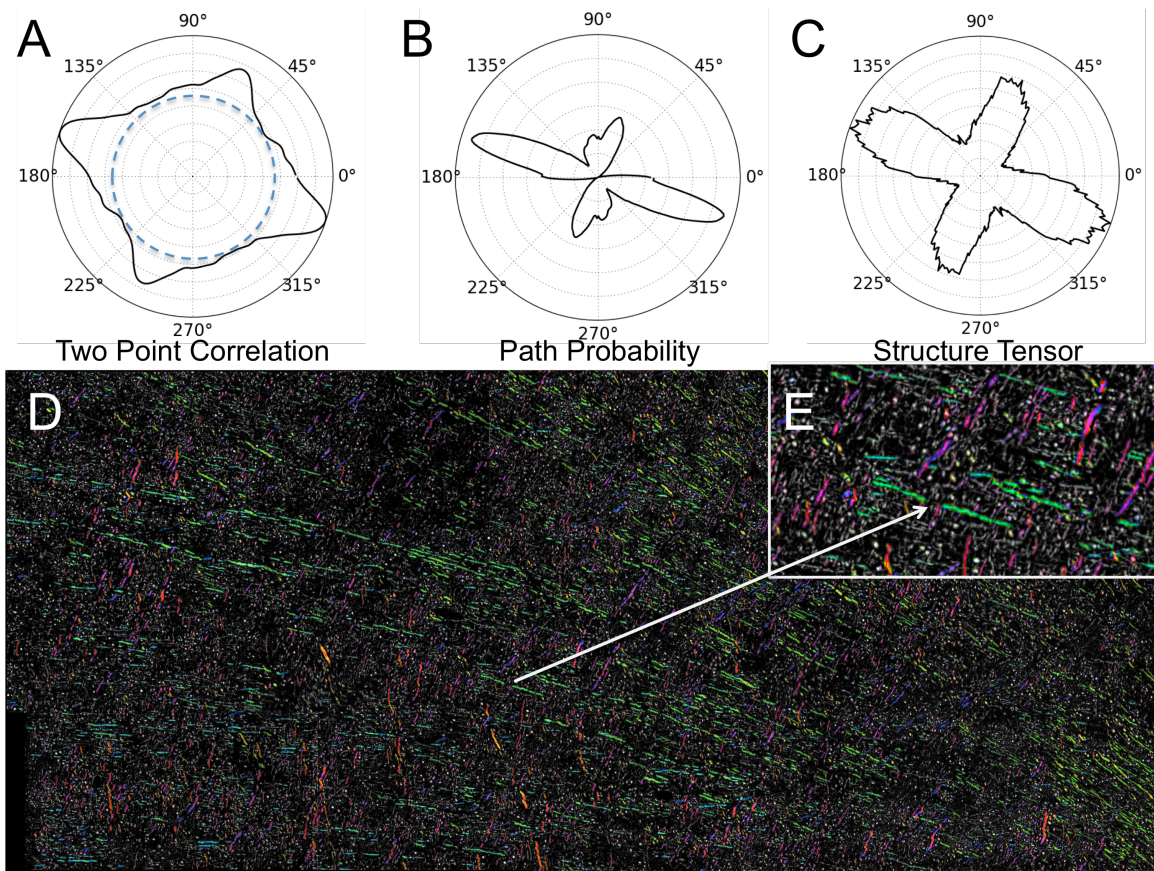


Figure 5.6: Comparison of different quantitative evaluations of orientation. Plots in Panels A-C show the whole Two-Point, Path Probability and Structure Tensor distributions. Units of radial axis are relative strength in the given angular bin. Autocorrelation (A) reveals a large isotropic background, (blue dashed circle) and primary orientations at 161° and 64° . Structure Tensor orientation distribution (B) shows primary orientations at 160° and 66° . Path Probability (C) reveals primary orientations of 163° and 69° as well as small peak at 97° . Panel D shows SMI-312 labeled fibers of Fig. 5.5 with Path Probability (PP) applied to code each fiber orientation in hue, saturation and brightness with hue of orientation according to the color wheel in Figure 5.7 and brightness proportional to the anisotropy of PP ($P_{max}/P_{average}$). Thus primary

orientations are revealed at 163° (green hues) and 69° (purple) plus for 19% of the fibers (reddish-orange) at 97° . An enlarged view is shown in E. Scale bar in D = $200\ \mu\text{m}$, in E = $50\ \mu\text{m}$.

however it is hard to estimate what that fraction is. Artifacts can be produced in this method if a window contains only a non-representative part of a fiber, such as its terminus, where the edge direction is not related to fiber orientation, or if the window contains multiple fibers, as detailed in Image Analysis Methods.

The mechanism by which local fiber orientation is governed is unknown, and we did not wish to assume normal, or an alternative distribution, of fluctuations around mean values. This precluded the use of fitting to estimate the amount of fiber area in each peak. Fortunately, peaks were well separated, so we were able to estimate the size of each peak through integration. For each distribution $f(\theta)$, our procedure was:

1. Estimate background level B as global minimum of $f(\theta)$. Total amount of isotropically distributed fibers is πB .
2. Identify local minimums m_i and local maxima M_i with some tolerance. Regions between local minimums are peaks. Overlapping peaks were identified as those where $|m_i - m_{i+1}|$ was significantly greater than zero, where significance was determined on a case by case basis with respect to background and M_i .
3. The peaks are characterized by the moments of $f(\theta) - B$, with the zero-moment corresponding to fraction of orientations in a peak, first moment the center of the peak, and second moment the width. For non-overlapped peaks, the moment integral can be taken between the entire range between the minimums:

Fraction of orientation in peak $F = \int_{m_i}^{m_{i+1}} (f(\theta) - B) d\theta$

Center of peak $M = \frac{1}{F} \int_{m_i}^{m_{i+1}} \theta (f(\theta) - B) d\theta$

Width of Peak $W = \frac{1}{F} \int_{m_i}^{m_{i+1}} (\theta - M)^2 (f(\theta) - B) d\theta$

4. This procedure must be altered for overlapped peaks. In this case, the integral is performed from the smaller of m_i, m_{i+1} to the next local maximum, M_i or M_{i+1} . In this region overlap is minimized, and the formula above can be adapted to estimate proper values by assuming that the distribution is symmetric around the local maximum. This of course automatically gives $M = M_i$. If a case is encountered where one peak is a shoulder of another, or a small peak sits on the tail of another such that both m are significantly above background, or if peaks are generally asymmetric around their maximums, this technique will fail and one will be forced to resort to fitting. Fortunately all distributions here had well enough separated peaks for these integral methods to be applied. Peaks all appeared to be symmetric around maximums, as they should be if width reflects random errors in orientation. The adapted formula, for the case of the overlap on the right side of the maximum, are:

5. Percentages are reported as $F/T, B/T$, where $T = \int_0^\pi f(\theta) d\theta$

Fraction of orientation in peak $F = 2 \int_{m_i}^{M_i} (f(\theta) - B) d\theta$

Center of peak $M = M_i$

$$\text{Width of Peak } W = \frac{2}{F} \int_{m_{i+1}}^{M_i} (\theta - M)^2 (f(\theta) - B) d\theta$$

The largest peak in the Path Probability was well separated enough to use the formulae described in step 3 of the procedure. The two smaller peaks were overlapped, necessitating the use of the formulae in step 4. Using the above procedure, 49.5% of fiber area was found to be in the peak centered at 163° relative to the image, 30% in a peak almost perpendicular to this one at 69°, while 19% were in a peak intermediate to these two at 97°. Only 1.5% of fibers were randomly oriented. The two large near perpendicular peaks correspond to the observations in this region using dMRI, we therefore refer to fibers with this orientation as “grid” fibers, and the remainder as non-grid. The weight of the smallest peak should be taken with a grain of salt, due to the area weighting discussed above. These correspond to the reddish-orange false colored fibers in Figure 5.6. Many of these are among the larger fibers in this section, with a mean diameter near 8 microns, compared to the mean for all fibers of 5 microns (unpublished data). It is probable that if we were able to sample on a per-fiber basis, the fraction of fibers in this peak would be substantially less than reported by Path Probability.

Thus the majority of fibers, about 80%, are observed to adhere to the grid structure. The nineteen percent of non-conformist fibers raise the possibility that some subpopulations may follow different organizational principles. There are fibers from sources other than the motor region in the region sampled. Fibers with different sources (i.e. cortex and midbrain) may follow different cues; this raises the possibility that there may be multiple grids. This would not be necessary, however, if fibers from the same source displayed non-grid behavior. Observations of non-grid behavior in a fiber

population with a common source would instead be indicative that the nature of a fiber's target, or its type, determines its geometry. To observe whether a group of fibers from a common source had similar aberrant fibers to the SMI-312 population, we examined the fibers stained with the BDA tracer, which all projected from a small region of the motor cortex controlling hand movement. An unprocessed microscopy image of these fibers is shown in Figure 5.8.

The fiber orientation distribution of the BDA tracer image was obtained using the Path Probability method (shown in Figure 5.9 C). The Two-Point and Structure tensor methods were also applied to check for peaks not resolved by Path Probability; none were found. Path Probability revealed two major directions at -3° and 70° , comprising 57.5% and 21% of the total fiber population respectively. The peak at 70° may appear to have a shoulder near 45° , but examination of the image suggests these (purple-blue fibers) appear due to curvature, not an additional preferred direction. No additional peaks were observed. Instead, the remaining 21.5% of fibers were randomly oriented. Figure 5.9 A and B display the HSB encoded results of the analysis in the same manner as Figure 5.6 D and E.

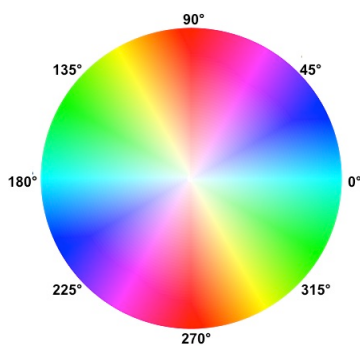


Figure 5.7. Mapping from hue to angle for color-coded orientation images.

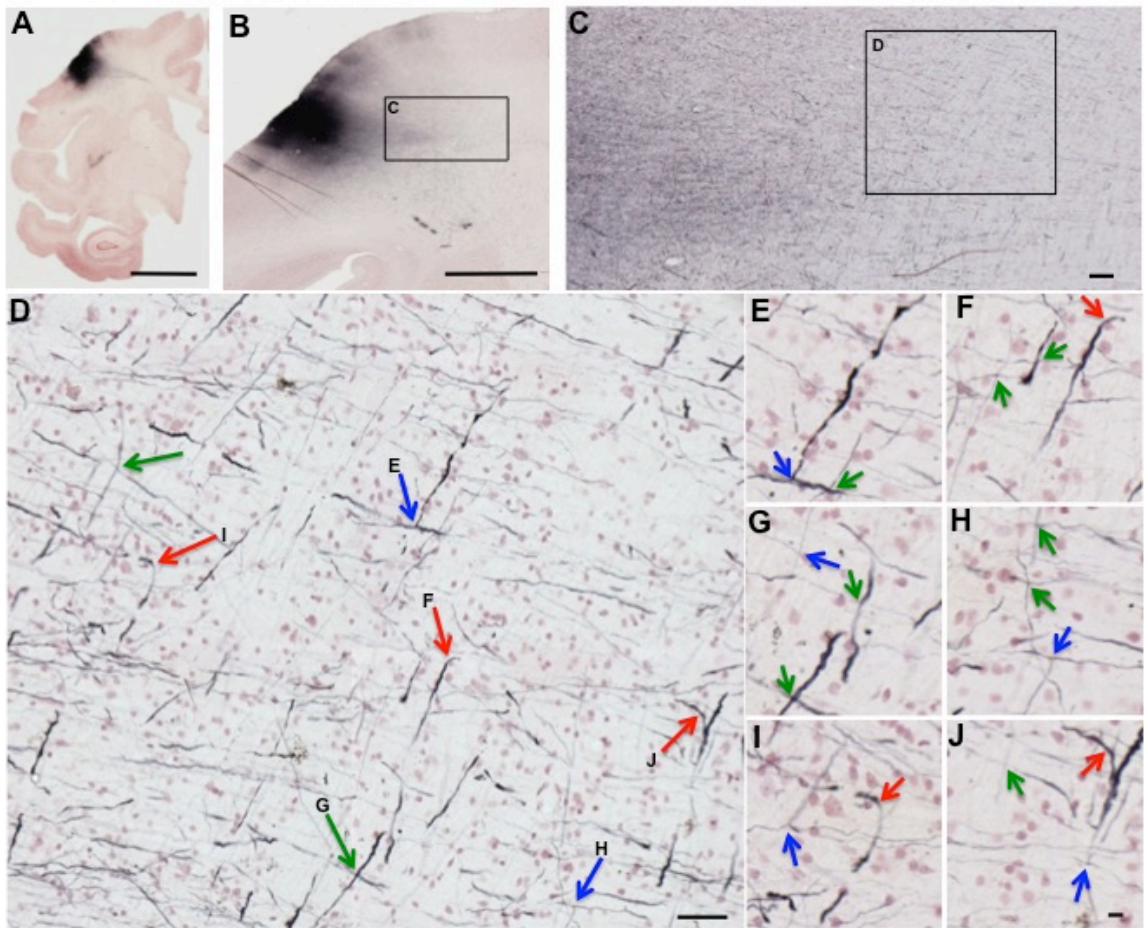


Figure 5.8 Panel A is a 30 micron section through the BDA injection into the precentral gyrus, counterstained with neutral red to show gray matter. Panel B is an adjacent section at higher magnification showing BDA labeled fibers leaving the injection site. Panels C and D show the fibers as they disburse into orthogonal directions. In D, fibers are identified as crossing (green arrows), branching (blue arrows) or making sharp turns (red arrows). Panels E through J show these and similar fibers at higher magnification. Scale Bars: A = 10 mm, B = 2 mm, C = 200 μ m, D = 100 μ m, J = 20 μ m for E-J.

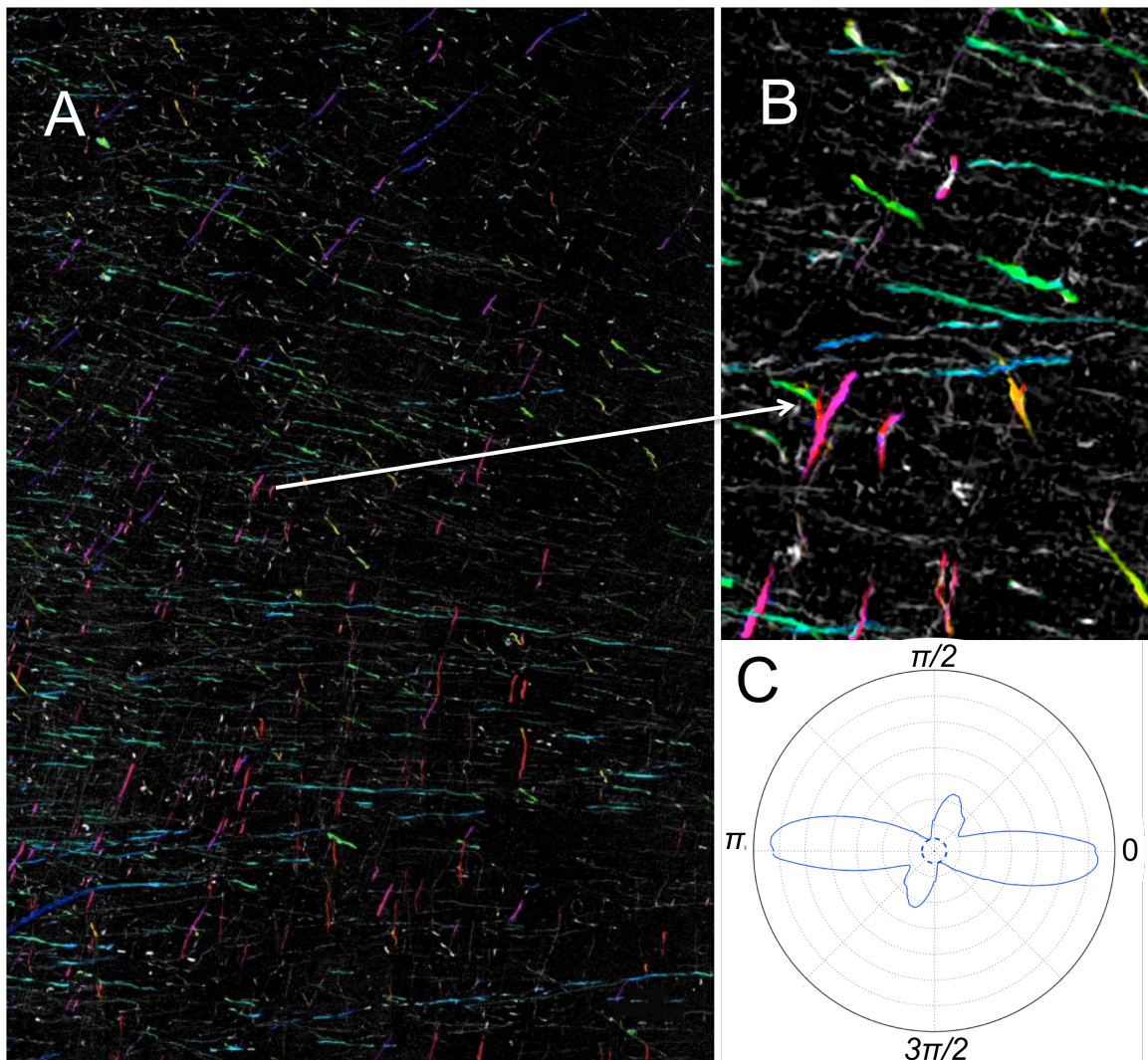


Figure 5.9 Analysis of BDA tracer image. Panel (A) used Path Probability with $R = 40 \mu\text{m}$ to analyze the BDA labeled fiber in Fig. 1C and encode their orientation in hue and saturation as was done for SMI-322 in Fig. 3. **Panel (B)** is a close-up view of the encoding. The orientation distribution in **Panel (C)** shows two primary orientations are present at 70° (reddish to green hues) and -7° (aqua to blue hues). These two primary directions account for about 80% of all fibers while the remaining 20% are isotropically distributed.

This population of fibers projecting from a the same region of the motor cortex contrast with the SMI-312 labeled population in having a large fraction of randomly oriented fibers. The large isotropic background is explicable by the proximity to the less organized grey matter. In fact, it is surprising that the observed degree of organization is achieved so soon after the fibers enter the white matter. The fraction of randomly oriented fibers noticeably decreases in deeper white matter, towards the right in Figures 5.8 and 5.9.

A minor point of similarity is the large fraction of fibers in the medial axis, approximately horizontal in both SMI-312 and BDA images. This likely reflects that motor fibers likely make up a large fraction of those labeled by SMI-312, although they are not equally represented in each axis. Still, the large number of BDA-labeled fibers perpendicular to the medial axis suggests that a large number of turning and branching events must have occurred.

Lastly, the population of BDA-labeled fibers shows only two peaks in the plane of section. This suggests that all long-range axons exiting the motor cortex navigate the white matter by means of the grid.

This result supports the hypothesis that non-grid fibers arise from a different source. It does not exclude the possibility that these fibers have different characteristics than the typical fiber. For example, we observed that the out of grid fibers in our SMI-312 sample were larger than average. The subpopulation of larger fibers may be expected to deviate from the grid. Larger fibers are able to transmit signals between areas very quickly, at the expense of energy [Perge, et al.] A grid trajectory imposes a

factor of $\sqrt{2}$ length penalty, as compared to a straight-line route, so it may be that a subpopulation of axons dedicated to rapid signal transmission are routed more directly to decrease transmission time. Unique myelin sheath proteins can identify large fibers. The orientation distribution of directly routed axons should show a peak corresponding to every target.

To investigate this hypothesis, we stained additional sections nearby the SMI-312 section with SMI-32, labeling axons that mainly originate from large projection neurons. As shown in Figure 5.10A, SMI-32 labels a fraction of fibers, as compared to SMI-312 (Figure 5.5). The fiber orientation distribution was extracted using the Path Probability method, which was again checked against distributions produced using the Two-Point and Structure Tensor, and is shown in Figure 5.10 C. The results of the analysis were spatially encoded using the HSB space of previous analyses (shown in Figure 5.10 B).

SMI-32 labeled fibers were concentrated in two major orientations offset by 69° , with 46.8% of fibers in a large peak at 150° (reddish-purple fibers in Figure 5.10 B), and 35.7% of fibers in around 81° (green fibers). In addition to this grid pattern, 6.8% of fibers formed a narrow peak around 44° (blue fibers). The remaining 10.7% of fibers were isotropically distributed; these may have resulted from the in-plane projection of axons intersecting the section at high angles. Based on tissue curvature, this section appears to have been rotated clockwise by about 90° during either mounting or imaging, compared to the other sections. If this is true, the largest component of the orientation distribution is again aligned with the medial-lateral axis.

Similar to the SMI-312 labeled fibers, a small number of fibers appeared to be ignoring the grid structure. In this population of large axons, however, they represented a smaller fraction than in the general population, 6.8% vs. 19.0%. These numbers cannot

be directly compared, because the distribution is weighted by area, and the blue fibers in the SMI-32 image appear to be of the same or smaller diameter than the axons in this image, while those in the SMI-312 image were larger than average. However, it is fair to say that this cannot account for the factor of three decrease, meaning that out of grid behavior is actually less common in the subset of large axons than in the general population. Though some long range fibers do deviate, they do not form a subpopulation following a different set of rules.

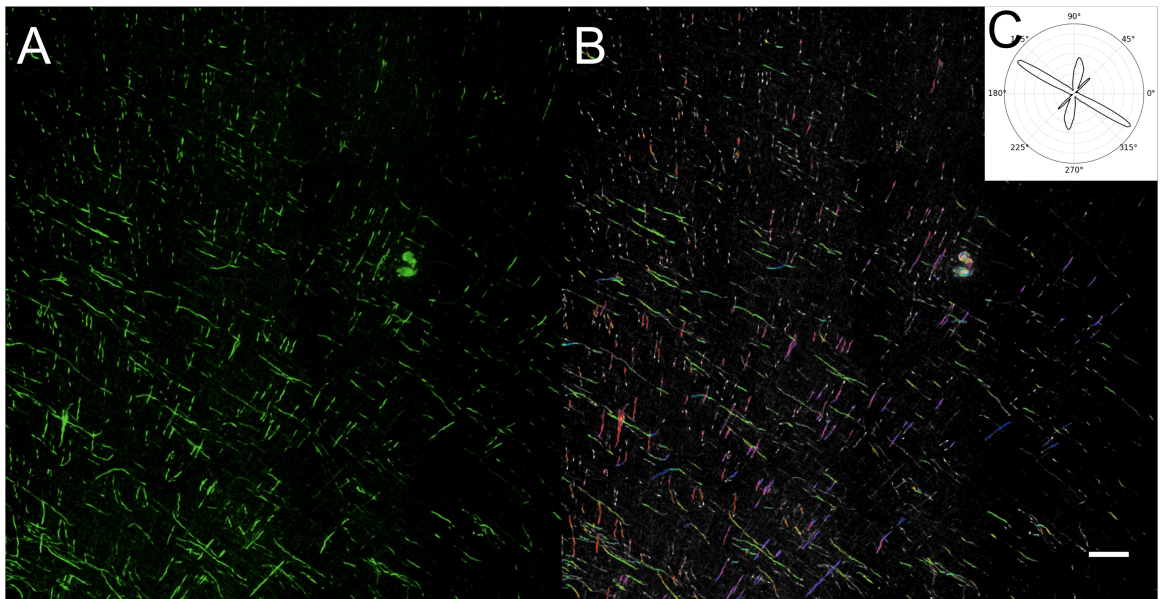


Figure 5.10 (A) Raw microscopy of SMI-32 stained fibers. Population is noticeably sparser than SMI-312 fibers (Figure 5.5.1). (B) Orientation-Hue encoded fibers. Fibers in primary orientations are green and purple, a subpopulation of blue fibers deviating from the grid are interspersed throughout.

Branching and Turning Rates, Anisotropy, and Alignment with Grid

Inspection of 3D confocal images by our neuroscientist collaborators revealed the existence of fibers branching, and making turns with radii comparable to their diameter (Wedeen et al., 2012). Three-dimensional images remove the ambiguity associated with discriminating between these structures and crossing fibers using conventional two-dimensional microscopy.

Unfortunately, the small size and experimental variability between available confocal images precluded their use in a systematic study of branching and turning. By comparing two-dimensional projections of crosses and turns to their 3D structure, we were able to learn to identify true turns and branches in two-dimensional images with good accuracy.

This allowed us to undertake a systematic survey of the branching and turning behavior of axons in the shallow white matter under the motor cortex, as displayed in Figure 5.8. With our available data, we were able to measure the rate of turns and branches per linear fiber length, the relative amount of turns between each pair of directions, the direction of branches from fibers in a given axis, and the alignment of these small scale features with the grid.

The total rate measurement was limited to a subset of the total analyzed region, because of the labor involved in measuring the length of every fiber in the sample. Direct measurement of the sampled fiber length in this region produced an estimate of 5.747 mm. The indirect measurement, produced by dividing the total area by mean fiber width, estimated the sampled fiber length as 5.558 mm, with lower and upper limits of 4.047 mm and 8.8868 mm, calculated as $(Total\ Area/Mean\ Width \pm Std\ Deviation)$. The good

agreement of the direct measurement with the most likely length value estimated through thresholding suggests that experimental drift was minimal.

A total of 9 turns and 8 branches were found in the sampled region. Using the directly measured 5.747 mm sampled fiber length gives an estimate of an average of 3.0 trajectory altering event in every linear millimeter of fiber. The total uncertainty in this rate due to error in the length measurement is likely to be small compared to that due to statistical fluctuations in event number. The confidence interval for the event rate was estimated by assuming that branches and turns are randomly distributed in space, so the number counted in a randomly selected area follows the Poisson distribution. If these events are clustered, this will lead to an overestimate of the rate, anti-correlation will lead to an underestimate. The confidence interval of a Poisson mean can be calculated through its link with the quantiles of the χ^2 (Chi-squared) distribution [Ulm]. For the $1 - \alpha$ confidence interval:

$$P(\lambda_L) = P(\chi_{2*N}^2 \leq 2\lambda_L) = \alpha / 2$$

$$(5.4.1) \quad 1 - P(\lambda_U) = P(\chi_{2*(N+1)}^2 \leq 2\lambda_U) = 1 - \alpha / 2 \quad [\text{Ulm}]$$

where N is the number of observations. In plain English, from Ulm: “ $2\lambda_L$ is simply the $\alpha/2$ fractile of a χ^2 variable with 2N degrees of freedom, while $2\lambda_U$ is simply the $1-\alpha/2$ fractile of a χ^2 variable with 2(N+1) degrees of freedom.” So, for example, the lower limit of the 95% confidence interval of a process where N events occurred in time T is:

$$(5.4.2) \quad \lambda_L = (Q\chi_{2*N}^2(0.025) / 2) / T$$

where $Q\chi^2_N(p)$ is the p th quantile of the χ^2 distribution with N degrees of freedom.

Applying these formulas to our turn counts gives upper and lower limits of 27 and 10 events in our region, which translates to a 95% confidence interval of 1.7/mm – 4.7/mm for the total event rate. If this result holds true for all cortical fibers, it would imply that even short fibers may have time to execute about four turns, while long-range fibers may turn and branch tens of times. It will be interesting to extend these measurements to other regions, and measure their dependence on variables such as distance from the cell body, and whether or not branches can also branch and turn.

The rate estimates suggest that turning and branching occur at rates high enough to allow for arbitrary connectivity with the entire trajectory of each fiber obeying grid geometry. This led to further investigation into their properties, namely: 1) do the incoming and outgoing legs of turning fibers align with the grid axes identified through orientation analysis, and 2) are turns between, and branches into, certain directions more

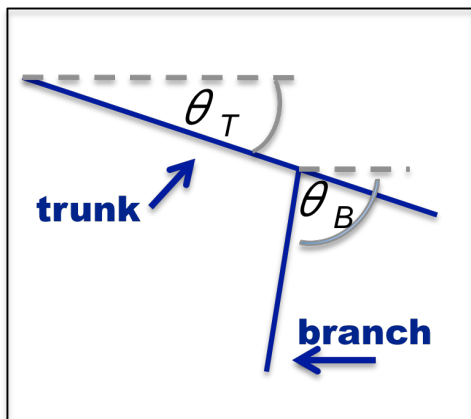


Figure 5.11. Quantification of Branch Geometry. Schematic illustrates definition of trunk angle, θ_T , and branch angle, θ_B . Angles are relative to the X-axis of the image. In the results that follow, counterclockwise rotation is defined as positive.

common than others, and does observed asymmetry align with the traditional targets of fibers from the motor area?

These questions can be answered simultaneously by measuring the geometry of turns and branches. First we will examine branching fibers. The geometry of a branching fiber can be described by the angle of its trunk and its branch relative to the image (see Figure 5.11). The distributions of θ_T and θ_B can be compared to the orientation distribution of all fibers. Asymmetry can be observed in certain combinations of θ_T and θ_B are more common than others. We must point out here that θ_T has a periodicity of π . This is because the trunk is not directed – we cannot ascribe unique properties to either end. This is not the case for the branch – one end is pointed away from the apex, so it has a periodicity of the full 2π .

A survey of a large 20x image of BDA stained tissue, and area of 208,000 square microns, produced a total of 25 branches. Plotting θ_T vs θ_B produced four groups, with a single outlier, as illustrated in Figure 5.12. Each group corresponded to a combination of the primary axes observed for the full population of fibers, with the trunk aligned with either the medial-lateral or superior-inferior axis. The medial-lateral trunks are near the -7° major axis, and the average of the superior-inferior trunks is about 80° , offset by 10° from the peak of the superior-inferior axis identified in the bulk population of fibers, most likely due to tissue curvature. Each group of trunks has two groups of branches, into the positive and negative directions of the complementary axis. Neglecting the outlier, 71% of trunks were aligned medial-laterally, and 19% superior-inferiorly. This closely matches the fraction of non-random axons in each axis determined by the Path Probability orientation analysis, 73% and 32%. Interestingly, branching was highly anisotropic. Of 17 branching fibers with trunks aligned with the medial-lateral axis, 76%

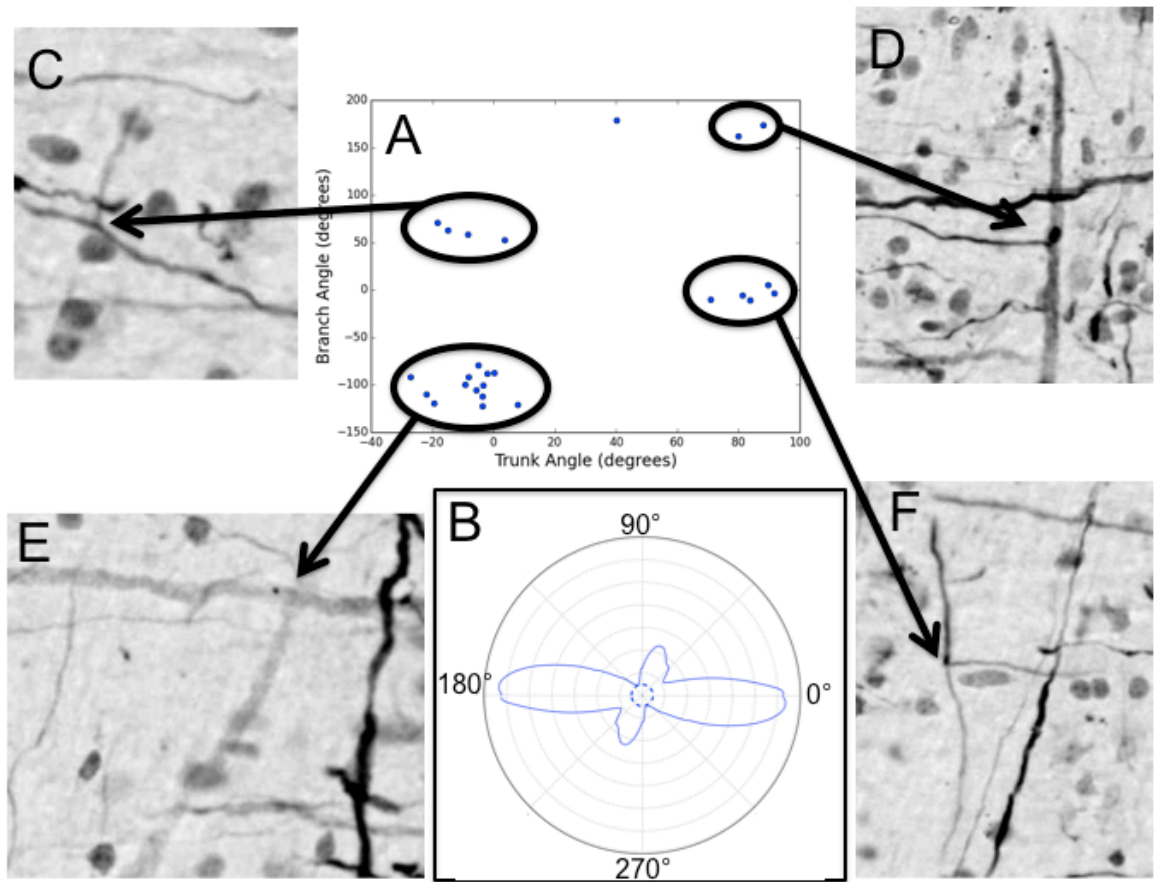


Figure 5.12. Geometry of branches. (A) Four clusters of points correspond to branching fibers with trunks aligned one grid axis sprouting branches aligned with the other grid axis. Trunk angles are shown on the x-axis, and branch angles on the y-axis. The distribution of orientation for all fibers is shown in (B). Typical examples from each type of branching event are shown in (C) – (F).

(13) had branches that descended inferiorly. The remaining 24% (8) with trunks aligned with the medial-lateral axis were more evenly distributed, with 62.5% (5) medial branches and 37.5% (3) lateral branches.

A survey of a separate 260,000 square micron section of tissue imaged at 40x revealed similar results. Twenty total events were observed, 70% of which had trunks aligned with the medial-lateral axis. This group of axons showed a similar asymmetry. Of branching axons with trunks aligned with the medial-lateral axis, with 64% of branches into the inferior direction. Axons with trunks aligned with the superior-inferior axis had a two-to-one excess of branches into the medial direction.

Turning requires some modifications to the analytical tools used above. Like the trunk of branches, there is an ambiguity to which leg of the turn a signal enters and

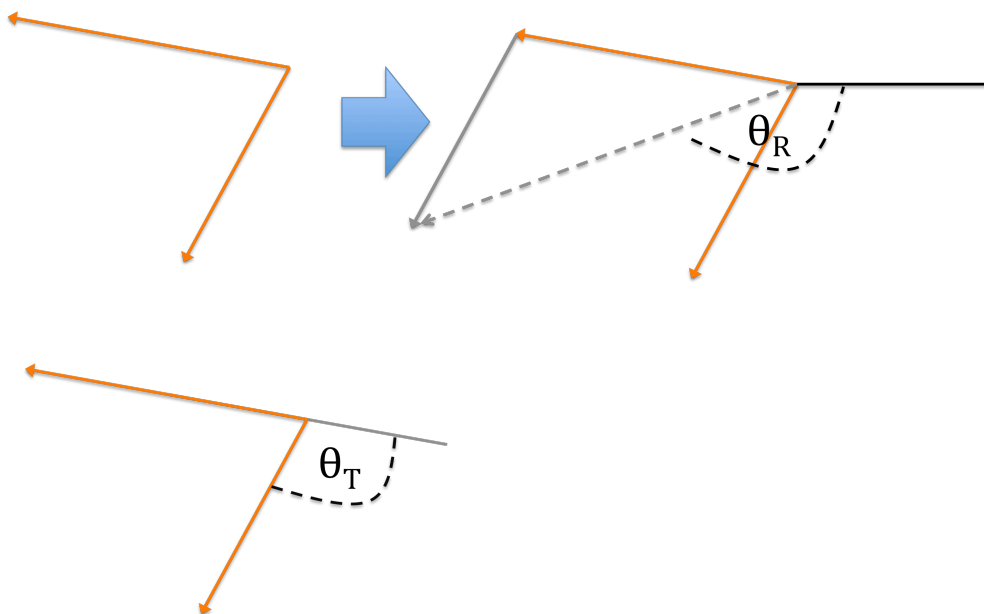


Figure 5.13 Quantification of Turn Geometry. Turns can be quantified by two angles: θ_R the angle the resultant (gray dashed arrow) of the two legs makes with the image (black line = x-axis), and θ_T , the angle the axon must turn through to change orientations.

exits. Any analysis must be agnostic to which branch is which, thus we cannot simply plot the angle of leg one vs. leg two. A branch can be defined by two angles, as shown in Figure 5.13. Algebraically, these are the average of, and the difference between, the angles the legs make with the image, although we equivalently use the supplement of the difference, for reasons we shall explain shortly. Geometrically, the average of the angles can be viewed as the angle of the resultant formed by normalizing the length of the two legs, and adding them tip to tail. The supplement of the difference in angles is the amount of degrees the axon must alter its trajectory by in order to execute the turn. It is a more appealing number than the angle between the legs because unlike that angle, it is large when the change in trajectory is large.

In contrast to the rate measurements, where the number of turns and branches was approximately equal, turns were outnumbered in this sample two to one, with only twelve examples found. This may be due to small number fluctuations, or possibly a lower rate of turn recognition in the lower resolution 20x image than the 40x.

Turns were extremely anisotropic. The resultant angle of two thirds of the turns matched that of turns with legs extending from the apex in the lateral and inferior directions. Two turns had legs extending in the superior and medial directions, one of the twelve had legs in the lateral and superior directions, and the remaining turn was ambiguous.

The turning angle θ_T matched the expected value of about 103° for several of the lateral-inferior turns. Half of these fibers, however, turned through angles less than this by more than ten degrees. This may be due to an experimental limitation: if a fiber exits the plane of the thin section before completing its turn, θ_T will be reduced from its true value. This is actually a general limitation of two-dimensional microscopy, since thicker

sections will decrease the likelihood of this effect, but increase the error in angle, due to projection through the slab.

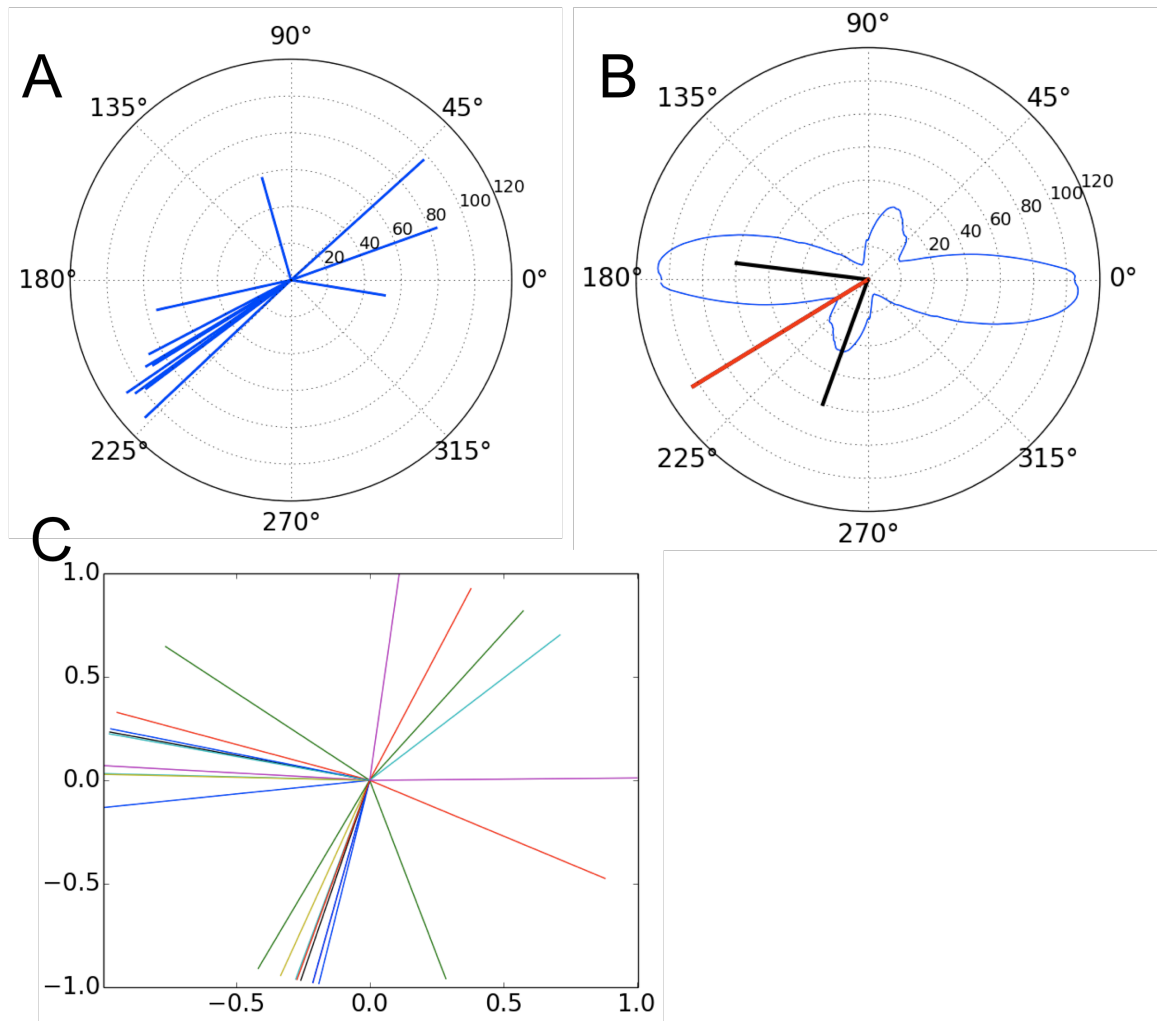


Figure 5.14. Distribution of Turns. Panel (A) shows the distribution of θ_R vs θ_T , with θ_R on the polar axis, and θ_T on the radial axis, for measured turns. θ_R is clearly clustered around about 210° degrees, and the turning angle for most of this group is greater than 100°, although some are less, possibly due to truncation. Panel (B) shows the orientation distribution of all fibers. The solid black lines represent a turn with legs in the lateral and inferior directions. Their resultant is at 211.5°, with a turning angle of 103°,

corresponding very well to the observed behavior. Panel **(C)** shows an overlay of turn schematics with apex translated to (0,0), demonstrating the abundance of negative vertical-to-negative horizontal turns, as well as a few between other directions, and one obtuse outlier (green line), that corresponds to a turn in the main group according to θ_R , but with a θ_T of about 75° .

A survey of a smaller section of tissue imaged at 40x revealed similar results. Twelve total turns were observed, of which 58% were lateral-inferior. This is a smaller anisotropy than observed in the 20x sample, but is still greater than twice the fraction expected for isotropic turning.

The directional asymmetry in turning and branching are quite striking, with 60% of observed branches connecting the lateral and inferior directions, and close to a three to one preference for the inferior direction in branching fibers with trunks aligned with the medial-lateral axis. This asymmetry is strongly supportive of the hypothesis that axons navigate the white matter by means of turns between the grid axes. The largest fraction of axons from the motor cortex are known to target the cerebellum, pons and other structures in the hindbrain, as part of the pyramidal, or corticospinal and corticobulbar tracts. These hindbrain structures are medial and inferior to the motor area. Axons in the grid targeting the hindbrain would be expected to descend medially, and either turn into the inferior direction, or extend a branch inferior. The observed turn would have legs extending laterally and inferiorly from its apex. The most common target for these fibers then corresponds to the most commonly observed turns and branches.

5.7 Implications for Grid Structure and Long-Range Trajectories

Our findings can be summarized into two major points:

1. The grid structure extends down to length scales of a few tens of microns, and the observed collective behavior at the mesoscale is not emergent, it is a result of microscale organization. Turning and branching occur at sufficient rates for the grid to be the primary organizational principle for all white matter.
2. Long-range trajectories are a result of a series of discrete events, namely turning and branching, at the microscale level.

Turn and branch based navigation is a necessary result of the strict adherence to the grid system at the micro level. This suggests that whatever the functional role of the grid, be it a navigational principle, temporal regulator, or otherwise, it may be necessary, or at least maximizes its effectiveness, if it is enforced at the scale of a few microns.

Mathematical Modeling of Connectivity

The functionality of the brain is largely determined by its connectivity. Connectivity, in turn, is the product of the routes taken by axons. One way to quantify connectivity in terms of structural parameters is through “potential connectivity” of a neuron. We define potential connectivity, $PC(\mathbf{r}_1, \mathbf{r}_2)$, as the probability there will be a connection between from a neuron at \mathbf{r}_1 to a neuron at \mathbf{r}_2 as a function of their locations. We are interested in the shape of $PC(\mathbf{r}_2; \mathbf{r}_1)$: $PC(\mathbf{r}_1, \mathbf{r}_2)$ for some choice of \mathbf{r}_1 . For example, a neuron that always targets a specific location \mathbf{R} would have $PC(\mathbf{r}_1, \mathbf{r}_2) = \delta(\mathbf{r}_2 - \mathbf{R})$, and a neuron that grows an axon a random length in a random direction would have $PC(\mathbf{r}_2; \mathbf{r}_1) = \text{constant}$. In the first case, the variance of the distribution is zero, in the second case it

tends to infinity with the size of the brain. It is probable that $PC(\mathbf{r}_2; \mathbf{r}_1)$ is peaked around one or more \mathbf{R} . In a traditional view, the variance of $PC(\mathbf{r}_2; \mathbf{r}_1)$ around each peak would be a function of quantities such as the variance in axon angle.

In a grid, the variance of axon angle tends rapidly to zero with distance. Our observations suggest instead $PC(\mathbf{r}_2; \mathbf{r}_1)$ is determined by branching and turning rates.

Consider, for example, the distribution of contacts neurons make on the opposite side of one of the folds in the brain, known as a gyrus. The spatial distribution of the terminal ends of the axons is a function of branching and turning rates. The white matter in a gyrus is typically on the order of a single millimeter thick, just enough for most

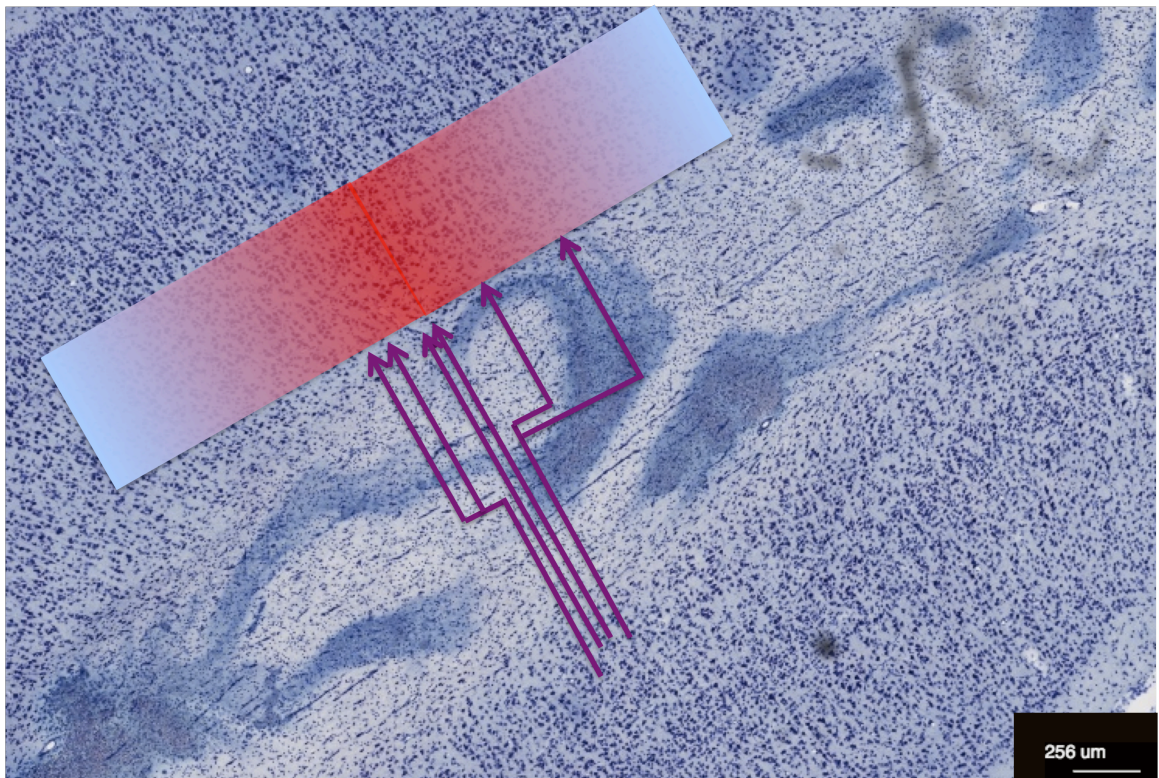


Figure 5.15. Axons crossing a gyrus. A hypothetical distribution of the terminals of axons crossing this gyrus is visualized by a heat map. The distribution is determined by branching and turning, indicated by purple arrows.

axons to turn into a trajectory parallel to the white/grey boundary, then back into a trajectory taking them into the opposite side of the gyrus, as illustrated in Figure 5.15. A simple model of this system starts with axons that turn randomly with constant probability at any point along their length, although turns in different directions may occur with unequal probability. For simplicity, we consider the distribution in the X dimension for fibers growing between two sides of a gyrus separated by a distance of Δ in the Y dimension. We also institute a no backtracking rule. Backtracking should be suppressed due to its waste of material and transmission time. Turn probabilities can be described by a two rates, λ_x , the mean number of turns into the X direction by fibers growing in the Y direction per unit length, and λ_y , the mean number of turns into the Y direction by fibers growing in the X direction. The no backtracking rule prohibits

If turns occur at random, the length of fiber between turns will be exponentially distributed. This is a well-known result from the study of Poisson processes. Since the no backtracking rule prohibits growth in the $-Y$ direction, the number of segments oriented in the Y direction is Poisson distributed:

$$(5.7.1) \quad P(N_Y = k) = \frac{(\lambda_x \Delta)^k e^{-\lambda_x \Delta}}{k!} = \frac{(\Delta / \mu_x)^k e^{-\Delta / \mu_x}}{k!}$$

the second parameterization is in terms of μ_x , the mean distance between turns. This allows us to derive the expected horizontal displacement at Δ . An axon with N segments oriented in Y direction will have N-1 segments oriented in X, with exponentially distributed lengths. Due to the no-backtracking rule, these segments will all be in the same direction, and their lengths will add. The sum of N independent exponentially distributed random variables is the Erlang distribution:

$$(5.7.2) \quad f(L; N, \lambda_y) = \frac{\lambda_y L^{N-1} e^{-\lambda_y L}}{(N-1)!} = \frac{L^{N-1} / \mu_x e^{-L/\mu_x}}{(N-1)!}$$

The length distribution is a sum of Erlang distributions, weighted by the probability of an axon with N segments oriented in X:

$$(5.7.3) \quad P(L) = (\lambda_x \Delta) e^{-\lambda_x \Delta} \delta(L) + \sum_{N=2}^{\infty} \frac{(\lambda_x \Delta)^N e^{-\lambda_x \Delta}}{N!} \frac{\lambda_y L^{N-2} e^{-\lambda_y L}}{(N-2)!}$$

$$P(L) = (\Delta / \mu_x) e^{-\Delta/\mu_x} \delta(L) + \sum_{N=2}^{\infty} \frac{(\Delta / \mu_x)^N e^{-\Delta/\mu_x}}{N!} \frac{L^{N-2} / \mu_y e^{-L/\mu_y}}{(N-2)!}$$

The term outside the sum represents fibers that do not turn. The mean value of the Erlang distribution described by Equation 5.7.2 is $N\mu_y$, and its variance is $N\mu_y^2$. The relative deviation is $1/\sqrt{N}$, maximized when fibers make a single turn crossing the gyrus.

This has an interesting implication for connectivity. Fibers traveling short distances have a relatively broad distribution of potential targets. The areas occupying opposite sides of a gyrus perform related computations – widely distributed connectivity is likely to be beneficial. Conversely, a long distance pathway will make many turns and branches, and its targets will be concentrated in a small region. This may allow the brain to concentrate long distance connections in their intended target regions.

In reality, turning and branching behavior may include such effects as correlation and spatial variation in turning probability. Another interesting effect is the interaction with the curved geometry of the brain. Curvature may act as a funnel, effectively changing the size of a region. Because of curvature, two fibers that turn near

one another may have widely separated terminals. This divergence hints at “chaotic” behavior, which is interesting given the debate on where connectivity falls on the continuum between deterministic and random.

Biological Implications

These findings have some immediate implications for the traditional biological understanding of the brain as well. The conventional view of pathways between different areas of the brain may need to be revised. Neuroscience envisions brain pathways as relaying a representation of the processing done by a particular area to another area where it can be used. For instance, visual information is combined with proprioceptive information, resulting in what athletes know as hand-eye coordination. The physical realization of the pathway was thought to be fibers organized into bundles of parallel fibers, like streamlines in fluid, or strings under tension. We have shown that instead, trajectories consist of linear paths punctuated by sharp turns.

For axonal fibers to remain as part of a coherent pathway with other fibers from the same origin, branches and turns must be coordinated. This implies so spatial variation in the probability of turning and branching events, or interaction between axons. It is known that axons secrete chemicals, the semaphorins, that can deflect other axons; it is possible that they may be able to initiate turning and branching behavior as well. Large concentrations of turns have not been noticed, although they have not been specifically looked for, to our knowledge, which raises the question of how they are related to one another spatially.

There are also functional implications. For example, action potential propagation is known to be disrupted at branch points. Branches were thought to be uncommon in the white matter, our measurements suggest that most axons of the motor cortex have

branches, and the grid makes it likely that others do as well. Propagation failure may be more important than commonly recognized. This can be combined with the possibility of widespread axon degeneration in the developing brain. O’Leary and Takashima observed branching axons in the spinal tract. During development, one leg of the branched axon would often die back, leaving either a sharp turn or linear fiber. This degeneration is known to occur if the information transmitted by an axon is not being used – the neuron trims the axon back to avoid wasting energy. Widespread branching may allow developmental flexibility, at the cost of information loss in transmission during the early stages of life.

These small radius turns and branches place an important constraint on the most commonly used brain mapping technology, dMRI tractography. This technique connects neighboring voxels in a dMRI scan if the orientation of their peaks line up. A line of connected voxels between two regions of grey matter is interpreted as a “tract” of axons connecting neurons in the two regions. All current dMRI technologies average diffusion over voxels that are far larger than microscopic axon turns and branches, and even high angular resolution techniques like the aforementioned Diffusion Spectrum Imaging cannot resolve turns and branches. This can lead to errors in the reconstruction of axonal tracts. Wedeen, et al., for example, suggest that dMRI tractography renderings of the corticospinal tract from cortex to peduncle as a smooth arc [e.g., Catani et al.] are due to error in the resolution of fiber orientations, since this smooth tract disagrees with observations of the axons obtained from high resolution microscopy [Wedeen, et al. 2012b]. While axonal branches and turns may be too small to be spatially resolved with present or foreseeable dMRI, these structures may potentially be reflected and mapped with other features of diffusion contrast [Assaf et al., Callaghan, et al.]. The grid poses additional challenges to dMRI tractography. Adjacent parallel fibers, identified and

named “kissing fibers” [Basser, et al.], may be a ubiquitous phenomenon as fibers navigate along and across grid axes. These cause ambiguities in tractographic reconstruction. Thus, these observations pose a notable challenge for dMRI of the human brain connectome, as well as opportunities to better understand and map brain connectivity.

6. Discussion and Future Prospects

The analyses performed in this dissertation have demonstrated two ways in which spatial analysis can shed light on the inner workings of the brain. In our study of astrocytes, we ultimately showed that the prevailing belief that astrocytes play an active role in protecting the cortex from the toxic amyloid-beta plaques of Alzheimer’s disease is incorrect. This illustrates the use of spatial information as a proxy for difficult-to-observe processes. A full understanding of astrocytes response would require knowledge such as gene expression as a function of amyloid-beta in the region around the astrocyte, what chemicals were absorbed and released by the astrocyte, and their effects on surrounding neurons. However, this exquisite detail is not necessary to dispute the hypothesis that astrocytes are sent to the site of plaques, like infantry on the front lines. From spatial information alone, we can deduce that instead the astrocyte system is itself disrupted by Alzheimer’s, and that another cell type must be responsible for defense.

We also observed a previously unknown aspect of astrocyte biology, a force with a repulsive core up to about 18 microns, and a weakly attractive well extending another 20-30 microns. This is 13 microns greater than the average diameter of the astrocyte, but less than the extent of the mature astrocyte’s processes. Both the origin and function of

this force is unknown. It may be a frozen in remnant of development, when astrocytes are establishing their position in the cortex, and may be a result of chemical signaling or mechanical contact between the nascent processes of immature astrocytes. In the second case the 18 micron range of the force would reflect the size of the processes of immature astrocytes when their density reaches the point where interaction becomes common. The first case implies a novel chemical messenger, similar to the semaphorins in neurons. Future investigation will involve the existence and character of the interaction in primate species. Systems where astrocytes are mobile will help elucidate the nature of the force. Developing brains are an obvious case of such a system; it will also be interesting to study astrocyte interactions in gliomas. Gliomas are a common type of malignant brain cancer, making up 80% of all malignant brain tumors [Goodenberger and Jenkins]. Astrocytes in gliomas divide, and are mobile, so it may be possible to observe this interaction. These are not normal astrocytes, of course, so the interaction may be altered or absent.

Our successful investigation into the role of astrocytes leads us to investigate other populations of cells. Microglia, are known to be mobile, entering an amoebic state to migrate to injury, toxins, or foreign cells such as bacteria. It is not known how the spatial distribution of the microglial population changes in response to a diffuse insult, such as the plaques of Alzheimer's. They are assumed to be attracted to plaques, hence high density should be expected near plaques, with low density at farther distances. Our experience with astrocytes, however, suggests that observations may be misleading, and that interesting interactions may have gone unobserved.

The interplay between astrocytic domains and their regulatory function also leads to interesting uses of spatial information. For example, how does the concentration

of a drug depend on the configuration of astrocytic domains? Do neurons belonging to the same domain act as any kind of functional subunit? Answering these functional questions is much easier experimentally if the domain can be approximated without direct imaging of the processes, as we have done using the Voronoi tessellation. One function of the repulsive force between astrocytes may be to regulate domain size. This force may then vary between brain structures and species. The range of the force was observed to vary among members of our cohort. The manipulation of the concentration of various neurotransmitters is a huge industry, and forms the backbone of neuropharmacology. Billions of dollars a year are spent on antidepressants, which primarily regulate the neurotransmitter serotonin. The illegal narcotic cocaine increases the concentration of three key neurotransmitters, dopamine, serotonin, and epinephrine. It would be interesting to model how the spatial distribution of astrocytes effects the regulation of these important chemicals, and how this can be manipulated by drugs.

Our analysis of axons shows a system in which the role of space is paramount to function. This can be deduced by the strict adherence to the grid pattern at a broad range of scales. Targeting a distant point is a difficult task for a cell, and it is not surprising to find some interesting pattern in the spatial structure of axons. The description and validation of this structure, however, requires novel imaging techniques and precise mathematical tools.

The connectivity of the brain determines its function. A large amount of research focuses on the modification of connectivity during the brains lifetime. This research is justified: the modification of connection strength is the physical basis of learning, and the loss of connectivity due to axon death probably underlies the mental decline associated with aging. [Peters et al.] The brain is unique among networks, however, in

how its initial connectivity is established. Neurons are initially disconnected from one another, and related to one another spatially. The axons that eventually connect them map this spatial relationship into connectivity. Some simple spatially dependent network models have been proposed, for example separation based connection probability in models of the airport and internet hub networks. [Daqing et al.] The spatial-connectivity mapping in the brain is likely to be much richer, and has the added benefit that there are a large number of brains to measure the properties of, unlike many networks.

The development of the brain creates a novel set of questions, based on the translation of the structural properties of single cells in properties of a network. An example might be the relationship between turning probability and the degree distribution of the brain, or the average distance between nodes.

The observations of the grid at the axonal scale raise a host of interesting physical questions. For example, the modeling of 3D trajectories comprised of grid-like segments in non-Euclidean geometry may turn up interesting statistical properties, such as relationships between first-passage times and curvature or turning probability. Modeling should help to determine how deterministic the pattern of turns and branches of a single axon must be in order to produce realistic connectivity patterns.

The grid may also affect signal transmission characteristics. It imposes a Manhattan distance metric (L_1 norm) for example, which means that all non-backtracking paths between two points are the same length. Signals transmitted between areas along different axons with different sequences of turns will arrive at the same time. The L_1 norm has particularly interesting implications for traveling waves of action potentials in the brain. A circle in Manhattan geometry is a square. Action potentials

could build up on the edges of a spreading square, creating coherent waves at 45° to the grid axes. Oscillations in the hippocampus appear to travel at about 45° to the axes of the hippocampal grid measured using DSI.

Measurements of correlations between these events will help elucidate how pathways are formed. They will also pave the way for exploration by biologists into the signaling behind branching and turning. Aberrant connectivity is thought to underlie schizophrenia, and possible autism, understanding the signaling underlying the formation of pathways should help expose the causes of these conditions. Interestingly, schizophrenia emerges later in life, typically in young adulthood, although its roots are thought to lie in development. Long-range connectivity should be established by this age. This may implicate branching axons as the culprit, since connectivity patterns may be altered by the degeneration of branches, as we discussed earlier.

The brain is a unique system in that it translates small-scale physical processes, such as axon growth and cell division, and environmental regulation, into a large complex network. It is a rich field of study, and deserves to be on the frontier of physics. We hope this dissertation demonstrates why spatial information is invaluable for the understanding of the brain.

Bibliography

- Allen, Nicola J., and Ben A. Barres. "Signaling between glia and neurons: focus on synaptic plasticity." *Current opinion in neurobiology* 15.5 (2005): 542-548.
- "Latest Facts & Figures Report | Alzheimer's Association." *Latest Facts & Figures Report*. Alzheimer's Association, 2014. Web. 08 Dec. 2014. <http://www.alz.org/alzheimers_disease_facts_and_figures.asp>
- Y. Assaf, T. Blumenfeld-Katzir, Y. Yovel, P. J. Basser, AxCaliber: a method for measuring axon diameter distribution from diffusion MRI. *Magnetic Resonance in Medicine* **59**,1347-54 (2008).
- Le Ballac M, Mortessagne F, Batrouni G. *Equilibrium and Non-Equilibrium Statistical Thermodynamics*, Cambridge University Press, 2004
- Barber, C.B., Dobkin, D.P., and Huhdanpaa, H.T., "The Quickhull algorithm for convex hulls," *ACM Transactions on Mathematical Software*, 22(4):469-483, Dec 1996, <http://www.qhull.org>
- P. J. Basser, S. Pajevic, C. Pierpaoli, J. Duda, A. Aldroubi, In vivo fiber tractography using DT-MRI data. *Magnetic Resonance in Medicine* **44**, 526-32 (2000)
- Bear M, Connors B, Paradiso M. *Neuroscience: Exploring the Brain*. Lipincott, Williams and Wilkins, 2007
- Bernsen, John. "Dynamic thresholding of grey-level images." *International conference on pattern recognition*. 1986.
- M. D. Budde, J. Annese, Quantification of anisotropy and fiber orientation in human brain histological sections. *Frontiers in Integrative Neuroscience* **7**, 3, (2012).
- Brodmann, K. *Vergleichende Lokalisationslehre der Gro hirnrinde*. Verlag von Johann Ambrosius Barth. Leipzig, 1909.
- Brillinger, David R. "Some history of the study of higher-order moments and spectra." *Statistica Sinica* 1.465-476 (1991): 24J.
- Brody, Howard, et al. "Map-making and myth-making in Broad Street: the London cholera epidemic, 1854." *The Lancet* 356.9223 (2000): 64-68.
- Brookmeyer, Ron, et al. "Forecasting the global burden of Alzheimer's disease." *Alzheimer's & Dementia* 3.3 (2007): 186-191.
- Budd, Julian ML, and Zoltán F. Kisvárday. "Communication and wiring in the cortical connectome." *Frontiers in Neuroanatomy* 6 (2012).
- Buldyrev, S. V., et al. "Description of microcolumnar ensembles in association cortex and their disruption in Alzheimer and Lewy body dementias." *Proceedings of the National Academy of Sciences* 97.10 (2000): 5039-5043.
- Burbach, Guido J., et al. "Laser microdissection reveals regional and cellular differences in GFAP mRNA upregulation following brain injury, axonal denervation, and amyloid plaque deposition." *Glia* 48.1 (2004): 76-84.
- Bushong, Eric A., Maryann E. Martone, and Mark H. Ellisman. "Maturation of astrocyte morphology and the establishment of astrocyte domains during postnatal hippocampal development." *International Journal of Developmental Neuroscience* 22.2 (2004): 73-86.
- Calka, Pierre. "An explicit expression for the distribution of the number of sides of the typical Poisson-Voronoi cell." *Advances in Applied Probability* (2003): 863-870.
- P. T. Callaghan. *Principles of Nuclear Magnetic Resonance Microscopy* (Oxford University Press, Oxford, 1994).

- Campbell, Michael J., and John H. Morrison. "Monoclonal antibody to neurofilament protein (SMI-32) labels a subpopulation of pyramidal neurons in the human and monkey neocortex." *Journal of Comparative Neurology* 282.2 (1989): 191-205.
- M. Catani, I. Bodi, F. Dell'Acqua, Comment on "The geometric structure of the brain fiber pathways". *Science* **337**, 1605 (2012).
- Chung, Kwanghun, et al. "Structural and molecular interrogation of intact biological systems." *Nature* 497.7449 (2013): 332-337.
- Comin, César H., et al. "Statistical physics approach to quantifying differences in myelinated nerve fibers." *Scientific Reports* 4 (2014).
- da Fontoura Costa, Luciano, Fernando Rocha, and Silene Maria Araújo de Lima. "Characterizing polygonality in biological structures." *Physical Review E* 73.1 (2006): 011913.
- Daqing, Li, et al. "Dimension of spatially embedded networks." *Nature Physics* 7.6 (2011): 481-484.
- Davis, Marc, and P. J. E. Peebles. "A survey of galaxy redshifts. V-The two-point position and velocity correlations." *The Astrophysical Journal* 267 (1983): 465-482.
- Dronkers, Nina F., et al. "Paul Broca's historic cases: high resolution MR imaging of the brains of Leborgne and Lelong." *Brain* 130.5 (2007): 1432-1441.
- Duyckaerts, C. & Godefroy, G. Voronoi tessellation to study the numerical density and the spatial distribution of neurones. *Journal of Chemical Neuroanatomy* **20**, 83-92 (2000).
- El, K.J. et al. Ccr2 deficiency impairs microglial accumulation and accelerates progression of Alzheimer-like disease. *Nature Medicine* **13**, 432-438 (2007).
- Eng, Lawrence F., Roopa S. Ghimikar, and Yuen L. Lee. "Glial fibrillary acidic protein: GFAP-thirty-one years (1969–2000)." *Neurochemical Research* 25.9-10 (2000): 1439-1451.
- Fawcett, James W., and Richard A. Asher. "The glial scar and central nervous system repair." *Brain Research Bulletin* 49.6 (1999): 377-391.
- Fortune, Steven. "A sweepline algorithm for Voronoi diagrams." *Algorithmica* 2.1-4 (1987): 153-174.
- E. L. Giannaris, D. L. Rosene, A stereological study of the numbers of neurons and glia in the primary visual cortex across the lifespan of male and female rhesus monkeys. *Journal of Comparative Neurology* **520**, 3492–3508 (2012).
- Gibson, Jay R., Michael Beierlein, and Barry W. Connors. "Two networks of electrically coupled inhibitory neurons in neocortex." *Nature* 402.6757 (1999): 75-79.
- Goodenberger, McKinsey L., and Robert B. Jenkins. "Genetics of adult glioma." *Cancer Genetics* 205.12 (2012): 613-621.
- Harvey A. Swadlow and Stephen G. Waxman (2012) Axonal conduction delays. [Scholarpedia](#), 7(6):1451.
- Hippocrates. Translated: Francis Adams. "On the Sacred Disease." 400 BCE
- Hodgkin, Alan L., and Andrew F. Huxley. "A quantitative description of membrane current and its application to conduction and excitation in nerve." *The Journal of Physiology* 117.4 (1952): 500.
- Huber, Andrea B., et al. "Signaling at the growth cone: ligand-receptor complexes and the control of axon growth and guidance." *Annual Review of Neuroscience* 26.1 (2003): 509-563.
- Institute of Laboratory Animal Resources Commission of Life Sciences NRC. *Guide for the care and use of laboratory animals* (National Academy Press, Washington, DC, 1996).

- Kerscher, Martin, István Szapudi, and Alexander S. Szalay. "A comparison of estimators for the two-point correlation function." *The Astrophysical Journal Letters* 535.1 (2000): L13.
- R. Kimmel, N. Kiryati, and A. M. Bruckstein. Distance maps and weighted distance transforms. *Journal of Mathematical Imaging and Vision, Special Issue on Topology and Geometry in Computer Vision*, 6:223-233,1996.
- H. Knutsson, C-F. Westin, M. Andersson, Representing local structure using tensors II. (*SCIA, Berlin-Heidelberg, Springer-Verlag*, 2011).
- Koffie, R.M. *et al.* Oligomeric amyloid beta associates with postsynaptic densities and correlates with excitatory synapse loss near senile plaques. *Proceedings of the National Academy of Sciences* **106**, 4012-4017 (2009).
- Kulijewicz-Nawrot, M., Sykova, E., Chvatal, A., Verkhratsky, A., & Rodriguez, J.J. Astrocytes and glutamate homeostasis in Alzheimer's disease: a decrease in glutamine synthetase, but not in glutamate transporter-1, in the prefrontal cortex. *ASN Neuro*. **5**, 273-282 (2013).
- Lal, Ratnesh, Hai Lin, and Arjan P. Quist. "Amyloid beta ion channel: 3D structure and relevance to amyloid channel paradigm." *Biochimica et Biophysica Acta (BBA)-Biomembranes* 1768.8 (2007): 1966-1975.
- Ledoux, Hugo. "Computing the 3d Voronoi diagram robustly: An easy explanation." *Voronoi Diagrams in Science and Engineering, 2007. ISVD'07. 4th International Symposium on*. IEEE, 2007.
- Lee, Tai Sing. "Image representation using 2D Gabor wavelets." *Pattern Analysis and Machine Intelligence, IEEE Transactions on* 18.10 (1996): 959-971.
- Marquardt, Till, et al. "Coexpressed EphA receptors and ephrin-A ligands mediate opposing actions on growth cone navigation from distinct membrane domains." *Cell* 121.1 (2005): 127-139.
- Mervis, Ronald F. "Neuron Gallery Collection, Neurostructural.org"
- Meyer-Luehmann, M. *et al.* Rapid appearance and local toxicity of amyloid-beta plaques in a mouse model of Alzheimer's disease. *Nature*. **451**, 720-724 (2008).
- Mountcastle, Vernon B. "The columnar organization of the neocortex." *Brain* 120.4 (1997): 701-722.
- Nedergaard, Maiken. "Direct signaling from astrocytes to neurons in cultures of mammalian brain cells." *Science* 263.5154 (1994): 1768-1771.
- Nimmerjahn, Axel, et al. "Sulforhodamine 101 as a specific marker of astroglia in the neocortex in vivo." *Nature Methods* 1.1 (2004): 31-37.
- O'Leary, Dennis DM, and Toshio Terashima. "Cortical axons branch to multiple subcortical targets by interstitial axon budding: implications for target recognition and "waiting periods"." *Neuron* 1.10 (1988): 901-910.
- Pakkenberg, Bente, et al. "Aging and the human neocortex." *Experimental Gerontology* 38.1 (2003): 95-99.
- Panter, S. Scott, et al. "Glial fibrillary acidic protein and Alzheimer's disease." *Neurochemical Research* 10.12 (1985): 1567-1576.
- Paxinos, George, et al. "Bregma, lambda and the interaural midpoint in stereotaxic surgery with rats of different sex, strain and weight." *Journal of Neuroscience Methods* 13.2 (1985): 139-143.
- Perea, Gertrudis, Marta Navarrete, and Alfonso Araque. "Tripartite synapses: astrocytes process and control synaptic information." *Trends in Neurosciences* 32.8 (2009): 421-431.
- Perge, János A., et al. "Why do axons differ in caliber?" *The Journal of Neuroscience* 32.2 (2012): 626-638.
- Peters, Alan, et al. "Neurobiological bases of age-related cognitive decline in the rhesus monkey." *Journal of Neuropathology & Experimental Neurology* 55.8 (1996): 861-873.

Peters, A and Folger-Sethares, C. "The fine structure of the aging brain." Boston University School of Medicine, 72 East Newton Street, Boston, MA 02118. www.bu.edu/agingbrain
Supported by the Institute on Aging of the National Institute of Health, grant number P 01-AG 000001

Pineda, E., Garrido, V., & Crespo, D. Domain-size distribution in a Poisson-Voronoi nucleation and growth transformation. *Physical Review E. Statistical, Nonlinear, and Soft Matter Physics* **75**, 040107 (2007).

Otsu, Nobuyuki. "A threshold selection method from gray-level histograms." *Automatica* 11.285-296 (1975): 23-27.

Perez-Nievas, B.G. *et al.* Dissecting phenotypic traits linked to human resilience to Alzheimer's pathology. *Brain*. **136**, 2510-2526 (2013).

Prewitt, Judith, and Mortimer L. Mendelsohn. "The analysis of cell images*." *Annals of the New York Academy of Sciences* 128.3 (1966): 1035-1053.

Rakic, Pasko. "Specification of cerebral cortical areas." *Science* 241.4862 (1988): 170-176.

Rasband, W.S., ImageJ, U. S. National Institutes of Health, Bethesda, Maryland, USA, <http://imagej.nih.gov/ij/>, 1997-2014

Rockland, Kathleen S., Kadharbatta S. Saleem, and Keiji Tanaka. "Divergent feedback connections from areas V4 and TEO in the macaque." *Visual Neuroscience* 11.03 (1994): 579-600.

Ripley, Brian D. "The second-order analysis of stationary point processes." *Journal of Applied Probability* (1976): 255-266.

Rudolph, Judith, *et al.* "Ephrins guide migrating cortical interneurons in the basal telencephalon." *Cell Adhesion & Migration* 4.3 (2010): 400-408.

Santos A. "[Radial Distribution Function for Hard Spheres](http://demonstrations.wolfram.com/RadialDistributionFunctionForHardSpheres/WolframDemonstrationsProject)"
[http://demonstrations.wolfram.com/RadialDistributionFunctionForHardSpheres/Wolfram Demonstrations Project](http://demonstrations.wolfram.com/RadialDistributionFunctionForHardSpheres/WolframDemonstrationsProject); Published: May 14, 2013

Johannes Schindelin, Ignacio Arganda-Carreras, Erwin Frise, Verena Kaynig, Mark Longair, Tobias Pietzsch, Stephan Preibisch, Curtis Rueden, Stephan Saalfeld, Benjamin Schmid, Jean-Yves Tinevez, Daniel James White, Volker Hartenstein, Kevin Eliceiri, Pavel Tomancak and Albert Cardona (2012) [Fiji: an open-source platform for biological-image analysis](https://doi.org/10.1038/nmeth.1717), *Nature Methods* 9(7): 676-682

Schoenemann, P. Thomas, Michael J. Sheehan, and L. Daniel Glotzer. "Prefrontal white matter volume is disproportionately larger in humans than in other primates." *Nature neuroscience* 8.2 (2005): 242-252.

Serrano-Pozo, A. *et al.* Differential relationships of reactive astrocytes and microglia to fibrillar amyloid deposits in Alzheimer disease. *Journal of Neuropathology & Experimental Neurology* **72**, 462-471

Serrano-Pozo, A., Gomez-Isla, T., Growdon, J.H., Frosch, M.P., & Hyman, B.T. A phenotypic change but not proliferation underlies glial responses in Alzheimer disease. *American Journal of Pathology* **182**, 2332-2344 (2013).

Shaw, G. "Microglia and Neurons." http://commons.wikimedia.org/wiki/File:Microglia_and_neurons.jpg, Wikimedia Commons / [CC-BY-SA-3.0](https://creativecommons.org/licenses/by-sa/3.0/) / [GFDL](https://creativecommons.org/licenses/by-sa/3.0/) (A)

Shaw, G. "Astrocyte 5." <http://en.wikipedia.org/wiki/Astrocyte#mediaviewer/File:Astrocyte5.jpg>, Wikimedia Commons / [CC-BY-SA-3.0](https://creativecommons.org/licenses/by-sa/3.0/) / [GFDL](https://creativecommons.org/licenses/by-sa/3.0/) (B)

Schindelin, Johannes, *et al.* "Fiji: an open-source platform for biological-image analysis." *Nature methods* 9.7 (2012): 676-682.

Shlosman, S. B. "Signs of the Ising model Ursell functions." *Communications in Mathematical Physics* 102.4 (1986): 679-686.

Sternberg, Stanley R. "Biomedical image processing." *Computer* 16.1 (1983): 22-34.

- Szalay, Sándor. *Large Scale Structures of the Universe*. No. 130. Springer, 1988.
- Takano, Takahiro, et al. "Astrocyte-mediated control of cerebral blood flow." *Nature Neuroscience* 9.2 (2005): 260-267.
- Tyler, William A., and Tarik F. Haydar. "Multiplex genetic fate mapping reveals a novel route of neocortical neurogenesis, which is altered in the Ts65Dn mouse model of Down syndrome." *The Journal of Neuroscience* 33.12 (2013): 5106-5119.
- Ulm, K. "Simple method to calculate the confidence interval of a standardized mortality ratio (SMR)." *American Journal of Epidemiology* 131.2 (1990): 373-375.
- Urbanc, B. et al. Neurotoxic effects of thioflavin S-positive amyloid deposits in transgenic mice and Alzheimer's disease. *Proceedings of the National Academy of Sciences* 99, 13990-13995 (2002).
- Verghese, P.B. et al. ApoE influences amyloid-beta (Abeta) clearance despite minimal apoE/Abeta association in physiological conditions. *Proceedings of the National Academy of Sciences* 110, E1807-E1816 (2013).
- Watts, Duncan J., and Steven H. Strogatz. "Collective dynamics of 'small-world' networks." *Nature* 393.6684 (1998): 440-442.
- V. J. Wedeen, P. Hagmann, W. Y. Tseng, T. G. Reese, R. M. Weisskoff, Mapping complex tissue architecture with diffusion spectrum magnetic resonance imaging. *Magnetic Resonance in Medicine* 54, 1377-86 (2005).
- V. J. Wedeen, R. P. Wang, J. D. Schmahmann, T. Benner, W. Y. I. Tseng, G. Dai, D. N. Pandya, P. Hagmann, H. D'Arceuil, A. J. de Crespigny, Diffusion spectrum magnetic resonance imaging (DSI) tractography of crossing fibers. *Neuroimage* 41, 1267-77 (2008).
- Wedeen, Van J., et al. "The geometric structure of the brain fiber pathways." *Science* 335.6076 (2012a): 1628-1634.
- Wedeen, Van J., et al. "Response to Comment on "The Geometric Structure of the Brain Fiber Pathways." *Science* 337.6102 (2012b): 1605-1605.
- De Winter, Fred, Anthony JGD Holtmaat, and Joost Verhaagen. "Neuropilin and class 3 semaphorins in nervous system regeneration." *Neuropilin: From Nervous System to Vascular and Tumor Biology*. Springer US, 2002. 115-139
- Wilhelmsson, U. et al. Redefining the concept of reactive astrocytes as cells that remain within their unique domains upon reaction to injury. *Proceedings of the National Academy of Sciences* 103, 17513-17518 (2006)
- Zhang, Kechen, and Terrence J. Sejnowski. "A universal scaling law between gray matter and white matter of cerebral cortex." *Proceedings of the National Academy of Sciences* 97.10 (2000): 5621-5626.

Curriculum Vitae

Will Morrison

Boston University, Physics Department

Center For Polymer Studies

590 Commonwealth Avenue Boston, Massachusetts 02215 USA

Education

January 2015, Ph.D. Physics, Boston University, Boston, MA Advisor: H. Eugene

Stanley Thesis: UNDERSTANDING THE BRAIN THROUGH ITS SPATIAL STRUCTURE

January 2013: M.A Physics, Boston University, Boston, MA Advisor: H. Eugene Stanley

May 2007: B.S Physics, University of New Hampshire, Durham, NH Advisor: Maurik Holtrop.

Publications

Meni Wanunu, Will Morrison, Yitzhak Rabin, Alexander Y. Grosberg, Amit Meller.

"Electrostatic focusing of unlabelled DNA into nanoscale pores using a salt gradient." *Nature nanotechnology* 5.2 (2009): 160-165.

Alon Singer, Meni Wanunu, Will Morrison, Heiko Kuhn, Maxim Frank-Kamenetskii, Amit Meller. "Nanopore based sequence specific detection of duplex DNA for genomic profiling." *Nano letters* 10.2 (2010): 738-742.

César H. Comin, João R. Santos, Dario Corradini, Will Morrison, Chester Curme, Douglas L. Rosene, Andrea Gabrielli, Luciano da F. Costa & H. Eugene Stanley. "Statistical physics approach to quantifying differences in myelinated nerve fibers." *Scientific reports* 4 (2014).